

# 2D Polarized Materials: Ferromagnetic, Ferrovalley, Ferroelectric Materials, and Related Heterostructures

Junwei Chu, Yang Wang, Xuepeng Wang, Kai Hu, Gaofeng Rao, Chuanhui Gong, Chunchun Wu, Hao Hong, Xianfu Wang,\* Kaihui Liu,\* Chunlei Gao,\* and Jie Xiong\*

The emergence of 2D polarized materials, including ferromagnetic, ferrovalley, and ferroelectric materials, has demonstrated unique quantum behaviors at atomic scales. These polarization behaviors are tightly bonded to the new degrees of freedom (DOFs) for next generation information storage and processing, which have been dramatically developed in the past few years. Here, the basic 2D polarized materials system and related devices' application in spintronics, valleytronics, and electronics are reviewed. Specifically, the underlying physical mechanism accompanied with symmetry broken theory and the modulation process through heterostructure engineering are highlighted. These summarized works focusing on the 2D polarization would continue to enrich the cognition of 2D quantum system and promising practical applications.

These researches have significantly promoted the electronic devices performance and associated manufacturing chains. Recently, benefited from the quantum mechanics, numerous polarization behaviors have been demonstrated in the 2D limit. Focusing on the spontaneous polarization, the magnetism in CrGeTe<sub>3</sub>, the polarized valley splitting in CrI<sub>3</sub>, and the in-plane (IP) ferroelectricity in SnTe have been revealed.<sup>[12–14]</sup> Distinguished from the traditional thin films behavior, in which the polarization is fragile at nanometer scale, the crystal structures preserved in van der Waals (vdW) nanosheets provide a clean environment on studying the physical origin and

## 1. Introduction

Polarization, including electronic polarization, magnetic polarization, and valley polarization, has long been the heart of enormous theoretical calculations, experimental set-ups, and practical devices.<sup>[1–6]</sup> In the past few decades, the detection and manipulation of these polarization behaviors are tightly related to the corresponding degrees of freedom (DOFs).<sup>[7–11]</sup>

response to external fluctuations. These 2D polarized crystals with splendid elements component and crystal structures are also suggesting novel electronic, spintronic, and valleytronic devices.<sup>[15–18]</sup> 2D polarized memory and logic devices have been constructed. For instance, CrI<sub>3</sub> based magnetic tunneling junctions are favored for the layered-dependent magnetism, where a recording high magnetoresistance over 19000% was reported, and 2D ferroelectric field effect transistors fulfilled the combined memory and logic applications.<sup>[19,20]</sup> In the circumstance that Moore's law approaching the physical limits, the developed multifunctional 2D polarization electronics are crucial for low-power dissipation, high-density integrated circuits.

J. Chu, X. Wang, Y. Wang, K. Hu, G. Rao, C. Gong, C. Wu, Prof. X. Wang, Prof. J. Xiong

State Key Laboratory of Electronic Thin Film and Integrated Devices  
University of Electronic Science and Technology of China  
Chengdu 610054, China

E-mail: xfwang87@uestc.edu.cn; jjexiong@uestc.edu.cn

H. Hong, Prof. K. Liu

State Key Laboratory for Mesoscopic Physics  
Collaborative Innovation Center of Quantum Matter  
School of Physics

Peking University  
Beijing 100871, China  
E-mail: khliu@pku.edu.cn

C. Gao

State Key Laboratory of Surface Physics  
Key Laboratory of Micro and Nano Photonic Structures (MOE)  
Department of Physics, and Institute for Nanoelectronic Devices  
and Quantum Computing

Fudan University  
Shanghai 200433, China  
E-mail: clgao@fudan.edu.cn

 The ORCID identification number(s) for the author(s) of this article can be found under <https://doi.org/10.1002/adma.202004469>.

Moreover, 2D polarized materials provide a direct vdW stacking routine on the devices' construction process, which prevents the lattice mismatch in traditional epitaxial heterostructures. Considering the atomically thin nature, the interfaces plays a critical role in the 2D devices, where the proximity effects demonstrate the power on modulating physical behaviors.<sup>[21]</sup> Specifically, the quantum confinement effect and spin-orbital coupling (SOC) dominate the tailoring process. The former confines the carriers effective mass ( $m^*$ ) in nanosheets, while the latter determines the electron-spin interaction at the interface.<sup>[22–25]</sup> And thus the band structure in 2D materials, corresponding to the optical and transfer behavior of DOFs, are modulated.<sup>[26–29]</sup> By constructing polarized heterostructures with ultraclean interfaces, various proximity effects and devices have been demonstrated, where the polarization penetrates into the neighboring non-polarized layer. Usually these heterostructures possess greatly enhanced polarization behavior than pristine materials. Represented by the CrI<sub>3</sub>/WSe<sub>2</sub> heterostructures, researchers have

DOI: 10.1002/adma.202004469

mediated the polarization Zeeman splitting around 5 meV, corresponding to an ultrahigh exchange field over 20 T.<sup>[30]</sup> The amplified polarization at the interface is motivating researchers on revealing the quantum mechanisms lying behind and exploiting their practical applications.

In this review, we focus on the two aspects, from the materials synthesis to the devices construction are introduced in sequence. We first give a fundamental introduction on the polarization physics, followed with the related characterization techniques. Focusing on the polarized electronics, we further discuss the spintronics, valleytronics and ferroelectric electronics. In these sections, an introduction of polarization with inversion asymmetry factors and polarization modulated DOFs is concerned. Finally, we give a brief outlook on the potential materials landscape and novel polarization devices. This review aims to provide researchers with an instruction of physics and materials on the emerging 2D polarized electronics.

## 2. Fundamentals

As shown in **Figure 1**, we focus on the spontaneous polarization on spin, valley, and charge DOFs when we indicate the polarization behavior. Accordingly, there are three kinds of polarization: ferromagnetism (FM), ferrovalley, and ferroelectricity (FE). In this section, the important concept, polarization, is introduced. The origin accordingly to the three characters are discussed.

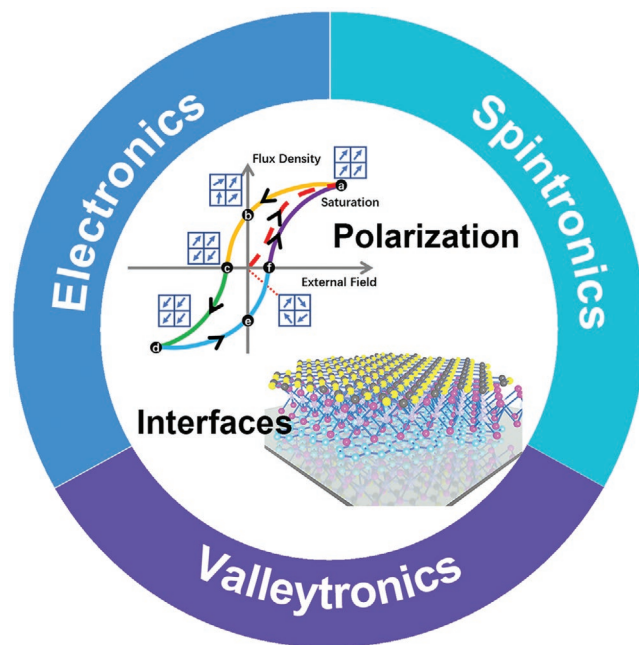


**Figure 1.** Fundamental physical phenomena that should be highlighted for 2D polarized system. In pristine 2D monolayer- or multilayered materials, the spontaneous polarization over external field defines the hysteresis behavior, which determines the basic performance of constructed devices. The three kinds of polarization, ferromagnetism, ferrovalley, and ferroelectricity, corresponds to spin, valley, and charge DOF, respectively. On modulating the DOFs, corresponding devices are constructed, in which the interface determines the modulating process.

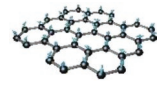
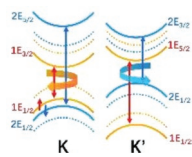
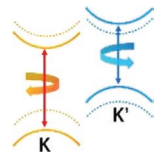
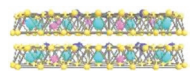
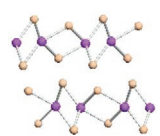
### 2.1. Polarization in 2D Materials

The direct observation over spontaneous polarization is the hysteresis to external field. Considering the polarized materials, such as  $\text{Fe}_3\text{GeTe}_2$ , under an external polarity field, the hysteresis loop occurs below the Néel temperature. As shown in Figure 1, paramagnetic, paraelectric, or paravalley behavior are maintained in the corresponding pristine materials for their disordered dipoles (the original point). Once we introduce an external polarity field, the dipole moments in the materials align to be paralleled with the field direction and the flux density saturates with the increased field ( $P_S$ , a point). When we remove the polarity field, disorders emerge in the system and the flux reduces with the decreased field. However, some remnant polarity ( $P_R$ , b point) still exist due to the spontaneous polarization.  $P_R$  indicates the polarity remained in a polarized material (ferromagnets, ferroelectrics, or ferrovalley) after the external magnetic or electric field is removed. To reduce the flux density to zero, a depolarize field on the reverse direction is necessary and denominated as coercivity ( $-P_C$ , c point).  $P_C$  is the ability of a polarized material against the external depolarized field. The same saturation, retentivity, and coercivity process would be repeated with the reversed external field direction, and the corresponding points at d, e, f are named as  $-P_S$ ,  $-P_R$ , and  $P_C$ , respectively. We should be noticed that the hysteresis loop continues with the sequence of a–f and would not go back to the original point with no flux density at zero external field. A depolarize process, such as increasing the temperature or the pressure, is necessary to disorient the dipoles and terminate the hysteresis behavior. The hysteresis loop is the direct evidence determining the polarity of materials. In fact, the flux density could be any other factors reflecting the polarity, such as the polarization field in the magnetic Kerr effect, the phase angle in the phase diagram of piezoelectric force microscope, and the field dependent resistance, as discussed in Section 3.

For ferromagnetic materials, the magnetism emerges from the spins of charges, specifically, the exchange coupling between the neighboring spins. The spin dimensionality is usually employed to describe the spin orders. As shown in **Table 1**, where three models, Ising model, XY model, and Heisenberg model, are proposed, corresponding to the spin dimensionality of 1, 2, and 3. According to the theory developed by Mermin and Wagner, there would be neither spontaneous ferromagnetic nor antiferromagnetic isotropic crystals at the 2D limit with Heisenberg model. The isotropic crystal nature would introduce gapless spin-wave excitation at any finite temperature and thus destroy the spontaneous or sublattice magnetism. Fighting against the thermal fluctuation, in the recent developed 2D magnets, such as  $\text{CrI}_3$ ,  $\text{CrGeTe}_3$ , and  $\text{Fe}_3\text{GeTe}_2$ , anisotropy plays a critical role.<sup>[31–35]</sup> There are mainly shape anisotropy from the dipole–dipole interaction and magnetocrystalline anisotropy from the spin–orbital interaction. Usually, in the 2D limit, shape anisotropy dominates the magnetic behaviors in thin films and the magnetocrystalline anisotropy is the key factor for magnetic nanocrystals.

Another kind of polarization, ferrovalley, is locked to the spontaneous valley polarization with lifted degeneracy.<sup>[36–41]</sup> The valley polarization could usually be modulated by the external

**Table 1.** Classification on 2D polarization.

Polarization	Classification	Symmetry description	Materials system	Schematic diagram
Ferromagnetism	Ising model	Spin alignment along c direction, spin-up or spin-down with equal energy. Discrete symmetry	CrI <sub>3</sub>	
	XY model	Spin alignment rotate only in xOy plane. Half-continuous symmetry	NiPS <sub>3</sub>	
	Heisenberg model	The energy spins are invariant to rotating every spin in the same way around the unit sphere. Continuous symmetry	Fe <sub>3</sub> GeTe <sub>2</sub> CrCl <sub>3</sub>	
Ferrovalley	Intrinsic materials	SOC lifted valley and spin degeneracy. Time reversal asymmetry	2H-VSe <sub>2</sub>	
	Heterostructures	Valley degeneracy due to the proximity effect. Structure inversion asymmetry	WS <sub>2</sub> /CrI <sub>3</sub> WSe <sub>2</sub> /EuO	
Ferroelectricity	Intralayer interaction	Inversion symmetry breaking from crystal distortion or structure reformation.	SnTe CuInP <sub>2</sub> S <sub>6</sub> $\alpha$ -In <sub>2</sub> Se <sub>3</sub>	
	Interlayer interaction	Inversion symmetry breaking from varying interlayer potential.	WTe <sub>2</sub>	

magnetic or electrostatic field. Predicted with the SOC (with strong coupled spin and valley DOFs) and intrinsic exchange interaction of transition-metal d electrons, VSe<sub>2</sub> in 2H phase is supposed to possess polarized valley behavior.<sup>[42]</sup> However, intrinsic ferrovalley materials are very rare, utilizing the exchange field at the interface, ferrovalley heterostructures have thus been invented. Represented by the WSe<sub>2</sub>/CrI<sub>3</sub> system, the chirality optical bandgap and anomalous valley Hall effects in TMDs have been demonstrated in these heterostructures.<sup>[43]</sup>

Ferroelectricity indicates the spontaneous charge polarization modulated by an external electric field. There are mainly two types of origin for ferroelectricity: structure distortion (ion displacement) and electron correlation. The latter is rather rare, and usually discovered in the multiferroic materials, which possess magnetic and ferroelectric order in simultaneous.<sup>[44–48]</sup> Represented by LuFe<sub>2</sub>O<sub>4</sub> and K<sub>0.6</sub>FeF<sub>3</sub>, the electric dipole depends on electron correlations, rather than the covalency.<sup>[49,50]</sup> For traditional non-layered materials, structure distortion induced ferroelectricity have been demonstrated in BaTiO<sub>3</sub> and BiFeO<sub>3</sub> thin films with several unit cell thickness.<sup>[51,52]</sup> However, selected substrates with lattice matching is necessary for maintaining the structure distortion. For the vdW materials, where lattice mismatches are avoided, interlayer interactions and intralayer bonding play more crucial roles, as represented by WTe<sub>2</sub> and SnTe. In detail, the intralayer ferroelectricity in

SnTe is attributed to the lattice distortion and reconstruction of the Sn–Te covalent bands. Specially, the ferroelectricity is decided by the screening effect of the carriers on the dipole–dipole interaction, and thus a strongly enhanced ferroelectricity with Curie temperature reaches 270 K was observed in monolayer SnTe.<sup>[14,53]</sup> While for WTe<sub>2</sub>, the polarization may involve a relative movement of the electron cloud to the ion core, which indicates ferroelectricity of WTe<sub>2</sub> may origin from electron-hole correlation effects. Based on first-principle calculations, it has been predicted that the in plane slippage could contribute interlayer vertical charge transfer and introduce ferroelectricity.<sup>[54,55]</sup>

The robustness of 2D polarization is rather complicated. Considering the phase transition temperature, the magnetic order is usually compressed, while the ferroelectricity is enhanced at 2D limit. The origin of this behavior is still ambiguous, which need more researches on this topic.

## 2.2. Interface in Heterostructures

The heterostructures interfaces possess great advantages for the synergistic effects of polarized materials and traditional TMDs. There are two types of interfaces during the fabrication and modulation process of 2D polarized devices, the contact interface, and the channel interface. The contact interface

dominates the charge/spin injection process, and the contact engineering focuses on constructing high-quality electrical metal/semiconductor contacts.<sup>[56,57]</sup> The channel interface dominates the polarization process and interconnection of DOFs. Utilizing surface decoration, doping and polarized dielectrics, the doping type and carriers concentration for charge DOF, and the polarity for valley and spin DOFs, could thus be tailored. In this review, we mainly focus on the channel interfaces, and the polarity modulated DOFs. The interactions at the hetero-interfaces would be discussed specifically in the later sections, herein, some concepts are informed for a basic cognition.

The proximity effect was first demonstrated in superconductors, where the adjacent non-superconducting materials were transformed to be superconductors.<sup>[58]</sup> Similarly, for polarized heterostructures, the proximity effects indicate polarization in polarized substrates or functional layers penetrates into non-polarized channel layers. The proximity effects are thus superior on conceiving functional polarized heterostructures. 2D materials are ideal candidates for the proximity effects which are usually confined to the few nanometers at the interface.<sup>[59–63]</sup> We should be especially informed that the proximity effects can also introduce symmetry breaking factors. For instance, for pristine monolayer WSe<sub>2</sub>, in spite of a considerable high SOC and inversion asymmetry induced valley splitting, the valley degeneracy at K and K' valley is still protected by the time reversal symmetry.<sup>[41]</sup> Nevertheless, by introducing the interface exchange field in WSe<sub>2</sub>/EuS heterostructures, the time reversal symmetry is broken and an ultrahigh valley splitting is observed.<sup>[64]</sup> Similar results, such as the opening of energy gap, and the spin polarization, have also been demonstrated with reduced symmetry order parameters.<sup>[65]</sup> Thus, these factors have provided great possibilities on manipulating the DOFs.

Considering the spin and valley DOFs, the asymmetry factors and SOC are always coupled, Bychrov-Rashba SOC should be especially concerned in structural inversion asymmetric systems.<sup>[66]</sup> The Bychrov-Rashba SOC determines the in-plane spin alignment in heterostructures, as depicted by

$$H_{BR} = \alpha_{BR} (\mathbf{k}_x \sigma_y - \mathbf{k}_y \sigma_x) \quad (1)$$

herein,  $\alpha_{BR}$  denotes the Bychkov-Rashba parameter, as determined by the position dependent band-edge profiles in the momentum space.  $\mathbf{k}_x$  and  $\mathbf{k}_y$  denote the wave vectors,  $\sigma_x$  and  $\sigma_y$  denote the Pauli matrix. The Bychkov-Rashba SOC could be interpreted as an equivalent magnetic field coupled spin DOF with Zeeman-like interaction, as

$$H_{BR} = \mu_B \sigma B_{eff}(\mathbf{k}) \quad (2)$$

$$B_{eff}(\mathbf{k}) = \frac{1}{\mu_B} \alpha_{BR} (-\mathbf{k}_x, \mathbf{k}_y, 0) \quad (3)$$

where the  $k$  dependent magnetic field  $B_{eff}(k)$  determines the spin orientation ( $\sigma = 1$  or  $\sigma = -1$ ) of a certain eigenstate. The Rashba SOC splits the degenerated energy band into two subbands with an energy splitting of  $\Delta \varepsilon_0 = 2\mu_B |B_{eff}| = 2\alpha_{BR}|k|$ . The Bychkov-Rashba parameter  $\alpha_{BR}$  originates from the interface boundary conditions, that is, band-edge profiles. Thus,  $\alpha_{BR}$  is

sensitive to the external fields and interface characters, which is crucial for modulating the DOFs. For instance, the room temperature gate-controlled charge-to-spin conversion have been demonstrated in WS<sub>2</sub>/graphene heterostructures.<sup>[24,67]</sup>

The mechanism of ferroelectric interfaces is settled by the dipole coupled DOFs. For ferroelectricity modulated charge DOF, the ferroelectric/semiconductor interface will generate positive/negative surface bounded charges with ferroelectric film  $\uparrow/\downarrow$  polarized. Considering the intrinsic semiconductor layer on the ferroelectric substrate. Electrons accumulates at the  $\uparrow$  polarized surface and hole accumulates at the  $\downarrow$  polarized surface. The carriers density and Fermi surface have thus been modulated for obtaining n-type or p-type semiconductors. Due to the hysteresis nature, these ferroelectric/semiconductor heterostructures have been applied for next generation compute-in-memory neutral network devices. For modulating the spin and valley DOFs, ferroelectricity counts greatly on introducing the broken inversion symmetry except for the polarization electrical field. As a result, Dresselhaus SOC should be considered in ferroelectric heterostructures. With a similar effect on in-plane spin degeneracy, the Dresselhaus SOC could be expressed as

$$H_D = (k_x \sigma_x - k_y \sigma_y) \frac{d}{dz} \left( \gamma_z \frac{d}{dz} \right) = \gamma_D (k_x \sigma_x - k_y \sigma_y) \quad (4)$$

where the Dresselhaus parameter  $\gamma_D$  is determined by the bulk inversion factors in noncentrosymmetric crystals. In traditional nonlayered systems, the energy bandgap  $E_0$  and effective mass  $m^*$  have been demonstrated tightly correlated with the Rashba and Dresselhaus SOC. The Dresselhaus-type band splitting have also been theoretically predicted in WO<sub>2</sub>Cl<sub>2</sub> crystals.<sup>[68]</sup>

The polarized heterostructures are now providing researchers with fancy platforms on the modulation of DOFs. Although we have given a basic view on the symmetry and interface factors, the practical situation is much more complicated. In the following sections, ferromagnetism, ferrovalley, and ferroelectricity are reviewed separately, with more detailed materials landscape and devices perspective.

## 3. Preparation and Characterization Technologies of 2D Polarization

### 3.1. Preparation of Polarized 2D Materials and Heterostructures

2D layered materials could be exfoliated smoothly into monolayer or few layers with a Scotch tape method, owing to their interlayer vdW force bonded nature. Currently, most 2D polarized materials are prepared through the mechanical exfoliation method.

Exfoliating from the bulk single crystals guarantees the high quality of few-layered materials for physical studies and device performance. Especially for these environmentally sensitive polarized materials such as CrI<sub>3</sub> and Cr<sub>2</sub>Ge<sub>2</sub>Te<sub>6</sub>, being exfoliated in the inert gas atmospheres and encapsulated by hBN could avoid the expose to oxygen and water in atmosphere, which are effective approaches maintaining their pristine properties. For instance, 2D CrI<sub>3</sub> first reported with layer-dependent

ferromagnetism was obtained by mechanically exfoliating the bulk crystals into mono-, bi-, and trilayer nanoflakes.<sup>[13]</sup> Then the heterostructures stacked with graphene and hBN in sequence were fabricated to control its magnetism electrically.<sup>[32,69,70]</sup> In similar, many other polarized vdW crystals have also been exfoliated with preserved polarity at the 2D limit. For instance, the ferromagnetism in Cr<sub>2</sub>Ge<sub>2</sub>Te<sub>6</sub>, Fe<sub>3</sub>GeTe<sub>2</sub>, and the ferroelectricity in CuInP<sub>2</sub>S<sub>6</sub> (CIPS) were confirmed in the exfoliated nanoflakes.<sup>[12,71–75]</sup> Mechanical exfoliation from the bulk is a smart choice for studying intrinsic properties and demonstrating fundamental devices, but the limitations in material scale and array integration restrict the long-term development of 2D polarization electronics.

To further explore the potential properties and modulating of the 2D polarization, it is necessary to synthesize large-scale 2D materials and even manipulate their components. Vapor deposition is showing unparalleled advantage in producing large-scale, high-quality single crystal nanoflakes with controllable thickness. Molecular beam epitaxy (MBE) and chemical vapor deposition (CVD) are the two most common vapor approaches due to their potential for precisely controlling chemical compositions and relatively low cost. For examples, by using MBE, CrBr<sub>3</sub> films have been obtained, which demonstrate stacking dependent interlayer magnetism. Diverse stacking orders of the second layer CrBr<sub>3</sub> leads to different interlayer coupling and determined the ferromagnetism or antiferromagnetism in bilayer CrBr<sub>3</sub>.<sup>[76]</sup> Bonilla et al. obtained VSe<sub>2</sub> film by MBE method, the transformation from paramagnetic to ferromagnetic when the thickness reduced to monolayer was observed. The as-grown VSe<sub>2</sub> possesses large magnetic moment above room temperature, indicating MBE a promising method to manufacture monolayer polarized vdW materials.<sup>[77]</sup> The demonstration of ferroelectric 2D materials was also supported by MBE. 1- to 4-unit cell (UC) specimens of SnTe were synthesized by Chang et al., followed by in-plane ferroelectricity demonstration.<sup>[14]</sup> Similarly, film with one to seven layers of another chalcogenide of Sn, SnS, was also prepared by MBE.<sup>[78]</sup> Although with the disadvantages of low growth rate and vital high vacuum, MBE method is of great concern in the synthesizing process of 2D polarization with single-crystalline nature.

Apart from the MBE approach mentioned above, CVD method has also been adopted to prepare polarized materials, such as ferrovalley VSe<sub>2</sub>.<sup>[79]</sup> Mica substrate along with most shared precursors metal chloride and selenide powders were utilized in the growth procedure. The scale of nanoflakes is about 5–20 μm, with controllable thickness of 4.9–90 nm.<sup>[80]</sup> The vertical heterostructures with other MX<sub>2</sub> (M: Mo, W; X: S, Se) TMDs were ulteriorly synthesized via a two-step CVD. In the second growth process, VSe<sub>2</sub> displayed a novel growth behavior. VSe<sub>2</sub> prefers to nucleate at the edge of MX<sub>2</sub> first, then grow from edge to the center till covered the whole MX<sub>2</sub> and form sharp interfaces.<sup>[81]</sup> These researches open doors to the better understanding and further study on ferrovalley materials. α-In<sub>2</sub>Se<sub>3</sub> is another binary 2D layered ferroelectric material except for quaternary CIPS, which has been obtained by vapor deposition method. Peng and co-workers first observed the room temperature out-of-plane ferroelectricity in both vapor deposited and mechanically exfoliated α-In<sub>2</sub>Se<sub>3</sub>. During their synthesis process, In<sub>2</sub>Se<sub>3</sub> powder serves as growth source,

and the thickness of as-grown nanoflakes down to single layer has been obtained.<sup>[82]</sup> Furthermore, using the mixed source of In<sub>2</sub>O<sub>3</sub> and Se powders, both α- and β-In<sub>2</sub>Se<sub>3</sub> were synthesized, the existence of in-plane and out-of-plane polarization in α-In<sub>2</sub>Se<sub>3</sub>, while no evidence of polarization in β-In<sub>2</sub>Se<sub>3</sub> were demonstrated.<sup>[83]</sup> Vapor deposition method gives the chance to produce large quantity, scalable and integratable 2D polarized materials. Further, these techniques provide tremendous convenience for in site or postgrowth of 2D polarization engineering, through which artificially designed polarization systems could be fulfilled.

### 3.2. Polarization Engineering of Traditional 2D Materials

Most 2D materials, such as graphene, hBN, MoS<sub>2</sub>, and WSe<sub>2</sub>, are usually pristine unpolarized. Based on these unpolarized 2D materials, extrinsic polarization could be introduced by doping and defects engineering and their applications expanded in consequence. Sorted by the site of the dopants located, surface adsorption, lattice dopants and alloys are the three main types. Surface adsorption of specific molecular could result in structural distortion of 2D materials thus induce polarization. For instance, the covalent bond in 2D superconducting NbSe<sub>2</sub> can be elongated by adsorbing hydrazine molecules on the surface. This tiny elongation could reduce the covalent interaction between Nb and Se then enhance the ionicity of the Nb, which produces ferromagnet order (Figure 2a).<sup>[84]</sup>

Lattice doping and alloying of TMDs are capable to manipulate the band structures and phase structures. With reduced time and space reversal symmetry, polarization is introduced into unpolarized 2D crystals. Specifically, the two techniques of substitutional doping and alloying, corresponds to the band and phase modulation process, respectively. Monolayer MoS<sub>2</sub> doped with Mn atoms was prepared via vapor reaction of S, MoO<sub>3</sub>, and Mn<sub>2</sub>(CO)<sub>10</sub> powders. The substrate dependent epitaxy process has been revealed during the synthesis process, where the MoS<sub>2</sub> with a 2% doping of Mn was only obtained on graphene substrate rather than SiO<sub>2</sub> and sapphire substrates. The MoS<sub>2</sub> nanoflakes obtained on SiO<sub>2</sub> and sapphire show many Mn-caused defects rather than doped Mn into the lattice due to the reactive surface terminations. A red shift and large intensity quenching of photoluminescence (PL) of MoS<sub>2</sub> on SiO<sub>2</sub> and sapphire were observed compared with pristine MoS<sub>2</sub> (Figure 2b). The shift and quenching of PL may be caused by the bound excitons generated by defects.<sup>[85]</sup> Thus, there are also negative side effects when introducing magnetism into TMDs by defects or doping magnetic atoms. Further, Wei and co-workers found that electronic interactions between substitutional Co atoms and Cr adatoms could largely enhance the ferromagnetism of monolayer MoS<sub>2</sub>, and the STEM image is showed in Figure 2d. A T<sub>C</sub> above room temperature with increased PL intensity has been achieved. X-ray absorption fine structure showed two coordination peaks of Co–S and Co–Mo at the Co K-edge, yet only one peak of Cr–S at Cr K-edge. The results suggest Cr atoms occupy the top site of monolayer MoS<sub>2</sub> and Co atoms serve as substitutional atoms. Magnetic measurements exhibited that the room-temperature saturation magnetization of Co–MoS<sub>2</sub> was 90 times higher than that

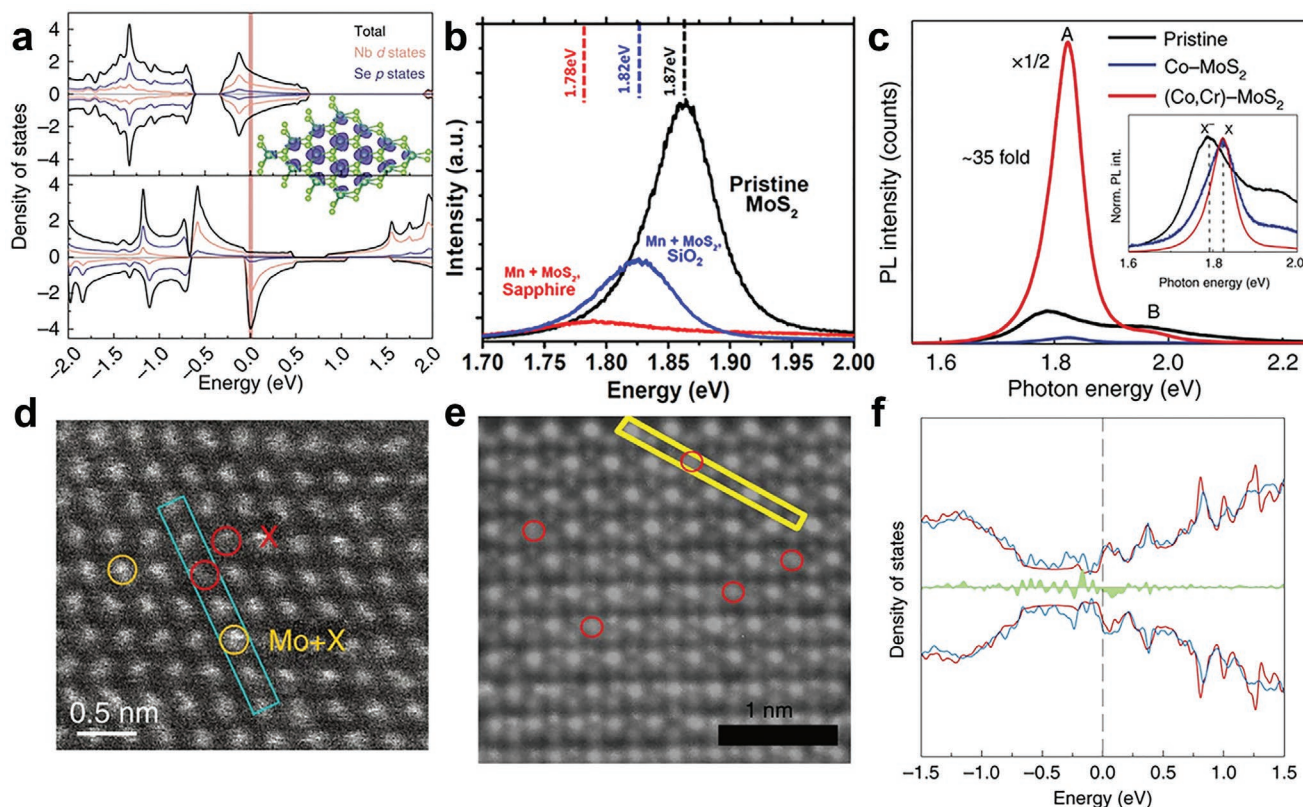


**Figure 2.** a) The DOS of the pure (up) and surface-absorbed (down) NbSe<sub>2</sub> nanosheets. Reproduced under the terms of the CC-BY 4.0 License.<sup>[84]</sup> Copyright 2016, The Authors, published by Springer Nature. b) The PL spectra of pristine MoS<sub>2</sub>, Mn-doped MoS<sub>2</sub> on sapphire and SiO<sub>2</sub>. Reproduced with permission.<sup>[85]</sup> Copyright 2015, American Chemical Society. c) Unnormalized and normalized (inset) PL spectra of pristine, Co-MoS<sub>2</sub>, and (Co, Cr)-MoS<sub>2</sub>. d) STEM image of the (Co, Cr)-MoS<sub>2</sub> monolayer. c,d) Reproduced under the terms of the CC-BY 4.0 License.<sup>[86]</sup> Copyright 2019, The Authors, published by Springer Nature. e) STEM image of the Fe-SnS<sub>2</sub> monolayer. Reproduced under the terms of the CC-BY 4.0 License.<sup>[88]</sup> Copyright 2017, The Authors, published by Springer Nature. f) DOS of PtSe<sub>2</sub> with (blue) and without (red) a V<sub>Pt</sub> defect. Reproduced with permission.<sup>[91]</sup> Copyright 2019, Springer Nature.

of pristine MoS<sub>2</sub>, and the Cr atoms did not contribute much to the improvement of magnetism. The origin of ferromagnetism in doped MoS<sub>2</sub> could be explained by bound magnetic polaron mechanism. In monolayer MoS<sub>2</sub>, there are ferromagnetic interactions between Co ions and an effective magnetic field owing to the spin alignment of defects and neighboring Co ions. Compared with the PL intensity of pristine MoS<sub>2</sub>, a 35-fold improvement in (Co, Cr)-MoS<sub>2</sub>, while greatly restrained in Co-MoS<sub>2</sub> was observed (Figure 2c). The enhancement of PL results from the electronic interactions between the Cr and Co atoms, which inhibits the nonradiative recombination caused by Co-doping.<sup>[86]</sup> Researches mentioned above highly indicate that doping of 2D materials has great potential in future magnetic, electronic, and optoelectronic applications. The pursuit of a relatively easy way to get scalable ferromagnetic TMD monolayers with  $T_C$  above room temperature is rising in these years. Monolayer MoS<sub>2</sub> with in situ substitutional doping of Fe atoms was implemented via low-pressure CVD method. PL spectroscopy showed the emission of Fe is around 2.28 eV, and the presence of Fe atom was also proved by STEM and Raman spectroscopy. With the measurement of nitrogen-vacancy center magnetometry, a large local field of  $0.5 \pm 0.1$  mT was observed, and

hysteresis loop measured by superconducting quantum interference devices revealed  $T_C$  has not been reached at 300 K.<sup>[87]</sup>

Alloying method introduces novel phases into the 2D system. For instance, Fe-doped SnS<sub>2</sub> alloy (Figure 2e), Fe<sub>0.021</sub>Sn<sub>0.979</sub>S<sub>2</sub> has shown ferromagnetic property with Curie temperature of  $\approx 31$  K and considerable optoelectronic performance.<sup>[88]</sup> The alloying bulk crystals were synthesized by vapor transport method, whereafter exfoliated into monolayer flakes. For the investigation of magnetism, a physical properties measurement system shows a notable anisotropy at 2 K. The coercivity and remnant magnetization are three and five times of that in paralleled direction, respectively. The easy axis lying in c direction indicates the 2D magnetism from anisotropy. The calculation of total density of states (DOS) shows the impurity levels of Fe-SnS<sub>2</sub> monolayer at the Fermi level come from the Fe atoms. Phase transition of MoSe<sub>2</sub> could be realized by alloying with Re atoms during the CVD process. A distinct transition from 2H to 1T' was observed with a middle phase between them. The concentration of Re atoms mainly affected the crystal structures, where it came out to be 2H phase below 40% doping, otherwise 1T' phase.<sup>[89]</sup> Furthermore, magnetic properties were investigated in Mo<sub>1-x</sub>Re<sub>x</sub>Se<sub>2</sub> alloy. The zero-field cooled (ZFC)

and field cooled (FC) measurements indicated that both 2H and 1T' alloys could hold the ferromagnetic behavior at 300 K and existed a competition between antiferromagnetic and ferromagnetic order. When cooling temperature down to 20 K, FC-ZFC showed a superimposed paramagnetic behavior caused by uncorrelated spins. In sum, there is a competition of magnetic correlations in the alloys, and Re atom can tune the phase of TMDs by electron donation, which is of much value in spintronics.

As mentioned above, defects in 2D materials can affect spin states and then induce magnetism into the specimens. Efforts have been done on magnetism in molybdenum dichalcogenides. When incorporating 1T-MoS<sub>2</sub> with 2H-MoS<sub>2</sub>, robust room temperature ferromagnetism is discovered. The unpaired electrons of Mo 4d in 1T-MoS<sub>2</sub> serve as new paramagnetic center and give chance to the enhancement of interactions between sulfur vacancies and Mo<sup>4+</sup> ions, which triggers ferromagnetism. For 2H-MoSe<sub>2</sub> and 2H-MoTe<sub>2</sub>, long-range magnetic order was observed in bulk crystals under 100 and 40 K, respectively. Mo vacancy and substitutional Mo atoms at chalcogen sites are the two major defects, where the magnetic moment of per Mo antisite comes within 0.9 to 2.8 μB, as revealed by DFT calculation.<sup>[90]</sup> As another sample, Pt vacancies in PtSe<sub>2</sub> thin layer would impact the electronic properties and further induce magnetism. Based on Ruderman-Kittel-Kasuya-Yosida (RKKY) model, layer dependent ferro- or antiferromagnetism were obtained. This behavior was also confirmed experimentally when investigating the magneto-transport responses of devices with one layer different. The device fabricated by 6.45 nm PtSe<sub>2</sub> exhibits antiferromagnetic response, while the one with 7.05 nm shows ferromagnetic behavior. More surprisingly, when they fabricated a device using flakes with one additional layer fragments, the response shows the coexistence of ferromagnetic and antiferromagnetic order. First-principles calculations verified the defect-induced spin-split states could cause magnetic moments around the Fermi level (Figure 2f). The research points out the great potential on modulating the magnetism of 2D PtSe<sub>2</sub>, such as increasing the defect concentration, manipulating the crystal thickness and the Fermi level.<sup>[91]</sup>

### 3.3. Characterization of 2D Polarization

Due to the microscopic nature, most macroscopic techniques are limited on characterizing the polarize behavior of 2D nano-flakes. Based on the light-matter interaction, the polarity of photons is sensitive to the time and spatial symmetry. In this section, recent developed technologies are summarized for a better understanding about the magnetism and ferroelectricity in the 2D limit. We mainly focus on the nonlinear optical methods, including magnetic-optical Kerr effect (MOKE) and second harmonic generation (SHG), and piezoresponse force microscope (PFM) technology.

The linearly polarized light consists of left-circularly polarized (LCP) and right-circularly polarized (RCP) light. After incidenting the linearly polarized light into the magnetic materials, the reflection light becomes elliptically polarized due to the disparate propagation velocities of LCP and RCP light in

the specimen. This phenomenon is called MOKE and the angle between the long axis of elliptically polarized light and the incident polarized light is the Kerr rotation angle  $\theta_K$ .<sup>[92]</sup> Here the macroscopic description of MOKE developed by Zak et al. is given.<sup>[93,94]</sup> By defining a situation of film with *N* layers and thickness of *d*, and the light incidenting through the medium *i*, a reflected light will back scatter into medium *i* and a transmitted light will illuminate into medium *f* (Figure 3a). The refractive index and the incident angle of corresponding media are defined as *n* and  $\theta$ . Direction of  $\gamma$  is related to the intersection of incident plane and film plane, and *z* is the surface normal direction. In the case mentioned above, the electric fields in two mediums are<sup>[95]</sup>

$$P_i = \begin{pmatrix} E_s^i \\ E_p^i \\ E_s^r \\ E_p^r \end{pmatrix}_i = \begin{pmatrix} E_s^i \\ E_p^i \\ r_{ss}E_s^i + r_{sp}E_p^i \\ r_{ps}E_s^i + r_{pp}E_p^i \end{pmatrix} \quad (5)$$

and

$$P_f = \begin{pmatrix} E_s^i \\ E_p^i \\ 0 \\ 0 \end{pmatrix}_f = \begin{pmatrix} t_{ss}E_s^i + t_{sp}E_p^i \\ t_{ps}E_s^i + t_{pp}E_p^i \\ 0 \\ 0 \end{pmatrix} \quad (6)$$

in which *r* is the reflection coefficient and *t* is the transmission coefficient. Now two matrices *i* and *f* are defined, which connect with the electrical fields at boundary between the film and the medium. The *s*- and *p*-components of the electric field are parallel and perpendicular to the incident plane, respectively. If introducing matrix *M* for the expression of  $P_i = MP_f$  and according to the the last two terms of the equation above, *M* can be defined as

$$M = \begin{pmatrix} G & H \\ I & J \end{pmatrix} \quad (7)$$

*G* and *I* are 2 × 2 matrices with *t* and *r*, where

$$G^{-1} = \begin{pmatrix} t_{ss} & t_{sp} \\ t_{ps} & t_{pp} \end{pmatrix} \quad (8)$$

and

$$I G^{-1} = \begin{pmatrix} r_{ss} & r_{sp} \\ r_{ps} & r_{pp} \end{pmatrix} \quad (9)$$

For *p*- and *s*-polarized light, the directly measured magnitude of the magneto-optic signal  $\phi$  can be expressed as a function of Kerr rotation angle  $\theta_K$  and ellipticity  $\epsilon_K$

$$\phi_s = \theta_{Ks} + i\epsilon_{Ks} = \frac{r_{ps}}{r_{ss}} \quad (10)$$

and

$$\phi_p = \theta_{Kp} + i\epsilon_{Kp} = \frac{r_{sp}}{r_{pp}} \quad (11)$$

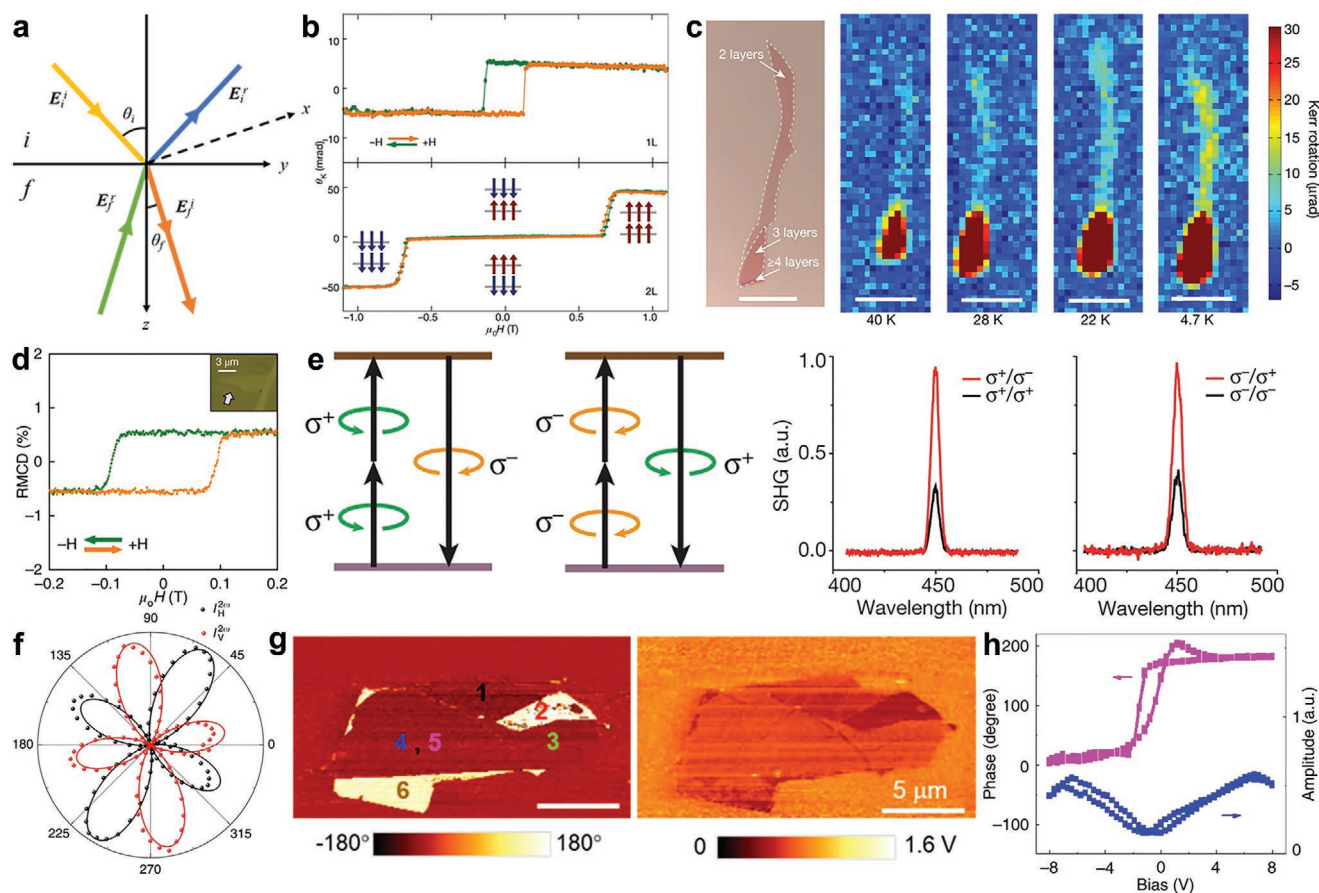


**Figure 3.** a) The schematic diagram of MOKE. b) MOKE signal on a monolayer and bilayer CrI<sub>3</sub> flakes. Reproduced with permission.<sup>[13]</sup> Copyright 2017, Springer Nature. c) Optical image of exfoliated Cr<sub>2</sub>Ge<sub>2</sub>Te<sub>6</sub> monolayer. MOKE signal as the temperature decreases from 40 to 4.7 K. Reproduced with permission.<sup>[12]</sup> Copyright 2017, Springer Nature. d) Polar RMCD signal for a monolayer Fe<sub>3</sub>GeTe<sub>2</sub> at 78 K. Reproduced with permission.<sup>[73]</sup> Copyright 2018, Springer Nature. e) Optical selection rules of circularly polarized SHG. Polarization resolved SHG signal of bilayer CrI<sub>3</sub>. Reproduced with permission.<sup>[97]</sup> Copyright 2019, Springer Nature. f) SHG intensity for a 100 nm CIPS flake. Reproduced under the terms of the CC-BY 4.0 License.<sup>[74]</sup> Copyright 2016, The Authors, published by Springer Nature. g) PFM phase and amplitude images of  $\alpha$ -In<sub>2</sub>Se<sub>3</sub> flake. Reproduced with permission.<sup>[82]</sup> Copyright 2017, American Chemical Society. h) PFM phase hysteresis and butterfly loop of monolayer 1T-MoTe<sub>2</sub>. Reproduced under the terms of the CC-BY 4.0 License.<sup>[100]</sup> Copyright 2019, The Authors, published by Springer Nature.

The expression for ultrathin films such as 2D flakes is simpler because of film thickness is much smaller than light wavelength,  $\sum_i n_i d_i \ll \lambda$ . This description of MOKE is universal for the situation where the optical thickness (product of the geometric thickness and the refractive index of the specimen) of sample is much smaller than the wavelength of the incident light. For 2D ferromagnetic materials, by sampling the rotation angle while sweeping the magnetic field ( $\theta_K$  vs  $H$ ), a hysteresis loop can be obtained. Similar to the magnetic hysteresis, the curve obtains magnetization direction and coercive field (intersection with abscissa) of the specimen.

Magneto-circular dichroism (MCD) microscopy is also called Faraday ellipticity effect, when linearly polarized light incidents a magnetic material, the transmitted light will become elliptically polarized due to the absorptivity difference between LCP and RCP light. The studies on MOKE and MCD indicate the inherent optical-materials interaction, and thus manifesting great potential on the manipulation and application

of polarization in 2D materials and heterostructures. The intrinsic ferromagnetism of monolayer CrI<sub>3</sub> and Cr<sub>2</sub>Ge<sub>2</sub>Te<sub>6</sub> (Figure 3b,c) characterized by MOKE were first reported in 2017.<sup>[12,13]</sup> Further efforts have been done to control their magnetism electrically.<sup>[32,71]</sup> Both RMCD and MOKE were employed for the examination of ferromagnetism in monolayer Fe<sub>3</sub>GeTe<sub>2</sub> (Figure 3d).<sup>[73]</sup> And strong room-temperature ferromagnetic order was observed in monolayer VSe<sub>2</sub> by MOKE, which may draw a lot of attention for spintronics applications.<sup>[77]</sup>

SHG is a nonlinear optical technique utilizing the second harmonic signals generation process to determine the reversal asymmetry. The second harmonic will be generated when the inversion symmetry of specimen is broken. The symmetry of 2D polarized materials varies when they are polarized, so the study of SHG will help understand the changes in space inversion and time-reversal symmetry. The nonlinear polarization of materials can be generally expressed as<sup>[96]</sup>

$$P = \chi^{(1)} E^1 + \chi^{(2)} E^2 + \chi^{(3)} E^3 + \dots \quad (12)$$

where  $P$  is the polarization,  $\chi^{(n)}$  is the  $n$ -th order nonlinear susceptibility and  $E$  is the electric field. In the equation above, the first term is the expression of normal absorption and reflection of incident light. The second term is SHG referring to the sum frequency generation of two incident light with the same frequency. And the frequency of output wave is twice of the frequency of incident light, in which the incident light wave is called fundamental wave and the output wave is called second harmonic. The third one corresponds to the third harmonic generation, light scattering, stimulated Raman process, and two- and three-photon absorption process. During the SHG process, two photons with the same frequency convert into one photon with the fundamental frequency doubled. Consider the incident light field  $E = E_0 \cos(\omega t + \phi)$ , and according to Equation (12), the second-order nonlinear polarization  $P_2$  can be expressed as

$$P_2 = \frac{1}{2} \chi^{(2)} E_0^2 + \frac{1}{2} \chi^{(2)} E_0^2 \cos[2(\omega t + \phi)] \quad (13)$$

The equation indicates that under an incident light with frequency  $\omega$ , the radiation light not only has linear frequency of  $\omega$ , but also nonlinear components of 0 and  $2\omega$  within the electric dipole approximation. The generation of second harmonic signals needs to meet two requirements, the specimen must be noncentrosymmetric and phase matching. The first one is easy to understand with Equation (13), where the SHG wave is a vector quantity. The second-order electric polarizability tensor of centrosymmetric specimen is zero, so second harmonic cannot be generated. The phase matching requirement is related to the energy transfer process. The second-order polarization wave can be coupled with light wave at  $2\omega$  frequency, and the transfer energy depends on the phase mismatch  $\Delta k$ , which influences the SHG efficiency  $\eta$ ,

$$\eta = \frac{P^{2\omega}}{P^\omega} \propto \frac{\sin^2(L\Delta k/2)}{(L\Delta k/2)^2} dL^2 E_0^2 \quad (14)$$

where  $L$  is optical thickness. To maximize SHG efficiency,  $L\Delta k/2 \rightarrow 0$  should be satisfied, that is, best condition of SHG is when the phase mismatch  $\Delta k$  is zero. For 2D materials, SHG has been employed to detect the asymmetry determined polarization. Although two requirements mentioned above are needed for SHG, but in some cases, SHG is also allowed without lattice inversion symmetry, such as antiferromagnetic  $\text{Cr}_2\text{O}_3$ , where an underlayer magnetic structure breaks the time-reversal symmetries. The SHG of bilayer antiferromagnetic  $\text{CrI}_3$  was first reported by Sun et al. (Figure 3e). As lattice structure of bilayer  $\text{CrI}_3$  is centrosymmetric, the SHG was confirmed to resulted only from the antiferromagnetic order, which broke both the spatial-inversion symmetry and the time reversal symmetry.<sup>[97]</sup> Bulk  $\text{MnPS}_3$  was reported to be an antiferromagnet with linear magnetoelectric effect. Whereas due to the absence of net magnetization, MOKE is feeble to verify the magnetic properties down to few-layered limit. In contrast, SHG is alert to antiferromagnetic order, where the signals revealed the magnetoelectric and antiferromagnetic properties of  $\text{MnPS}_3$  still existed in thin layers.<sup>[98]</sup> SHG was also applied in ferroelectric 2D materials such as CIPS (Figure 3f)<sup>[74]</sup> and

$\text{In}_2\text{Se}_3$ <sup>[82]</sup> for the study of relation between broken inversion symmetry and ferroelectricity.

Based on the piezoelectric effect, PFM, a technology to explore the ferroelectricity of materials has been widely applied. Under the excitation of an external electric field, electro-diode formation happens in the ferroelectric specimens. The conductive probe of atomic force microscopy is sensitive this tiny deformation and maps the domain structure, domain inversion, hysteresis loop, and slow relaxation process. Nowadays, PFM has been the main force and common approach to 2D ferroelectricity. The discovery of ferroelectric CIPS,<sup>[74,99]</sup>  $\text{In}_2\text{Se}_3$  (Figure 3g),<sup>[82,83]</sup>  $\text{SnS}$ ,<sup>[78]</sup> and  $\text{MoTe}_2$  (Figure 3h)<sup>[100]</sup> are all profited from PFM detection. The deep study and understanding of 2D ferroelectricity will promote the development of next generation non-volatile memory, and field effect transistors (FETs) based on vdW heterostructures.

Beyond the approaches mentioned above, there are other series of characterizations developed for 2D polarization as well. A single-spin magnetometer based on single nitrogen-vacancy in diamond is capable to image and control the ferromagnets in nanoscale, especially sensitive to antiferromagnetic order. Combined with photoluminescence to measure Zeeman shift, scanning tunneling microscope (STM) or other techniques, the mapping of magnetic order can be achieved. For example, the magnetization of  $\text{CrI}_3$  monolayers is measured to be  $\approx 16 \mu\text{B nm}^{-2}$ .<sup>[101]</sup> For ferroelectricity measurement, the ferroelectricity of  $\text{SnTe}$  is observed via STM<sup>[14]</sup> and that of  $\text{WTe}_2$  is monitored via electrical measurement.<sup>[54]</sup> These techniques mentioned here have demonstrated with great efficiency on determining the 2D polarization.

## 4. Ferromagnetic 2D Materials and FM-Gated Heterostructures

### 4.1. Spintronics in Traditional Layered Materials: Spin Injection, Transport, and Detection

2D materials are favored in spintronic devices due to the reduced in-plane spin scattering and tremendous SOC behaviors. In this section, we will introduce some recent advances in spintronics based on 2D nonmagnetic materials.

Graphene has been widely explored in the spintronics and proved to be an ideal spin channel for its low spin-orbit coupling and negligible hyperfine interactions.<sup>[102–104]</sup> The negligible SOC in graphene is almost perfectly suppressed due to the weak atomic spin-orbital splitting in carbon.<sup>[105]</sup> The hyperfine interaction refers the interaction of nuclear magnetic dipole moment and electron spin and contributes to spin dephasing. Nikolaos et al. first applied graphene channel to build a four-terminal nonlocal device, a spin relaxation length ranges from 1.5 to 2  $\mu\text{m}$  at room temperature was determined.<sup>[106]</sup> This structure of device is also recognized as a lateral spin valve, which exhibited different non-local resistance depending on the magnetization status of the four magnetic electrodes as shown in Figure 4a,b. Based on the nonlocal spin valve device, many efforts were done to improve the performance. On enhancing the spin injection efficiency from the ferromagnetic metal to semiconductor channels, many works focus on minimizing

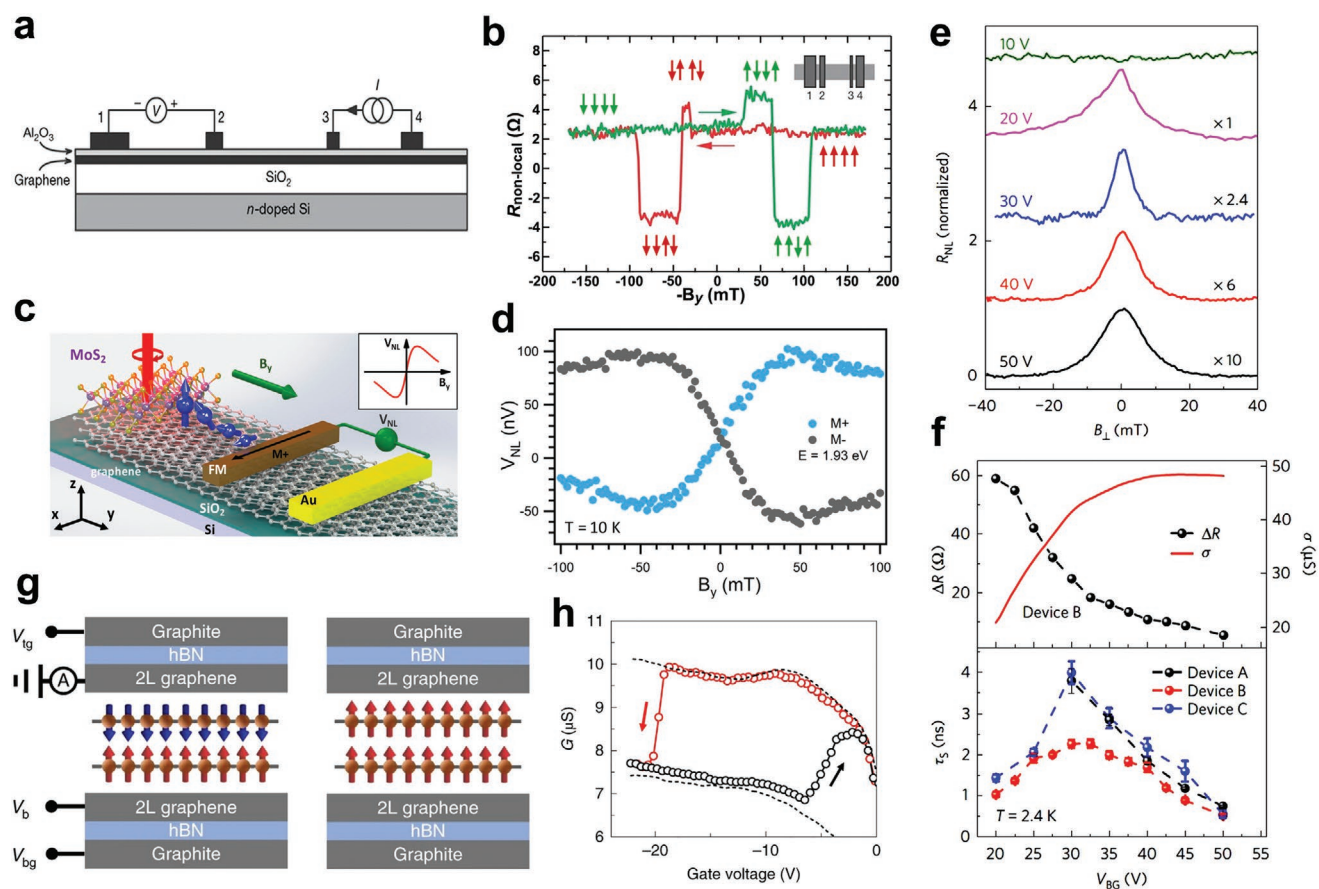


**Figure 4.** a) Nonlocal spin valve geometry based on graphene channel. b) Non-local resistance measured from the lateral spin valve when sweeping the magnetic field. The magnetization states of different electrodes are illustrated by arrow. a,b) Reproduced with permission.<sup>[106]</sup> Copyright 2007, Springer Nature. c) Illustration of MoS<sub>2</sub>/few-layer graphene heterostructure as well as optical spin injection, spin transport and detection process. d) Electrical measurement result of the optical spin injection using A exciton resonance energy at 1.93 eV. c,d) Reproduced with permission.<sup>[114]</sup> Copyright 2017, American Chemical Society. e) Measured Hanle spin precession curves under different back-gate voltage of the nonlocal spin valve with black phosphorus channel. f) Back-gate voltage dependence of spin relaxation time, nonlocal resistance and conductivity measured at 2.4 K. Reproduced with permission.<sup>[120]</sup> Copyright 2017, Springer Nature. g) Sketch of the graphene/MoS<sub>2</sub> non-local spin valve. h) Gate voltage dependence of the nonlocal resistance showing clear ON/OFF state. g,h) Reproduced with permission.<sup>[129]</sup> Copyright 2019, Springer Nature.

the conductance mismatch at the interface.<sup>[107–110]</sup> Barriers including oxides and boron nitride are introduced to achieve tunnel spin injection.<sup>[111–113]</sup> For example, pin-hole free strontium oxide was grown on graphene as the tunnel barrier, which achieved long spin relaxation time exceeding 1 ns.<sup>[113]</sup> Despite this, new routes have been under spotlight. For example, Luo et al. fabricated MoS<sub>2</sub>/graphene heterostructure and succeeded in spin injection from MoS<sub>2</sub> to graphene by illuminating circularly polarized light (Figure 4c,d).<sup>[114,115]</sup> Spin-polarized excitons were generated for the valley selection rules and then the polarized holes were injected into graphene due to the designed band alignment. This method provides a way to the optically mediated spin injection, and enables an ultrafast spin injection process. Moreover, utilizing the strong SOC in TMDs (WSe<sub>2</sub>, MoSe<sub>2</sub>) or heavy metals (Pt), spin Hall effect (SHE) as well as inverse spin galvanic effect (ISGE) are employed to generate spin current from charge current.<sup>[116–118]</sup> For example, Yan et al. used Pt as the electrode to realize electrically spin injection and detection with SHE and ISHE.<sup>[118]</sup> According to their calculation, their device had largest spin-to-charge conversion

signal compared with previous reported spin Hall metals with different metallic channels. This enhancement can be attributed to great spin transport ability of graphene. In addition to the intrinsic strong SOC, the proximity effect can be used to modify the properties of the neighboring materials to enhance the spin-to-charge interconversion. To further reveal the interconversion mechanism, Valenzuela et al. built a WS<sub>2</sub>/graphene heterostructures and specially designed the measurement circuit, which enable to separate the contributions of the SHE and ISGE.<sup>[119]</sup> Based on the spin precession experiment, they found that the efficiency of spin-to-charge conversion in graphene was tremendously enhanced by proximity effect. The proximity effect induced a complex spin texture in graphene, causing anisotropic spin dynamics and spin-orbit interaction. In addition, these two effects can both be modulated by gate voltage, providing new strategies for electrically controlled spin information. Although graphene is an excellent spin channel, the zero-bandgap nature restricts its applications in the semiconductor spintronic devices like spin diodes or spin transistors. Thus, Avsar et al. adapted semiconductor black phosphorus to

replace graphene as the spin channel and measured its spin transport properties,<sup>[120]</sup> which exhibited long spin relaxation length exceeding 6  $\mu\text{m}$  (Figure 4e,f). Moreover, their spin transport properties are highly correlated with the carriers concentration, thus enabling the gate modulation process. Therefore, they investigated the gate bias dependence of nonlocal resistance, which showed increasing resistance with decreasing gate voltage. This behavior can be understood by tunneling spin injection. The semiconductor nature with considerable spin transport performance proved the potential of black phosphorous for spintronics.

The proximity effect could also be applied for manipulating the spin transport process.<sup>[121,122]</sup> For example, the high SOC in the TMDs materials can induce spin dephasing and thus modulate the spin current in graphene such as  $\text{WS}_2/\text{graphene}$  heterostructure.<sup>[123]</sup> In addition, the proximity effect can also enhance the SOC as mentioned before. Except for the TMDs, topological insulator  $\text{Bi}_2\text{Se}_3$  flakes were also predicted to induce large SOC in graphene by proximity effect and were verified by Khokhriakov et al.<sup>[124]</sup> These methods are all gate tunable, demonstrating the proximity effect a satisfying way to manipulate the spin current.

## 4.2. Spintronics Enhanced by 2D Magnets

### 4.2.1. Magnetism in the 2D Limit

Generally, the spintronic devices mentioned above utilized the unique properties of the 2D materials like the varying SOCs. Despite these factors, it is of great importance to find low-dimensional materials with pristine magnetism, which will provide more fascinating spin–matter interactions and broaden the spintronic application scenarios in data storage, sensors, and etc. As discussed in Section 3, several methods have been used to introduce magnetism extrinsically. Unfortunately, most of the defect engineering only resulted in localized magnetic moments. The long-range ferromagnetic order is still absent for the lack of exchange interaction between the localized magnetic moments. Although the magnetic proximity effects were used to introduce long-range magnetism in unpolarized 2D materials, the bulk nature of magnetic substrate restricts their application in spintronics. Compensating the thermal fluctuation from the Mermin-Wagner theorem, the anisotropic effect has been proved by the discovery of intrinsic ferromagnetic 2D  $\text{Cr}_2\text{Ge}_2\text{Te}_6$  and  $\text{CrI}_3$  in 2017.<sup>[113,125]</sup> This newly developed 2D ferromagnetism, and recent discovered ferromagnetic layered materials, such as  $\text{CrBr}_3$ ,  $\text{CrSe}$ ,  $\text{Fe}_3\text{GeTe}_2$ , and  $\text{VSe}_2$ , have greatly attracted the worldwide attentions.<sup>[77,126–128]</sup> New technologies have been developed to recognize the 2D magnetism. It was found that in  $\text{Cr}_2\text{Ge}_2\text{Te}_6$ , the Curie temperature increased with the thickness, which suggested the interlayer magnetic coupling play an important role in the 2D ferromagnetism.<sup>[125]</sup> Based on the employed Heisenberg model, the ferromagnetic order happened in 3D system will be strongly destroyed by thermal fluctuations of the long-wavelength gapless spin-wave excitation in 2D counterpart. However, the magnetic anisotropy establishes the 2D ferromagnetic order through breaking the continuous rotational symmetry of the Hamiltonian, leading to a nonzero

excitation gap in the lowest-energy acoustic magnon mode. By comparison, the monolayer  $\text{CrI}_3$  exhibited Ising-type ferromagnetism below Curie temperature, which showed strong uniaxial magnetic anisotropy.<sup>[13]</sup> Moreover, unlike  $\text{Cr}_2\text{Ge}_2\text{Te}_6$ ,  $\text{CrI}_3$  has layer-dependent magnetic order with opposite spin polarization in adjacent layers due to AFM structure. This unique property provides numerous chances for modulating the ferromagnetism and then offers opportunities in spintronics. Except for the theory development and materials discovery, these 2D ferromagnetic crystals inspire great motivation to the development of 2D spintronics. Different methods on manipulating these 2D magnetism have been developed, which introduce great possibilities in spintronic devices as mentioned below.

### 4.2.2. Spintronic Devices Based on 2D Magnetic Materials

In this section, we focus on the coupling of magnetic order and spin transfer characters in 2D magnetic materials, including the electrostatically tuned magnetic orders, the magnetic field tuned spin transfer, and recent developed 2D magnet-based devices.

Based on the unique properties of these magnetic layers, various vdW heterostructures and corresponding spintronic devices were fabricated. As a fundamental device of the spintronics, the vdW magnetic tunnel junctions (MTJ) are mostly investigated. Composing of two ferromagnetic layers separated by a tunnel barrier, the MTJ utilize the tunnel magnetoresistance (TMR) effect. Thus, the uniform thickness of the 2D barrier layers can achieve homogeneous tunnel resistance and the sharp interface between the layers will provide high electronic quality.

Specifically, for the  $\text{Fe}_3\text{GeTe}_2/\text{hBN}/\text{Fe}_3\text{GeTe}_2$  MTJ, the two  $\text{Fe}_3\text{GeTe}_2$  layers act as the ferromagnetic electrodes while the hBN layer serve as the tunneling barrier.<sup>[71]</sup> A textbook tunnel junction behavior is observed with minimum (maximum) MR in the paralleled (antiparalleled) magnetic state of the two electrodes, as demonstrated by the anomalous Hall test. Herein,  $\text{Fe}_3\text{GeTe}_2$  layers differing in thickness is employed for diverse coercivity, which is crucial to achieve antiparalleled magnetization states. Based on the antiferromagnetic and insulating characteristics of multilayer  $\text{CrI}_3$ , another kind of MTJ is designed. Song et al. fabricated graphene/ $\text{CrI}_3$ /graphene heterostructures as spin-filter MTJs.<sup>[19]</sup> In these devices, the magnetization state of different layers in  $\text{CrI}_3$  is switched with external magnetic fields, resulting in different magnetic alignment of the  $\text{CrI}_3$  layers and magnetoresistance. They investigated similar devices with bilayer, trilayer, and four-layer  $\text{CrI}_3$  as tunneling barriers. A tremendous tunnel magnetoresistance as large as 19 000% can be achieved in four-layer  $\text{CrI}_3$  devices. The recording TMR was attributed to the intrinsic layer-by-layer AFM ordering of the  $\text{CrI}_3$ , where the antiparalleled AFM configuration performed as spin filters in serial to suppress the tunneling current. However, large magnetic field up to 2.5 T was applied to achieve such high TMR and the devices were measured at 2 K, which remains a difficult obstacle for practical applications. In order to clarify the electron tunneling mechanism in these heterostructures, Ghazaryan et al. fabricated graphene/ $\text{CrBr}_3$ /graphene heterostructure and performed detailed researches.<sup>[126]</sup>

The revealed tunneling process is mainly assisted by magnon emission process, which may offer new opportunities to spin injection. In addition, Jiang et al. adapted similar heterostructure with dual gate to construct a spin tunnel FET.<sup>[129]</sup> At different gate voltage, the spin-flip transition field of the CrI<sub>3</sub> was modulated (Figure 4g). Therefore, they utilize these properties to control the tunnel conductance at fixed magnetic field by varying the gate voltage. They succeed in repeatedly switching between high and low conductance state only by gate control, which offered new opportunities for magnetic memory devices (Figure 4h). Still, there exists similar problem that the device shall be operated at low temperature and high magnetic fields. Hopefully, there have been researches studying the room temperature magnets and manipulating the magnetic orders in the absence of external magnetic fields.

### 4.3. Manipulation of Magnetic Orders

As discussed above, manipulating the magnetic orders of the atomic thin ferromagnetic layers in the spintronic devices is of great importance. Although we can apply magnetic field to control the magnetic orders, it is more compatible in solid state circuits to use electrical methods to realize the manipulation. Several strategies have been investigated. Jiang et al. succeeded in controlling the magnetic states of both monolayer and bilayer CrI<sub>3</sub> through electrostatic doping.<sup>[69]</sup> To perform this, graphene/CrI<sub>3</sub>/graphene heterostructure encapsulated by hBN was fabricated (Figure 5a). When applying gate voltage, the saturation magnetization as well as the coercive force of the monolayer CrI<sub>3</sub> was tuned. The bilayer CrI<sub>3</sub> nanoflakes, which are

antiferromagnetic intrinsically, will change into ferromagnet by enough electron doping of  $\approx 2.5 \times 10^{13} \text{ cm}^{-2}$  (Figure 5b). But the carrier concentration correlated microscopic mechanism still need further exploration. In addition, Zhang et al. manipulated the ferromagnetism in Cr<sub>2</sub>Ge<sub>2</sub>Te<sub>6</sub> with both ionic gating and Si back gate (Figure 5c).<sup>[71]</sup> Below the Curie temperature, the hysteresis loop changed under hole doping, with enhanced saturation magnetization and reduced saturation field (Figure 5d). Using the first-principles calculations and micromagnetic simulations, they concluded the variation to the band structure rebalance as the doping influence the Fermi levels of the Cr<sub>2</sub>Ge<sub>2</sub>Te<sub>6</sub> nanoflakes.

Despite the gate control, other electrical methods were also investigated. For example, Alghamdi et al. utilized spin-orbit torque (SOT) effect to manipulate the magnetism of Fe<sub>3</sub>GeTe<sub>2</sub> through Pt film (Figure 5e).<sup>[130]</sup> According to the SOT effect, the spin current arisen from in-plane charge current via large spin-orbit coupling introduces torque to violate the magnetization. In this heterostructure, Pt film with strong SOC enables the charge-to-spin conversion. Moreover, the sharp interface of vdW heterostructure guarantees high SOT efficiency. After the spin current entering the Fe<sub>3</sub>GeTe<sub>2</sub> layer, the accumulated spin-polarized electron will apply field-like and damping-like torque for the magnetization. Finally, magnetization switch was observed through anomalous hall effect. This SOT effect manipulation provided more opportunities for engineering magnetism (Figure 5f).

In addition, the magnetic ground state in 2D polarized materials is closely connected to the crystal structure. After applying hydrostatic pressure, the CrI<sub>3</sub> crystals transform from the monoclinic phase to the rhombohedral phase.<sup>[131]</sup> The theory

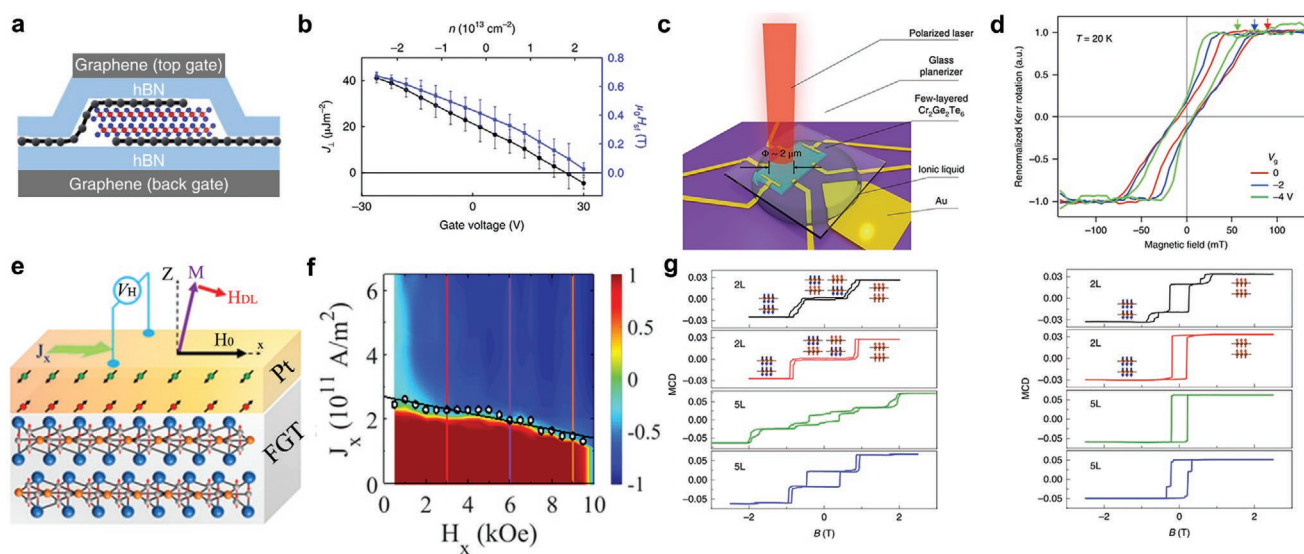


**Figure 5.** a) Schematic of dual-gate field effect devices based on bilayer CrI<sub>3</sub>. b) Interlayer exchange constant  $J_{\perp}$  and spin-flip transition field  $H_{sf}$  measured under different gate voltage. Antiferromagnetic-to-ferromagnetic transition happened at doping intensity of  $\approx 2.5 \times 10^{13} \text{ cm}^{-2}$ . a,b) Reproduced with permission.<sup>[69]</sup> Copyright 2018, Springer Nature. c) Schematic diagram of ionic gating few-layer Cr<sub>2</sub>Ge<sub>2</sub>Te<sub>6</sub> device for Kerr measurement. d) Renormalized Kerr rotation angle of the device in c) under 0, -2, -4 V gate voltage at 20 K. c,d) Reproduced with permission.<sup>[71]</sup> Copyright 2018, Springer Nature. e) Illustration of method to switch magnetization state of Fe<sub>3</sub>GeTe<sub>2</sub> via effective magnetic field from SOT. f) Effective switching current as a function of applied in-plane positive bias field. e,f) Reproduced with permission.<sup>[130]</sup> Copyright 2019, American Chemical Society. g) Magnetic circular dichroism as a function of magnetic field of bilayer and five-layer CrI<sub>3</sub> before (left) and after (right) applying pressure recorded at 3.5 K. The difference indicated pressure induced AF-FM phase transition. Reproduced with permission.<sup>[131]</sup> Copyright 2019, Springer Nature.

has been verified by the polarization Raman spectrum, accompanied with the magnetic ground state of bilayer CrI<sub>3</sub> experiencing an AFM-FM phase transition (Figure 5g).

#### 4.4. Outlook of 2D Magnets

Although researches on 2D ferromagnets are still in the initial stage, the fascinating results have exhibited the great potential lying behind. Toward the practical application of 2D magnets in spintronics, there are still required further investigation. The most basic requirement is the realization of room-temperature ferromagnetism in 2D magnetic materials. Although some 2D room temperature magnets have been discovered (Figure 6a,b), such as monolayer VSe<sub>2</sub>, MnSe<sub>2</sub>, and Fe<sub>3</sub>GeTe<sub>2</sub>, it is still not enough to satisfy variety of spintronic devices. New kind of materials have been predicted such as tetrahedral semiconductor CrC (Figure 6c).<sup>[77,132–135]</sup> Additionally, these materials were all fabricated by MBE or exfoliation method, which are still not suitable for large-scale integration. Therefore, fabrication methods need urgent development. Besides, new 2D room-temperature magnetic materials with different conductivity, especially ferromagnetic semiconductors, need to be developed. The ferromagnetic semiconductors enable the concurrent manipulation of both charge and spin current, which will greatly enhance the functionality for logic

devices and information storage applications. In addition, new methods to manipulate the magnetism, including electrical, mechanical, and optical methods, need to be developed. For instance, there have been predicted that monolayer RuCl<sub>3</sub> will be switched from spin-liquid phase to ferromagnetic phase by light (Figure 6d).<sup>[136]</sup> According to their analysis, this was achieved through the excitons induced lattice strain and itinerant ferromagnetism. This result gives a brand-new way to optically control of magnetism.

Toward the development in the practical applications, new device concepts shall be developed to exploit the full potential of 2D magnets. This can be realized by the combination with other 2D materials, which incorporate different characteristics, to build multifunctional devices. For example, Cardoso et al. propose a vdW spin valve composed of two insulating ferromagnetic layers separated by conducting layers. Because of the proximity effect, the conductance of the layers in the middle strongly relies on the magnetization states of the nearby insulating layers. Inspired by this characteristic, they predicted the on/off states of the conducting layers can be switched by converting the magnetization of the nearby layers from parallel to antiparallel, which show great potential in memory device (Figure 6e).<sup>[137]</sup> In conclusion, the discovery of 2D magnetic crystals not only boost the fundamental researches but also broaden the opportunities in 2D spintronics.

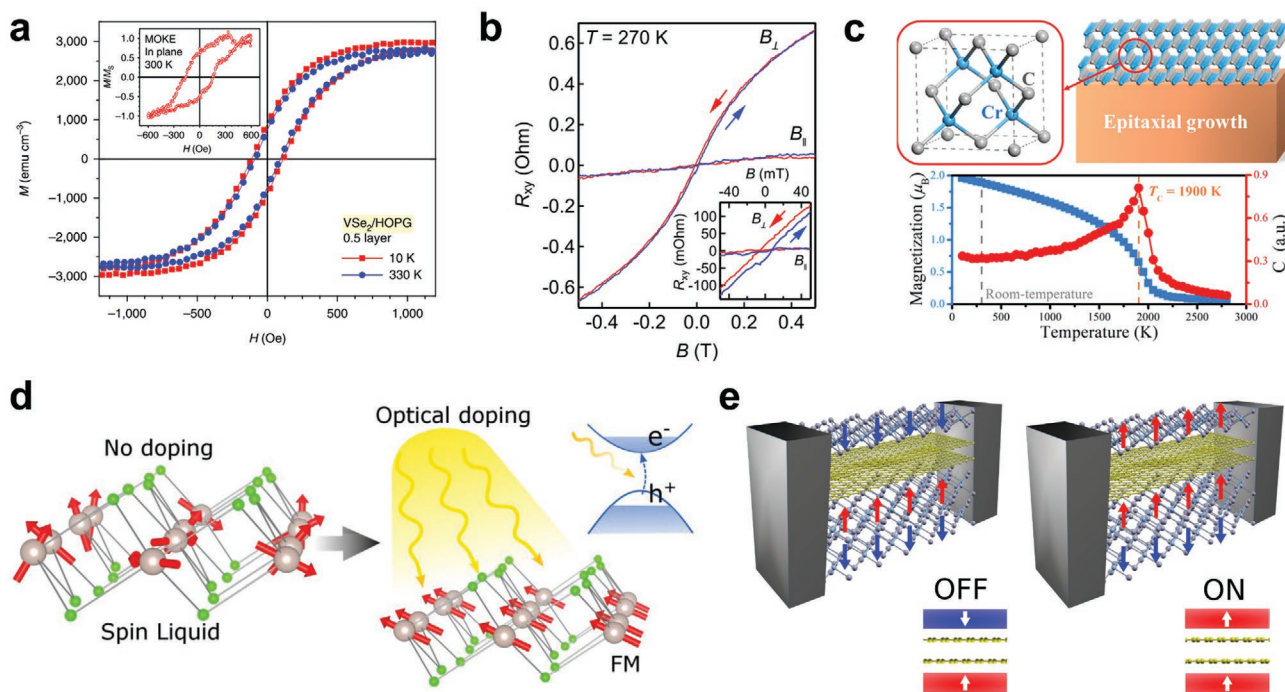


**Figure 6.** a) Magnetization-magnetic field hysteresis loop for VSe<sub>2</sub> on highly oriented pyrolytic graphite (HOPG) measured at 10 and 330 K. The inset shows the in-plane longitudinal magneto-optic Kerr effect at 300 K. Reproduced with permission.<sup>[77]</sup> Copyright 2018, Springer Nature. b) Parallel and antiparallel magnetic field dependence of anomalous Hall resistance of thin Fe<sub>3</sub>GeTe<sub>2</sub> flake. Reproduced with permission.<sup>[134]</sup> Copyright 2019, American Chemical Society. c) Illustration of a room temperature ferromagnet candidate CrC. Reproduced with permission.<sup>[135]</sup> Copyright 2019, American Chemical Society. d) Schematic of optical doping induced ferromagnetism in RuCl<sub>3</sub>. Reproduced with permission.<sup>[136]</sup> Copyright 2019, American Chemical Society. e) Schematic of a vdW spin valve with lateral electrical contacts, which is composed of a conducting layer sandwiched between two insulating ferromagnets. The in-plane conductance of the device strongly depends on the magnetization configuration of the two ferromagnetic crystals. Reproduced with permission.<sup>[137]</sup> Copyright 2018, American Physical Society.

## 5. Ferrovalley Materials and 2D Valleytronics

### 5.1. Valleytronics in 2D Materials

Compared with spin DOF arising from the intrinsic behavior of electrons, valley DOF indicates the occupation of the energy bands extremum. Recently, the rise of exploration on novel DOF of electron attracts large interests. The new DOF provides tremendous potential for information coding and manipulation in electronic devices. The degenerate valleys in material can be regarded as discrete DOF as they are able to be polarized and distinguished. Therefore, 2D valleytronics is developed recent years, which employs valley DOF for information manipulation. For example, there are two highly symmetrical Dirac points ( $K$  and  $K'$ ) in graphene and the hexagonal lattice has two different sublattices A and B (Figure 7a). The degeneracy at the two  $K$  and  $K'$  valleys are protected by the time- and spatial inversion symmetry. To obtain valley-dependent optical and transport properties, TMDs are usually introduced for the broken spatial-inversion symmetry and strong SOC. For the lifted degeneracy, the valley polarization can be obtained under the excitation of circular polarized light, which makes them a keypoint for valleytronics application.

The manipulation of valley index for encoding and operating information is crucial in valleytronics. Optical selection is opposite in two valleys because of the reversed Berry curvature  $\Omega$ , which gives a path to generate correlated valley polarization and imbalanced valley carries density. Here, a brief introduction

of  $\Omega$  is given to help understand the optical selection rules. Berry curvature occurs in semiclassical dynamics, where a nonadiabatic perturbation gives a modification to the adiabatic dynamics, called anomalous velocity.<sup>[138]</sup> Similarly, when applying an electric field  $E$  upon the crystal, apart from group velocity, electrons will get an anomalous velocity<sup>[139]</sup>

$$v_a = \frac{e}{\hbar} E \times \Omega \quad (15)$$

where  $e$  and  $\hbar$  denote the elementary charge and the Planck constant, respectively. So the Berry curvature can be considered as a magnetic field on rotating the electrons. Due to the broken spatial-inversion symmetry in monolayer TMDs,  $\Omega$  has opposite sign for the  $K$  and  $K'$  points (Figure 7b). Therefore, when an electric field is applied, the carriers at  $K$  and  $K'$  valleys will be deflected into different directions, thus inducing valley Hall effect (VHE, Figure 7c,d).<sup>[140–142]</sup>

The photoexcited electron–hole pairs will form a hydrogen-like bound state through strong Coulomb interactions known as the exciton (Figure 7e). Therefore, optical selection rules for excitons can be explained by hydrogen model. In this model, steady state Schrodinger equation of exciton can be divided into the radial part and the angle part.

Thus, exciton state is indicated by  $(n,m)$ , where  $n = 0,1,2,\dots$  is radial quantum number and  $m = 0, \pm 1, \pm 2,\dots$  is the angular momentum quantum number. The bright excitons have angular momentum  $m = w \pm \tau$  for  $\sigma^+$  ( $\sigma^-$ ) light, respectively, where  $w$  is phase winding number, a topological property of the

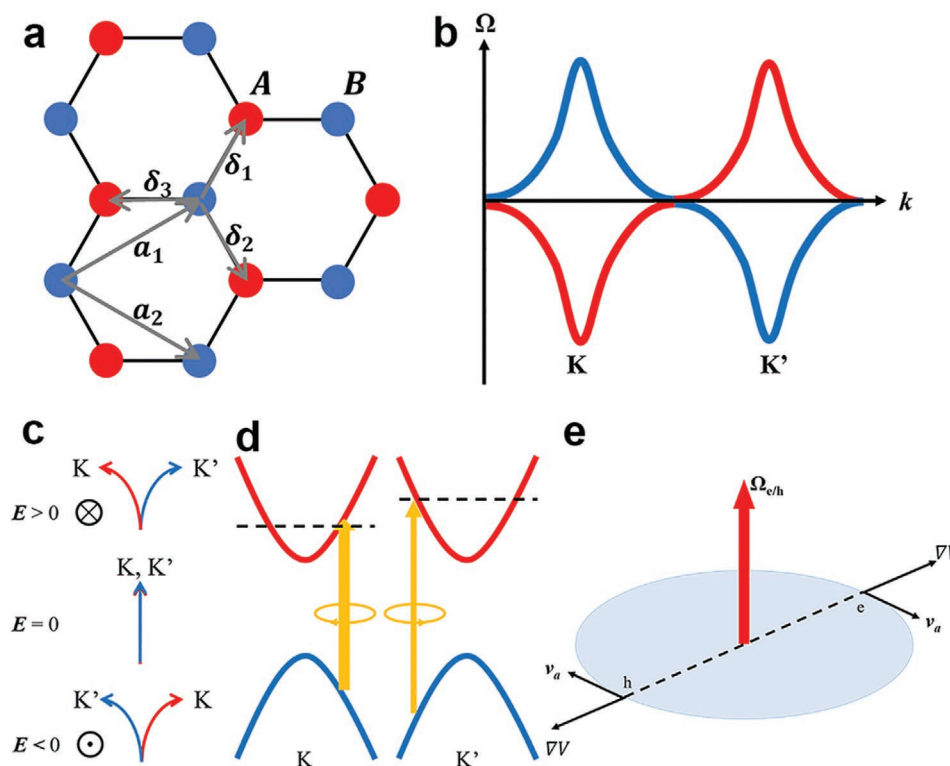


**Figure 7.** a) The crystal structure of graphene. The red and blue balls are representative of sublattices A and B, respectively. b) The distribution of Berry curvature for the conduction (blue) and valence band (orange) near the  $K$  and  $K'$  points. c) Effect of  $E$  on the VHE. d) The imbalance of electrons at  $K$  and  $K'$  points. e) The schematic diagram of the exciton formation under a central potential  $V$ .

Bloch bands ( $= 1$  in monolayer TMDs) and  $\tau$  is valley index ( $+1$  for  $K$ ,  $-1$  for  $K'$ ). And for dark excitons ( $m = 1$ ), an anomalous velocity caused by the Berry curvatures breaks time-reversal symmetry in each valley and further leads to the energy splitting ( $m = 1$  or  $m = -1$ ).<sup>[144–147]</sup> Hence, the spin state of an exciton  $S_z = \pm 1$  is correlated with its valley state  $K$  ( $K'$ ), and applying circularly polarized light can preferentially inject excitons into one valley, which generates population difference of excitons in the two valleys.<sup>[142]</sup>

The suppressed valley depolarization and sufficient valley lifetime ensures the device operation and information storage for high-performance practical application of valleytronics. Experiments have revealed relatively short valley lifetime ( $\tau_v < 10$  ps) at low temperatures, and much shorter at higher temperature (e.g., 1.5 ps at 125 K for monolayer WSe<sub>2</sub>).<sup>[148]</sup> The strong electron–hole Coulomb exchange interaction is to blame for the fast depolarization. So that many efforts have been made to achieve long-lived valley pseudospin to meet the requirements of valleytronics. An  $\approx 1$  ns-lifetime valley polarization for positive trion (charged excitons) was demonstrated in CVD-grown monolayer WSe<sub>2</sub> at low temperature (Figure 8a). The time-scale of valley polarization is much longer than the recombination time of trion ( $\approx 10$ – $20$  ps).<sup>[149]</sup> In this system, valley pseudospin

could transfer from photocarriers to resident holes, which enables such a long lifetime of valley polarization. Thus, long-lived valley-polarized holes was first created and observed in monolayer WSe<sub>2</sub>. The transfer of valley pseudospin occurs when lifetimes of the photogenerated electrons and holes differ widely from each other, or through defect assisted nonradiative recombination processes. The defect levels will capture photogenerated electrons and holes, then slow the recombination process of excitons. By applying electron-beam irradiation on monolayer WSe<sub>2</sub>, defects of selenium vacancies were created. Excitons would further bound to these defects making a large recombination time of 200 ns, which largely prolongs the valley polarization to 1  $\mu$ s (Figure 8b).<sup>[150]</sup> The engineering of crystal lattice provides a defect resonance to the emission spectrum below the delocalized exciton. Novel spin and valley dynamics of TMDs may be uncovered by resonant nonlinear optical spectroscopy. Singh et al. tuned resonant pump-probe energy across the trion resonance and observed both intravalley and intervalley trions in monolayer WSe<sub>2</sub>. The lifetime of intravalley trion valley polarization is  $\gg 25$  ps, which is beyond the measuring range of experimental setup. But the intervalley trion valley lifetime is just  $\approx 4$  ps (Figure 8c). Figure 8d shows the conversion and valley dynamics of various excitons and trions.

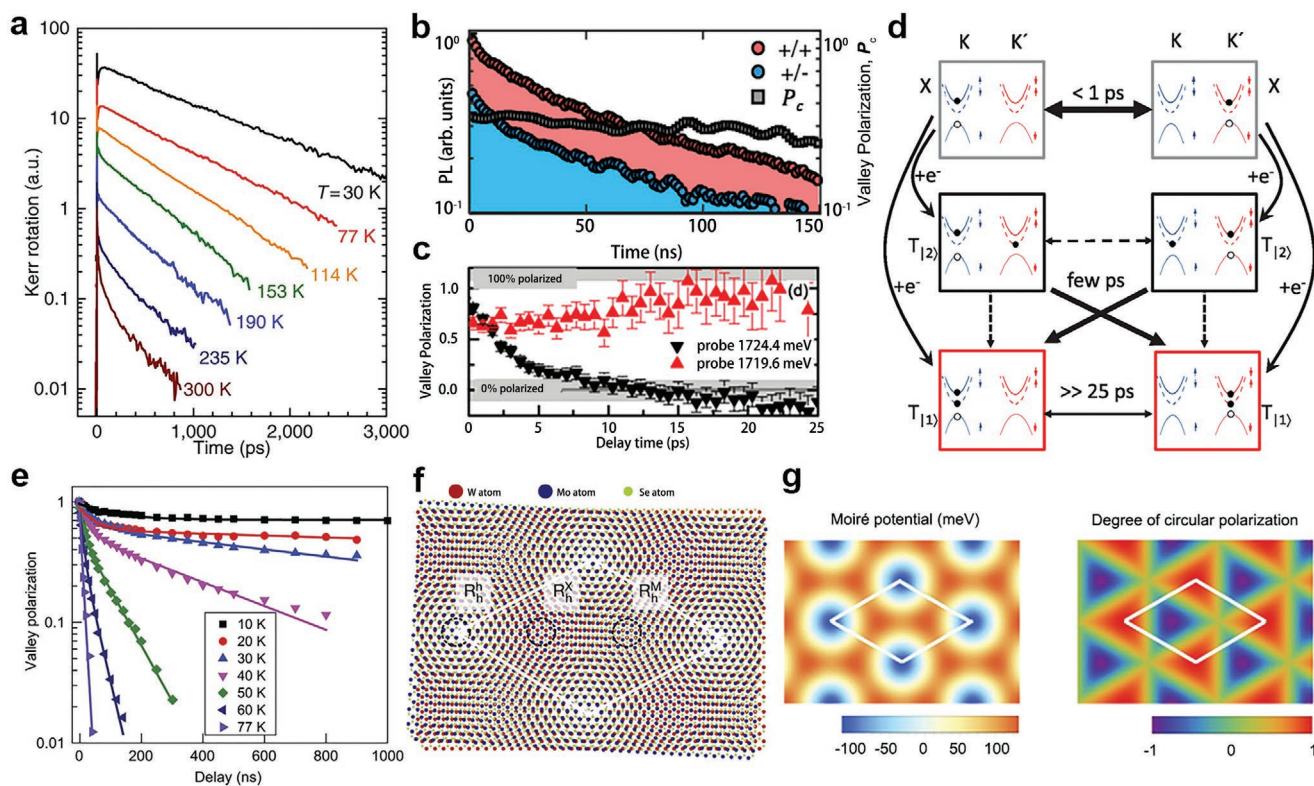


**Figure 8.** a) The time-resolved Kerr rotation measurement of WSe<sub>2</sub> under different temperatures. Reproduced with permission. Reproduced under the terms of the CC-BY 4.0 License.<sup>[149]</sup> Copyright 2015, the Authors, published by Springer Nature. b) The PL measurement of valley polarization of WSe<sub>2</sub> with defects. Reproduced with permission.<sup>[150]</sup> Copyright 2018, American Physical Society. c,d) Valley polarization measurements for intra- and intervalley excitons of WSe<sub>2</sub>. Schematic of the suggested valley polarization dynamics. Reproduced with permission.<sup>[151]</sup> Copyright 2016, American Physical Society. e) Delay of valley polarization of WSe<sub>2</sub>/MoS<sub>2</sub> under different temperature from 10 to 77 K. Reproduced with permission. Reproduced under the terms of the CC-BY 4.0 License.<sup>[152]</sup> Copyright 2017, the Authors, published by AAAS. f,g) Schematic of atomic alignments of MoSe<sub>2</sub>/WSe<sub>2</sub> heterostructure with a small twist angle. The moiré potential of the interlayer exciton transition, and map of the optical selection rules for excitons at  $K$  point. Reproduced with permission.<sup>[153]</sup> Copyright 2019, Springer Nature.

For intravalley negative trion, scattering of *K* valley requires the simultaneous transfer of three carriers (two electrons and a hole) to the other valley, which is hard to be realized due to the restriction of energy. So the intravalley trion valley polarization in the experiment is stable, referring to relatively long polarization lifetime.<sup>[151]</sup>

As mentioned above, valley lifetime of excitons in TMD monolayers is largely influenced by the electron–hole exchange interaction. But individual electrons or holes is not affected by this mechanism and will get longer lifetime. In case of type-II TMDs heterostructures, electrons and holes are fast separated into different layers and result in electron/hole doping, which largely restrains the electron–hole exchange interaction. This phenomenon extends the valley lifetime. A research was conducted in the system of type-II WSe<sub>2</sub>/MoS<sub>2</sub> heterostructure and the valley lifetime was characterized.<sup>[152]</sup> The imbalance of population decay time of holes is more than 1 μs and the valley lifetime is >40 μs at 10 K (Figure 8e). LCP selectively creates excitons at *K* valley in WSe<sub>2</sub> layer, then the electrons transfer to the MoS<sub>2</sub> layer within 50 fs leaving the hole valley polarization in WSe<sub>2</sub> layer. Moreover, some delighting properties can be realized by twisting the two layer TMDs in a specific angle to form a moiré superlattice. Multiple interlayer exciton resonances was observed in hBN-encapsulated MoSe<sub>2</sub>/WSe<sub>2</sub> heterostructure (Figure 8f,g).<sup>[153]</sup> In this structure, the moiré potential is mediated through the twisted angle. When slightly changing the twist angle, variation trend of the energy spacing and lifetime of the interlayer excitons are accord with the effect of the moiré potential. The transition of electron in larger twist angle is more indirect in momentum space and leads to longer lifetime, which is crucial for the long-term storage and information processing in valleytronics. When the twist angle is set as 1°, PL spectrum declares four interlayer exciton resonances peaks, which might imply the lateral confinement caused quantized energy levels.

We mentioned the vector of pseudospin *S* above, where the out-of-plane component *S<sub>z</sub>* describes the spin states of exciton and the in-plane component *S<sub>x,y</sub>* describes the coherent superposition of exciton valley states.<sup>[154]</sup> The evidence of exciton valley coherence is the luminescence of linearly polarized light, as the exciton from one valley only emits circularly polarized light. The manipulation of coherence of pseudospins is also critical for spintronics and valleytronics. The coherence of the *K* and *K'* valley excitons was first observed in monolayer WSe<sub>2</sub> via PL spectrum.<sup>[155]</sup> Thus, direct measurement of the valley coherence of excitons becomes a great task. Polarization-resolved optical 2D coherent spectroscopy (2DCS) was employed to study the valley coherence of excitons in monolayer WSe<sub>2</sub> (Figure 9a).<sup>[156]</sup> It is found that the valley coherence time has great matter with exciton lifetime, and is limited by the electron–hole exchange interaction. Embedding in optical microcavities provides a new way for detecting and controlling valley pseudospin. In this approach, part-light-part-matter exciton-polaritons are formed because of strong coupling between excitons and the cavity mode. Dufferwiel et al. formed a part-light-part-matter exciton-polaritons by embedding monolayer WSe<sub>2</sub> into optical microcavity.<sup>[156]</sup> They further discovered a luminescence three times higher than that of bare excitons as stimulated by linear polarized light (Figure 9b). And the polariton lifetime is about

5–10 ps (≈1 ps for bare exciton), with fitted coherence time of 0.52 ± 0.05 ps. In brief, the short valley coherence time limits the applications in spintronics and valleytronics, hence more need to be done to solve the restriction in coherence time.

Recently, the concepts of ferrovalley materials are proposed as a new member of ferroic family. This new member possesses spontaneous valley polarization, leading to the presence of additional charge Hall current (anomalous valley Hall effect). Due to anomalous valley Hall effect, the electrically reading and magnetically writing memory devices are coming up (Figure 9c). The binary information is stored by the valley polarization of the ferrovalley material that could be controlled by the magnetic moment through an external magnetic field. The memory based on ferrovalley materials has the advantage in nonvolatility in contrast to conventional valleytronic materials, which makes it a great candidate for practical applications of valleytronics. The early researches show that 2H-VSe<sub>2</sub> and GeSe are good candidates for ferrovalley memories.<sup>[42,157]</sup> Whereas the experimental efforts on 2H-phase V-group dichalcogenides are strongly advocated, where the related valley physics and valleytronic devices need to be achieved. Furthermore, recent ferrovalley researches are mostly based on the homogenous materials, the heterostructure systems based on polarized materials and 2D channels may provide many interests for the future study in valleytronics.

## 5.2. Modulation of the Valley DOF: Valley Zeeman Effect

The monolayer TMDs such as WSe<sub>2</sub> usually plays an important role in valleytronics as valley-semiconductor. Herein, due to the pseudospin nature, many researches focus on modulating the valley degeneracy by valley Zeeman effect. Zeeman effect indicates the magnetic field induced, valley-dependent linear shift of the exciton resonance of  $-\tau\Delta(B)/2$ , where  $\Delta(B) = 2(2 - \Delta\alpha)\mu_B B$ , where  $\Delta\alpha = \alpha_c - \alpha_v$  ( $\alpha = m_0/m^*$ , *c* means conductive band and *v* means valence band, *m\** is effective mass) (Figure 9d). Thus, in the magnetic field modulated polarized PL spectra, *K* valley exciton should be red shifted with respect to the *K'* valley exciton for *B* > 0, and blue shifted for *B* < 0.<sup>[158]</sup> In 2015, Srivastava et al. reported valley Zeeman effect in monolayer WSe<sub>2</sub>.<sup>[159]</sup> In this experiment, circularly polarization-resolved PL and magnetic field in Faraday geometry are used to examine the valley splitting.

The magnetic-field dependence of exciton photoluminescence spectra is shown in Figure 9e, where the *B* dependent splitting of *X*<sup>0</sup> and trion (*X*<sup>-</sup>) peaks were meanwhile observed. Both the splitting of *X*<sup>0</sup> and *X*<sup>-</sup> increases linearly with *B*, and the slope for trion (0.32–0.36 meV T<sup>-1</sup>) is larger than that in *X*<sup>0</sup> (0.25 meV T<sup>-1</sup>) (Figure 9f).<sup>[159]</sup> Considering the charged nature, the introduction of extra electrons/holes inevitably promotes the magnetic moment of trions. The valley Zeeman effect demonstrated in this work establishes the valley degree of freedom as a pseudospin index. The subsequent studies consider on enlarging the control of valley pseudospin, where the electronic doping is usually employed. In recently 2019, Yu's group built MoS<sub>2</sub>/WS<sub>2</sub> heterostructure and found a strongly enhanced valley magnetic response in MoS<sub>2</sub>.<sup>[160]</sup> The enhancement is attributed to the changed spin-valley degeneracy from

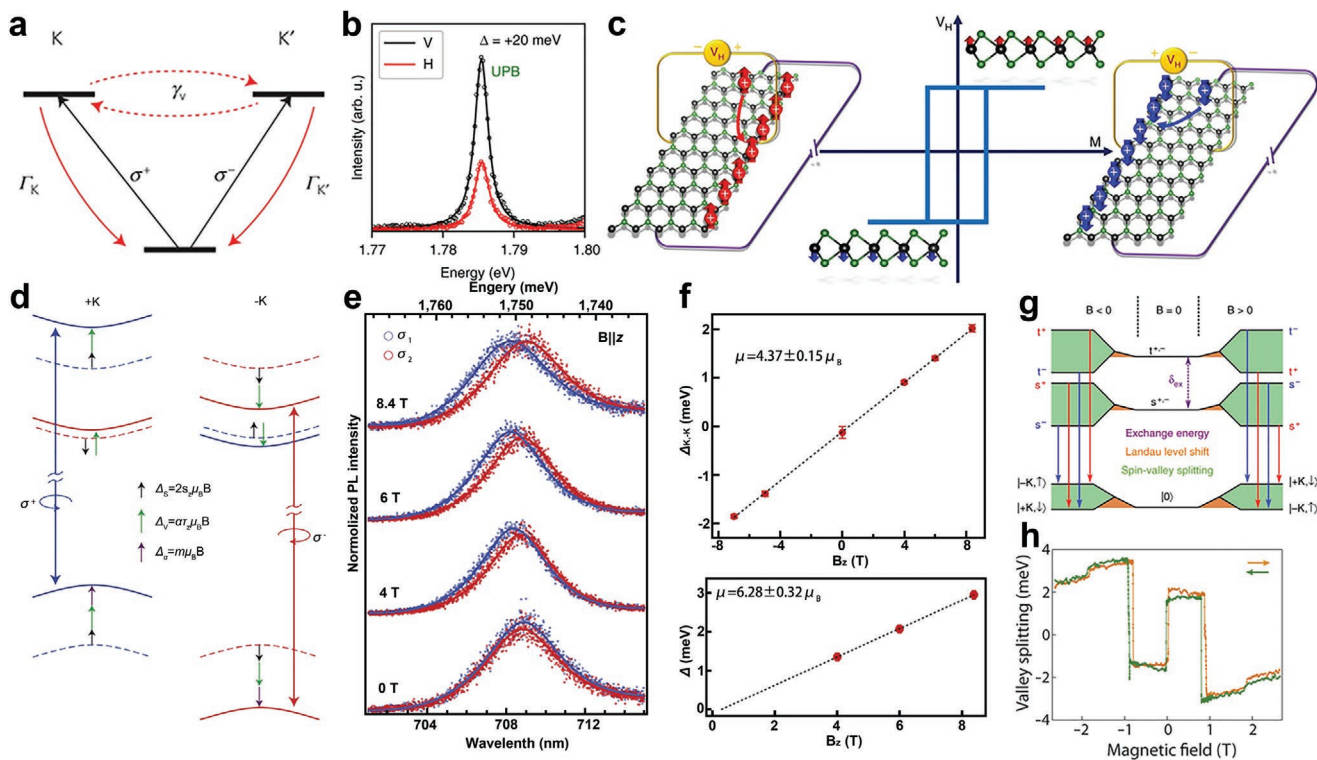


**Figure 9.** a) Valley recombination and coherence of  $\text{WSe}_2$ , where  $\Gamma_K$  ( $\Gamma_{K'}$ ) is recombination rate and  $\gamma_v$  is decoherence rate. Reproduced with permission.<sup>[154]</sup> Copyright 2016, Springer Nature. b) Schematic of the 2DCS experiment. Reproduced under the terms of the CC-BY 4.0 License.<sup>[156]</sup> Copyright 2018, The Authors, published by Springer Nature. c) Polarization resolved PL from the upper polariton branch, which is 3 times higher than that of bare excitons. Reproduced under the terms of the CC-BY 4.0 License.<sup>[42]</sup> Copyright 2016, The Authors, published by Springer Nature. d) Schematic of memory devices based on ferrovalley materials. Reproduced with permission.<sup>[158]</sup> Copyright 2015, Springer Nature. e,f) PL spectra of the  $X^0$  peak as a function of  $B$  and the splitting of  $X^0$  and  $X^-$  in  $\text{WSe}_2$ . Reproduced with permission.<sup>[159]</sup> Copyright 2015, Springer Nature. g) Energy level diagram of initial and final states of trion optical recombination. Reproduced under the terms of the CC-BY 4.0 License.<sup>[161]</sup> Copyright 2018, The Authors, published by Springer Nature. h) Valley splitting and normalized PL intensity as a function of  $B$ . Reproduced with permission.<sup>[43]</sup> Copyright 2017, The American Association for the Advancement of Science (AAAS).

2 to 4. Because of the special type-II band alignment, the  $\text{MoS}_2/\text{WS}_2$  system leads to highly n-doped  $\text{MoS}_2$  and enhanced many-body Coulomb interactions. Thus, the optical transitions of  $\text{MoS}_2$  deviate significantly from the simple noninteracting particle picture and elevate magnetic response. The magnetic dependent circularly polarized PL indicates the two  $X^0$  peaks located at  $\approx 1.94$  and  $2.08$  eV correspond to the exciton of  $\text{MoS}_2$  and  $\text{WS}_2$ , respectively. The valley splitting of  $\text{MoS}_2$  is larger than  $\text{WS}_2$ , from 0–7 T, for the Landé  $g$ -factor in  $\text{MoS}_2$  of  $\approx 11.03$  is two times of that in  $\text{WS}_2$  ( $\Delta E = g\mu_B B$ , where  $\Delta E$  is splitting energy). Moreover, the author verified the relationship between  $g$  factor and laser power, that is, the optical derived doping level mediates valley splitting. It was observed that the  $g$ -factor of  $\text{MoS}_2$  descended as the power increased, while the  $g$ -factor of  $\text{WS}_2$  is hardly governed. The results demonstrate that the optical pumping mediates the valley splitting in  $\text{MoS}_2$  through the doping process, while the strong spin-orbit coupling energy in  $\text{WS}_2$  impedes the tuning of valley degeneracy. Although TMDs provide a unique degenerate system to observe valley Zeeman splitting in both neutral and charged excitons, the values of  $\Delta E$  are always inconsistent among previous studies, which is affected by process of recoil of excess electron.

Recently, Tartakovskii's group simultaneously measured intervalley and intravalley trion photoluminescence, explored three distinct  $g$ -factors, where only one of them is associated with valley Zeeman effect.<sup>[161]</sup> First, the authors declared that there is singlet and triplet trions in  $\text{WSe}_2$  as considering the intra- and intervalley excitons. The two trions could be distinguished by fitting the circularly polarized PL spectra via Lorentzian functions. The authors conducted magneto-PL response of singlet and triplet trions in  $\text{WSe}_2$  and fitted them to observe the difference in splitting energy. The result (Figure 9g) shows that splitting energy of singlet trion is larger than that of triplet trions, and polarization of circular light also makes effect in energy shift that  $\sigma^-$  is more sensitive to  $B$  field. To analyze the peculiar behavior, the authors considered initial and final states of trion radiative recombination process under external magnetic field and found three different transition induced  $g$  factors. These 3  $g$  factors originate from trion valley Zeeman splitting, band  $c_1$  spin-valley splitting and trion  $\rightarrow$  electron Landau level energy, respectively. This work demonstrates that the splitting energy could not entirely reflect valley Zeeman effect in initial. It is necessary to measure and separate all the  $g$  factors associated with valley Zeeman effect and electron recoil processes.

Besides, valley DOF in the 2D materials can be controlled by the magnetic proximity effect, that is, ferromagnetic heterostructures. Xu et al. fabricated a ferromagnetic heterostructure composed of a monolayer WSe<sub>2</sub> and ultrathin ferromagnetic CrI<sub>3</sub> layers.<sup>[43]</sup> When the sample temperature is cooled down gradually below the  $T_C$  of CrI<sub>3</sub>, the valley splitting becomes visible based on the polarized photoluminescence spectra. At 5 K, the valley splitting of WSe<sub>2</sub> resulted from CrI<sub>3</sub> layers is estimated to be 3.5 meV, and the equivalent magnetic exchange field is estimated to be 13 T. Furthermore, they observed fast switching of valley splitting accompanied by the change of magnetization in CrI<sub>3</sub>. In addition to external magnetic field, the magnetization of CrI<sub>3</sub> can also be manipulated by light, which provides new opportunities to optical manipulation of valley (Figure 9h).

## 6. Ferroelectric Materials and FE-Gated Heterostructures

Ferroelectric materials are special functional materials with spontaneous and controllable electric polarization via external electric field. The fundamental landmark of ferroelectric materials is the polarization–electric field ( $P$ – $E$ ) hysteresis loop. The dependence of polarization on the electric field is linear at a weak external field, and transforms into nonlinear behavior with the increasing field. Physically, Landau-Ginzburg-Devonshire phenomenological model has been an essential method to solve the problem of ferroelectricity. In the 1940s, Ginzburg and Devonshire first developed Landau theory of phase transitions into ferroelectric materials. As demonstrated as

$$U = \alpha P^2 + \beta P^4 + \gamma P^6 - \vec{E} \cdot \vec{P} \quad (16)$$

$$E = 2\alpha P + 4\beta P^3 + 6\gamma P^5 + \rho \frac{dP}{dt} \quad (17)$$

where  $U$  is Gibbs free energy,  $E$  is external field,  $P$  is the polarization charge per unit area,  $t$  is thickness, and  $\alpha$ ,  $\beta$ ,  $\gamma$  are material parameters. As described in Landau-Ginzburg-Devonshire model, the relationship between Landau free energy  $U$  and the polarization  $P$  can describe ferroelectricity below the transition temperature ( $T_C$ ). The essential characteristic of ferroelectric materials is spontaneous polarization, which can be reversed by the external electric field, and the two stable spontaneous polarization states represent the two energy minima. The  $P$ – $E$  curve, as described in Equations (16) and (17), which is a consequence of the double well landscape, shows ferroelectric capacitance intuitively.

### 6.1. Ferroelectricity in 2D Materials

Ferroelectricity were experimentally discovered a century ago. Since then, many ferroelectric materials, such as BaTiO<sub>3</sub>, LiNbO<sub>3</sub>, PbTiO<sub>3</sub>, and P(VDF-TrFE), have been reported. So far, ferroelectric materials exhibit significance for application in field-effect transistor (FET), memory, and sensors devices. For these traditional epitaxy systems, ferroelectricity and its utilities are suppressed below a critical dimension by the strong

scaling effect. Generally, traditional perovskite ferroelectric materials lose their ferroelectricity when the thickness down to a critical value owing to incomplete screening of depolarization fields. Since the discovery of 2D ferroelectrics, 2D ferroelectric materials have attracted interest due to their simple synthesis method and intrinsic ultrathin behaviors, and they have emerged as promising candidates for overcoming issues existed in traditional ferroelectrics in terms of CMOS compatibility and thickness scaling. According to the ferroelectric polarization direction, ferroelectricity can be divided into in-plane polarization and out-of-plane polarization. In-plane ferroelectric switching is controlled by in-plane external electric field and results in in-plane dipole polarization field, while out-of-plane ferroelectric polarization switching is along the vertical direction of a 2D layer. Recently, ferroelectricity in 2D materials is studied for the clean interface as provided by vdW stacking. For instance, 2D ferroelectricity has been demonstrated in CIPS, WTe<sub>2</sub>, In<sub>2</sub>Se<sub>3</sub>, SnS, SnTe, Bi<sub>2</sub>O<sub>2</sub>Se, and 1T-MoTe<sub>2</sub>.<sup>[14,54,74,78,82,83,100,162–165]</sup> Notably, traditional ferroelectric materials are insulator, but researchers proved that 2D ferroelectric materials could be insulators, semiconductors, and metals, which endows them with wider applications in electronic and optoelectronic devices. In this section, the intrinsic ferroelectricity in 2D layered materials is summarized.

#### 6.1.1. 2D Ferroelectric Insulator

Recently, 2D ferroelectric FETs have attracted the interest of researchers. For traditional ferroelectric film/2D material structures, interface issue greatly degrades the performance (such as on–off ratio, memory window, and retention time) of device. By replacing traditional ferroelectric insulators with 2D ferroelectric insulators, vdW stacked 2D ferroelectric/2D semiconductor can eliminate the interface issue and get high-performance FE-FET. For instance, CIPS has been demonstrated the insulating behavior experimentally as a 2D ferroelectric insulator by Liu et al.<sup>[74]</sup> The out-of-plane ferroelectricity in CIPS stems from the displacement of Cu and In sublattice. An obvious phase contrast by PFM (Figure 10a), which indicates polarization switching, remains with a thickness down to 4 nm. The hysteresis loop of PFM phase and the butterfly loop of PFM amplitude demonstrate the robust ferroelectricity in CIPS ultrathin film. Moreover, SHG measurements explore the phase transition from ferroelectric to paraelectric at 320 K. CIPS, as a stable room temperature 2D ferroelectric material, acts as an ideal candidate for vdW heterostructured FE-FET. Furthermore, Balke et al. studied the ferroelectricity in CIPS and demonstrated their quadruple-well nature. Two distinct polarization phases result from the motion of Cu atoms into vdW gap were demonstrated, which double the information storage capacity.<sup>[167]</sup> The work provides great prospects of CIPS for next-generation multibit memory devices.

#### 6.1.2. 2D Ferroelectric Metal

Theoretically, itinerant electrons in metals would screen the external electric field so that ferroelectric switching is

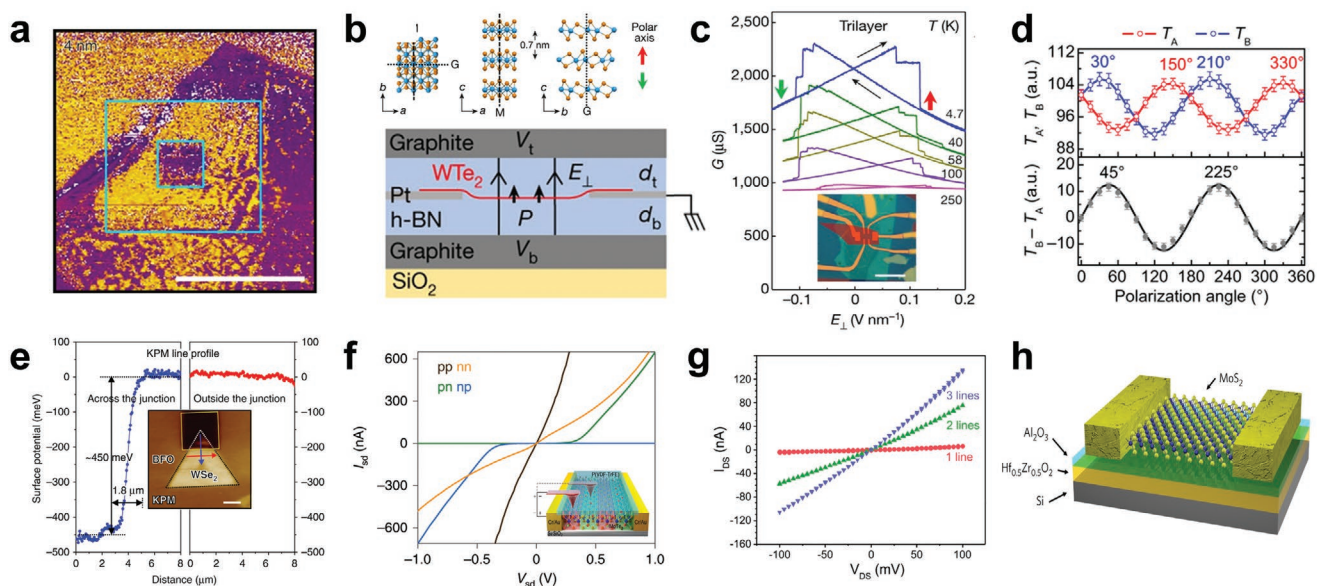


**Figure 10.** a) The PFM phase image of CIPS. Reproduced under the terms of the CC-BY 4.0 License.<sup>[74]</sup> Copyright 2016, The Authors, published by Springer Nature. b) Structure of WTe<sub>2</sub> and schematic cross-section of the device. c) Conductance *G* of WTe<sub>2</sub> as *E* is swept. Inset in d is the optical image of a double-gated device. b,c) Reproduced with permission.<sup>[54]</sup> Copyright 2018, Springer Nature. d) The light transmission of the In<sub>2</sub>Se<sub>3</sub> dependence on polarization angle. Reproduced under the terms of the CC-BY 4.0 License.<sup>[164]</sup> Copyright 2018, The Authors, published by American Association for the Advancement of Science. e) KPM and line profile image of WSe<sub>2</sub>/BFO device. Reproduced under the terms of the CC-BY 4.0 License.<sup>[166]</sup> Copyright 2018, The Authors, published by Springer Nature. f) Output curves of MoTe<sub>2</sub> homojunction. Reproduced with permission.<sup>[173]</sup> Copyright 2020, Springer Nature. g) Output curves of devices with different number of conductive paths. Reproduced with permission.<sup>[174]</sup> Copyright 2019, American Chemical Society. h) Schematic of a MoS<sub>2</sub> NCFET. Reproduced with permission.<sup>[175]</sup> Copyright 2018, Springer Nature.

prohibited in metals. But 2D metals is thin enough that external electric field could penetrate through the specimen to realize ferroelectric switching. Cobden et al. successfully demonstrated the spontaneous out-of-plane polarization and robust ferroelectric switching in bilayer or trilayer WTe<sub>2</sub>.<sup>[54]</sup> Monolayer WTe<sub>2</sub> is centrosymmetric and hence non-polar. The WTe<sub>2</sub> based devices exhibit bi-stable near zero electric field (Figure 10b,c) at temperature from 4 to 300 K. And the ferroelectricity switching could be intrinsically very fast. However, the origin of ferroelectricity in WTe<sub>2</sub> is still not clear. The electronic correlations theory is challenged. Lindenberg et al. demonstrated that few-layered WTe<sub>2</sub> based Berry curvature memory could originate from the interlayer vdW stacking transitions through the in situ Hall transport measurement.<sup>[168]</sup> And some theoretical calculations also support this mechanism.<sup>[169,170]</sup> The demonstration of ferroelectric polarization with 2D metals breaks the traditional inherent ferroelectric theory, and gives us a new direction of thinking about ferroelectric metal.

### 6.1.3. 2D Ferroelectric Semiconductor

Several 2D semiconductors have been demonstrated with ferroelectricity, which can be classified by the direction of the spontaneous polarization as in-plane ferroelectricity (e.g., SnTe, β-In<sub>2</sub>Se<sub>3</sub>, SnS), out-of-plane ferroelectricity (1T-MoTe<sub>2</sub>, Bi<sub>2</sub>O<sub>2</sub>Se) and intercorrelated in-plane and out-of-plane ferroelectricity (α-In<sub>2</sub>Se<sub>3</sub>). For 2D out-of-plane and intercorrelated ferroelectrics, ferroelectricity becomes poor or vanishes with the decreased thickness. In contrast, 2D in-plane ferroelectrics

remains robust against the reduced thickness for the vdW gaped and isolated polarization. For example, according to Li et al. work, SnTe demonstrates stable in-plane ferroelectricity at one unit cell limit with the ferroelectric transition temperature reaching 270 K.<sup>[14]</sup> Different from PFM, SHG etc. measurements, Li et al. used more sensitive measurement with STM and scanning tunneling spectroscopy (STS). They demonstrated ferroelectricity of SnTe with four evidence: the obvious stripe domain wall, atom displacement with lattice distortion, band bending resulted the spontaneous polarization (Figure 10d), and polarization switching by electric field. The *T<sub>C</sub>* of the SnTe films was found to be increased with enhancing from the thickness from 1 unit cell to 4 unit cell, which maybe origin from low free carrier density. And the in-plane ferroelectricity is associated with the screening effect of free carrier on the dipole–dipole interaction.

Except SnTe, SnS and β-In<sub>2</sub>Se<sub>3</sub> have also been reported with in-plane ferroelectricity. Fuhrer et al. demonstrated that β-In<sub>2</sub>Se<sub>3</sub> exhibits room temperature in-plane ferroelectricity via PFM, STM, polarized light microscopy, and low-energy electron microscopy (LEEM).<sup>[164]</sup> Their work shows obvious polarization angle dependence on the light transmission of adjacent domains, and in-plane ferroelectricity induced strong linear dichroism. The ferroelectric polarization strongly depends on superlattice distortion along the threefold symmetric directions in the *c* plane. Stable ferroelectricity under temperature to 200 °C are demonstrated in both exfoliated thin layers and bulk β-In<sub>2</sub>Se<sub>3</sub>. Bao et al. reported stable in-plane ferroelectricity in few layered SnS with a large gate tunable polarization with *I*–*V*, *P*–*V* hysteresis curves and SHG results. The result indicates that ferroelectric transition exists from 4 to 298 K. Because of

a converse piezoelectric effect in the armchair direction, the in-plane polarization of SnS shows nanoripples-like image through STM method, which is also regarded as the coupling effect between the lattice strain and the ferroelectric order.

$\text{Bi}_2\text{O}_2\text{Se}$  is an emerging 2D semiconductor with high carrier mobility, tunable bandgap, and low effective mass and has attracted many researchers' attention. Biswas et al. demonstrated ultrathin  $\text{Bi}_2\text{O}_2\text{Se}$  nanoflakes possess robust out-of-plane ferroelectricity due to the broken inversion symmetry induced by orthorhombic distortion at room temperature.<sup>[165]</sup> The distortion is associated with the displacement of O and Bi atoms, which breaks local inversion symmetry and relates to the formation of spontaneous dipole movement. Recently, Yuan et al. found that monolayer  $1\text{T-MoTe}_2$  exhibits room temperature out-of-plane ferroelectricity,<sup>[100]</sup> which results from the broken symmetry induced by the atomic displacements. In addition, the  $T_C$  is demonstrated to be above 330 K and an on-off ratio of about 1000 is achieved for the FTJ device.

For the in-plane ferroelectricity and out-of-plane ferroelectricity, the spontaneous polarization occurs only along one direction. In contrast, intercorrelated ferroelectricity exhibits the rotation of the out-of-plane (in-plane) polarization due to the reversal of in-plane (out-of-plane) polarization under a vertical electric field. Robust intercorrelated ferroelectricity in  $\alpha\text{-In}_2\text{Se}_3$  has been found by Li et al.<sup>[83]</sup> They observed that in-plane polarization changes simultaneously when switching the out-of-plane phase. The behavior was inferred to the lateral motion of the center of Se atomic layer by the introduction of external electric field. Zhang et al. demonstrated similar results, where the intrinsic 2D  $\alpha\text{-In}_2\text{Se}_3$  ferroelectricity with dipole locking and ultrahigh transition temperature (700 K) were demonstrated. The SHG and PFM measurements indicate the out-of-plane polarization requires a flip of polarization from the reversed in-plane lattice orientation.<sup>[171,172]</sup> The locked polarization behavior provides new techniques on stabilizing the 2D ferroelectricity, which is of great importance for studying 2D multiferroics and robust room temperature ferroelectrics.

## 6.2. FE Modulated DOFs: Novel Devices Based on Dipole Electric Field and FE Heterostructures

Driven by the ultrahigh polarized field, novel devices modulating the DOFs are proposed. In this section, we focus on the recent developed FE modulation process and related devices, including logic transistors, memories, and light sensors.

### 6.2.1. Logic Transistors

Logic switch transistors are the footstone for integrated circuit. Nowadays, many investigators contribute to explore novel logic devices, and ferroelectric devices are promising candidates due to their rich tunability.

*Programmable Ferroelectric Devices:* With the development of PFM technology, a ferroelectric film could be regulated into nanodomains with different polarization directions and applied for laterally 2D electronic and optoelectronic devices. Notably, programmable ferroelectric devices are capable to achieve

nonvolatile transistors on monolayer 2D materials. Wu et al. obtain a lateral  $\text{WSe}_2$  p-n homojunction by manipulating the polarization of  $\text{BiFeO}_3$ .<sup>[166]</sup> Monolayer  $\text{WSe}_2$  exhibits different surface potential and carrier density on the adjacent region with opposite polarization directions of  $\text{BiFeO}_3$ . An obvious current rectifying behavior in the nonvolatile p-n homojunction was observed, which indicates the excellent gate manipulation of programmable  $\text{BiFeO}_3$  film (Figure 10e). This work provides an idea in nonvolatile control of carrier and ferroelectric doping of single 2D materials, thus opening a door to develop laterally 2D electronic and optoelectronic devices. Apart from inorganic ferroelectric materials, ferroelectric polymers could also be utilized for programmable ferroelectric devices due to the efficiently eliminated interface issues. Wang et al. reported robust and nonvolatile  $\text{MoTe}_2$  lateral n-n, n-p, p-n, and p-p homojunctions by tuning the polarity of ferroelectric polymer P(VDF-TrFE) (Figure 10f).<sup>[173]</sup> The p-n and n-p homojunctions demonstrate outstanding rectification properties with rectification ratio of  $10^3$  and ideality factor  $n$  of 2.5. Different from most of inorganic ferroelectrics, ferroelectric domains of P(VDF-TrFE) are reversible, durable and nonvolatile, which result in high on-off ratio, fast refresh time of electronic devices. Gruverman et al. fabricated a programmable device based on both ferroelectric field effect transistor and ferroelectric tunnel junction.<sup>[174]</sup> They applied SPM to fundamental  $\text{MoS}_2/\text{Pb}(\text{Zr,Ti})\text{O}_3$  (PZT) FET structure. Using SPM, the polarization states of PZT was changed with creating nanodomain paths, and thus the channel conductivity of  $\text{MoS}_2$  can be controlled (Figure 10g). Moreover, the number and the shape of nanodomain paths can tune the channel conductivity. The experiment paves the way of energy-efficient synaptic memory devices.

*Steep Slope Logic Switch FET:* The thermionic limit of FET, named Boltzmann tyranny, prevents the lowering of the overall power consumption in integrated circuits. In 2008, Salahuddin proposed the concept of negative capacitance FET (NCFET) with ferroelectrics/dielectrics/semiconductor structure. In the recent years, NCFET based on 2D channel materials or 2D ferroelectric gate materials have been reported. For example, Ye and colleagues fabricated steep-slope hysteresis-free negative capacitance  $\text{MoS}_2$  transistors. The  $\text{MoS}_2/\text{Al}_2\text{O}_3/\text{HZO}$  structure exhibits the minimum subthreshold swing (SS) of  $5.6 \text{ mV dec}^{-1}$ , hysteresis of 12 mV (Figure 10h),<sup>[175]</sup> and a maximum drain current of  $510 \mu\text{A } \mu\text{m}^{-1}$ , which is a promising candidate for future low power logic switch FET. Then, p-type  $\text{WSe}_2/\text{HfO}_2/\text{Ni}/\text{Al}_2\text{O}_3$  NCFET was also demonstrated with the SS less than  $60 \text{ mV dec}^{-1}$ .<sup>[176]</sup> Due to the unique properties of 2D materials in specific interface and contact, the most suitable integrated device is vdW integration without any dangling bond. vdW NC transistors based on 2D CIPS and 2D  $\text{MoS}_2$  were successfully demonstrated by Liu et al.<sup>[177]</sup> The device shows excellent performance with the minimum SS of  $28 \text{ mV dec}^{-1}$ . In addition, the vdW NC logic inverter with the voltage gain of 24 and high-performance logic switch FET were also realized based on the 2D vdW structure.

### 6.2.2. Memory

Ferroelectric FET, random access memory (RAM) and tunnel junction have long been studied for nonvolatile memory

devices. Herein, we introduce the recent progress of these aspects.

**Ferroelectric FET:** Several researches based on ferroelectric insulator gate/2D semiconductor channel structure open the door of 2D ferroelectric FET memory devices. Specifically, gate utilizes ferroelectric insulators and tunes the conductivity of semiconductor channels. The two polarization states of ferroelectric gate manipulate channel conductivity and induce two resistivity states, corresponding to the “0” and “1” in a memory device. Compared with other type memory devices (such as resistive memory, floating memory), ferroelectric FET possesses longer nonvolatile, stronger stability and nondestructive properties. Suh et al. demonstrated a graphene-hBN-Pb(Mg<sub>1/3</sub>Nb<sub>2/3</sub>)<sub>0.71</sub>Ti<sub>0.29</sub>O<sub>3</sub> (PMN-PT) structured memory device based on ferroelectric polarization switching and charge trapping,<sup>[178]</sup> but on/off ratio of the memory is less than one magnitude. Using MoS<sub>2</sub>/PZT structure, larger memory window, nondestructive operation and optoelectronic tunability have been achieved by Sinitskii et al.<sup>[179]</sup> But its memory time is short (10 000 s) and on/off ratio is small (about 22). Lee et al. fabricated a BP-P(VDF-TrFE) nonvolatile memory device with on/off ratio of 10<sup>5</sup> while short retention time of 10<sup>3</sup> s.<sup>[180]</sup> Further, a long retention time >10 d based on n- and p-type 2D materials-PZT structure has been demonstrated by Wu et al. During this experiment, the depolarization field was impaired through stronger polarization field and cleaner interface for such long retention time. In contrast with P(VDF-TrFE) and PZT, Im et al. obtained lead-free inorganic Ba<sub>x</sub>Sr<sub>1-x</sub>TiO<sub>3</sub>(BST) oxides,<sup>[181]</sup> and the MoS<sub>2</sub>-BST devices show on/off ratio of 10<sup>4</sup> and retention time of 10<sup>3</sup> s.

Recently, the optical introduced and stress mediated ferroelectric polarization provide new routines. Alexe et al. proved that

WS<sub>2</sub>/PZT device has light and voltage simultaneously tuned memristive property,<sup>[182]</sup> which can be used for neuromorphic applications. Wu et al. demonstrated a ferroelectric strain FET memory device based on MoTe<sub>2</sub>/PMN-PT structure.<sup>[183]</sup> The strain induced by electric field on PMN-PT causes semiconductor-semimetal phase change in MoTe<sub>2</sub> (Figure 11a,b). The strain FET breaks the limitations of slow switch time, volatile, and SS issues and obtains a high on/off ratio (10<sup>7</sup>) as well as a fast switch time.

More and more novel 2D/ferroelectrics memory devices have been demonstrated. Researchers are no longer satisfied to the traditional stack structures and electrical manipulations, instead, more innovative structures, tuning methods and new mechanism are promoted and demonstrated. Bulk ferroelectric films have inevitable dangling bonds resulting in interface issues, which were settled through all vdW structures. Ye and colleagues fabricated MoS<sub>2</sub>/CIPS vdW heterostructure ferroelectric FET memory device with enhanced on-off ratio.<sup>[75]</sup> The 2D vdWs FE-FET shows an intrinsic counterclockwise hysteresis loop and nonvolatile memory characteristics controlled by the dual gate.

Utilizing the recent developed ferroelectric semiconductors, the coexistence of polarization and gate-tunability provide a rising platform for memory FETs. Recently, Ye and colleagues proposed a ferroelectric semiconductor FET and demonstrated improved memory performance for the vanished depolarization field.<sup>[20]</sup> The on/off ratio and maximum current reaches over 10<sup>8</sup> and 862 μA μm<sup>-1</sup>, respectively. They also found counterclockwise and clockwise hysteresis loop when utilizing different dielectric materials due to complicated interaction between semiconducting and ferroelectrics in α-In<sub>2</sub>Se<sub>3</sub> (Figure 11c,d).

**Ferroelectric RAM and Tunneling Junction:** Traditional ferroelectric RAM utilizes ferroelectric film as a capacitor between

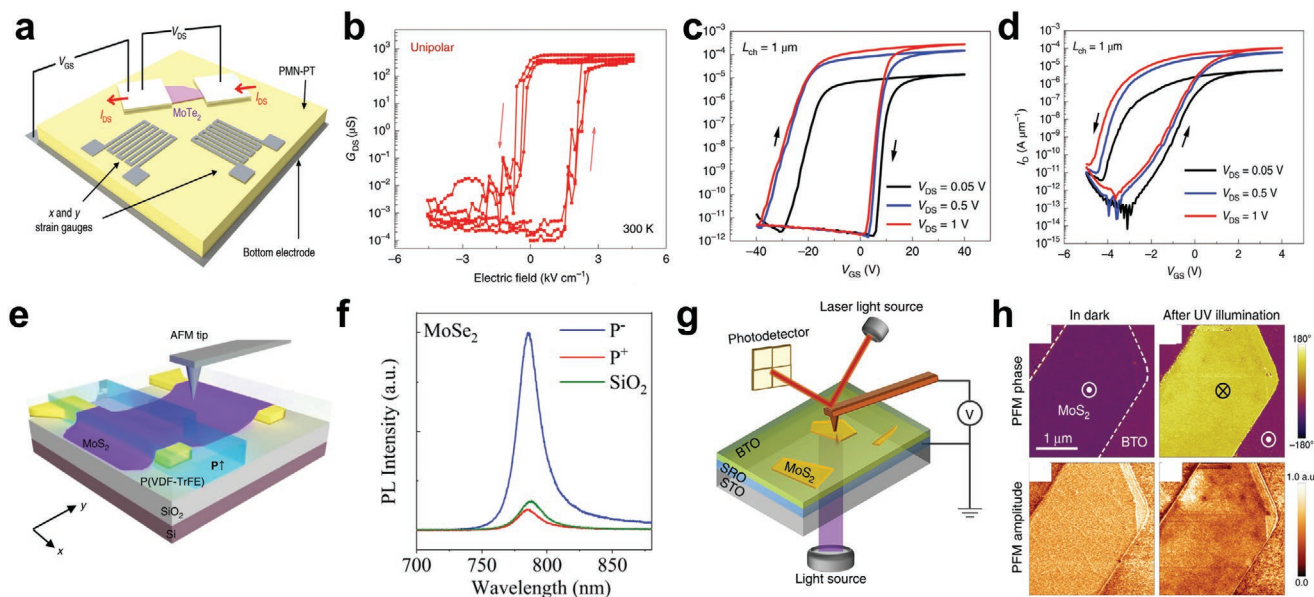


**Figure 11.** a) Schematic of the MoS<sub>2</sub> strain FET. b) Conductance  $G$  of the MoS<sub>2</sub> strain FET as  $E$  is swept. a,b) Reproduced with permission.<sup>[183]</sup> Copyright 2019, Springer Nature. c,d) Output curves of FeS-FET devices. Reproduced with permission.<sup>[20]</sup> Copyright 2019, Springer Nature. e) Configuration of a ferroelectric PVDF-coupled MoS<sub>2</sub> device. Reproduced under the terms of the CC-BY 4.0 License.<sup>[191]</sup> Copyright 2020, The Authors, published by Springer Nature. f) PL spectra of MoSe<sub>2</sub> monolayer. Reproduced with permission.<sup>[194]</sup> Copyright 2018, American Chemical Society. g) Schematic of device geometry for ferroelectric heterostructures. h) PFM phase in the dark before and after UV illumination. Reproduced under the terms of the CC-BY 4.0 License.<sup>[195]</sup> Copyright 2018, The Authors, published by Springer Nature.

top and back electrodes. When applying up and down electric field, ferroelectric capacitor shows two robust polarization states which are nonvolatile memristive phenomena. Recently, Poh et al., Zeng et al., and Zhang et al. independently demonstrated the  $\alpha$ - $\text{In}_2\text{Se}_3$  based ferroelectric RAM.<sup>[172,186–188]</sup> These works show that both monolayer and multilayer  $\alpha$ - $\text{In}_2\text{Se}_3$  exhibit on/off ratio. Notably, Poh et al. achieved a high-quality  $\alpha$ - $\text{In}_2\text{Se}_3$  film by MBE growth method, leading to enhanced on/off ratio of  $10^6$ .<sup>[186]</sup> Zeng et al. obtained retention time over  $10^3$  s and lifetime over  $10^5$  cycle without losing nonvolatility modulated by dual gate.<sup>[187]</sup> Considering the great potential of FeRAM for next generation memory device, and high mobility and intrinsic vdW interface of 2D ferroelectrics, 2D FeRAM shows great potential to possess fast switch time, high on-off ratio and long retention time.

Ferroelectric tunneling junction (FTJ) structure is similar to ferroelectric RAM with a two-terminal vertical heterostructure. While FTJ focuses on modulating the barrier height of the two contact interfaces and generates multiple resistance states. Traditional FTJ is fabricated by using ABO-type perovskites and binary oxides. But it is still a challenge to obtain a high tunneling resistance (TER) due to the difficulty in achieving ultraclean interfaces while maintaining the tunability of contacts simultaneously. Recently, Wang et al. experimentally demonstrated 2D FTJ for the first time by using CIPS.<sup>[188]</sup> The authors utilized graphene and Cr as the asymmetric electrodes and achieved a high TER above  $10^7$ , which is attributed to the large barrier height mismatch, that is, the modulated Fermi level of graphene by ferroelectric polarization of CIPS.

### 6.2.3. Light Sensors

Utilizing ferroelectric materials as gate dielectrics, the intrinsic properties (such as carrier density and bandgap) of channels could be modulated. These phenomena make ferroelectrics wonderful for optoelectronic devices, especially photodetectors.  $\text{MoS}_2$  is one of the most popular optoelectronic objects among the family of 2D materials because of its high mobility and thickness dependent bandgaps. To improve the performance of  $\text{MoS}_2$  phototransistors, Wang et al. revealed a strong interface electric field induced by ferroelectric polymer P(VDF-TrFE),<sup>[190]</sup> which reduce the dark current of  $\text{MoS}_2$  channel, thus improve the photoresponsivity to  $2570 \text{ A W}^{-1}$  ( $\lambda = 635 \text{ nm}$ ) and broaden the response wavelength to  $1550 \text{ nm}$ . Recently, by combining photogating effect induced by ferroelectric polarization field and voltage amplification effect into the HZO/ $\text{MoS}_2$  phototransistor,<sup>[191]</sup> ultrahigh photodetectivity of  $4.75 \times 10^{14} \text{ cm Hz}^{1/2} \text{ W}^{-1}$  ( $\lambda = 637 \text{ nm}$ ) and SS of  $1764 \text{ mV dec}^{-1}$  can be realized.

Ferroelectric programmable devices mentioned above could also be applied to photodetectors. Zhai et al.<sup>[192]</sup> and Wang et al.<sup>[193]</sup> demonstrated P(VDF-TrFE)/ $\text{MoS}_2$  and P(VDF-TrFE)/ $\text{MoTe}_2$  programmable homojunction photodetectors, respectively (Figure 11e). They both achieved similar performance with responsibility of  $\approx 101 \text{ A W}^{-1}$ , detectivity of  $10^{13}$  Jones and response time  $\approx 101 \mu\text{s}$ . These works open a new effective method to construct p–n homojunction in individual 2D atomic layer, which offers inspiration for the CMOS integrated device.

Ferroelectric materials can also manipulate the photoluminescence (PL) response of 2D materials. Lu et al. dem-

onstrated that domain-engineered  $\text{LiNbO}_3$  with up- and down-polarization can efficiently modulate the PL emission of 2D materials.<sup>[194]</sup> They found  $9 \times$  PL enhancement under different domain polarization orientation (Figure 11f). Notably, light can control ferroelectric functions of ferroelectric materials. Gruverman et al. demonstrated ferroelectric polarization switching in  $\text{BaTiO}_3(\text{BTO})/\text{MoS}_2$  structure can be realized using light instead of electric field due to the generated charges at the BTO/ $\text{MoS}_2$  interface, which result from the light induced change of the exciton states in  $\text{MoS}_2$  (Figure 11g,h).<sup>[195,196]</sup>

### 6.3. Developing Novel 2D Ferroelectrics

The traditional ferroelectrics face critical thickness limited issues and achieving ferroelectric thin film is always a huge challenge. So 2D ferroelectrics provide a promising solution. Combined with the first principle theory, novel ferroelectrics with vdW structure are under prediction. In this section, we focus on the theoretical predicted novel 2D ferroelectrics.

Elemental 2D layered materials (such as black phosphorus, tellurene, bismuthine) are outstanding family in 2D materials due to their wide range tunable bandgap and high mobility. A few kinds of elemental 2D ferroelectric materials (Te, As, Sb, and Bi) have been predicted. Ji et al. predicted multilayer Te exhibits polarization due to spontaneously broken structure symmetry by the in-plane ion displacement.<sup>[197]</sup> The predicted transition temperature is above  $600 \text{ K}$ , and it shows electric polarization tuned and valley dependent spin textures. Additionally, Zhang et al. forecasted group-V (Bi, Sb, and As) monolayers with spontaneous in-plane ferroelectric polarization at room temperature.<sup>[198]</sup> Lattice distortion with atomic layer buckling, which is induced by s–p hybridization, contributes to the ferroelectric spontaneous polarization. Their theoretical result reveals the effect of s–p hybridization on distortion of 2D system with the puckered lattice structure like phosphorene.

For binary compounds, Shirodkar and Waghmare suggested that monolayer 1T- $\text{MoS}_2$  possess ferroelectricity.<sup>[199]</sup> Compared with 2H- $\text{MoS}_2$ , 1T- $\text{MoS}_2$  opens a small bandgap from the degeneracy of Fermi surface and electron–phonon coupling, which causes a metal–semiconductor transition. The structural distortion predominantly caused by the in-plane Mo displacements results in the broken symmetry (Figure 12a). Similar to 1T- $\text{MoS}_2$ , Picozzi inferred that monolayer t- $\text{MX}_2$  ( $M = \text{Mo}, \text{W}$ ;  $X = \text{S}, \text{Se}, \text{Te}$ ) with  $d^2$  metal ions could be promising candidates for ferroelectric materials for their spontaneous dielectric polarization (Figure 12b) and spin–orbit coupling.<sup>[200]</sup>

In addition to elemental and binary compounds mentioned above, multicomponents are also highly anticipated. Yang et al. predicted CIPSe has a AFE/FE transition under the open-circuit boundary condition ( $D = 0$ ),<sup>[201]</sup> and always show ferroelectricity under close-circuit boundary condition ( $E = 0$ ) (Figure 12c,d). Liu et al. showed that monolayer  $\text{AgBiP}_2\text{Se}_6$  exhibits out-of-plane polarization which results from compensated ferroelectric state.<sup>[202]</sup> The compensated ferroelectric state originates from the distorted  $\text{Ag}^+$  and  $\text{Bi}^{3+}$  sublattices and exhibits two stable ferroelectric phases. Recently, Li et al. demonstrated theoretically that niobium oxide dihalides  $\text{NbOX}_2$  ( $X = \text{Cl}, \text{Br}, \text{and I}$ ) show intrinsic room temperature in-plane ferroelectricity and

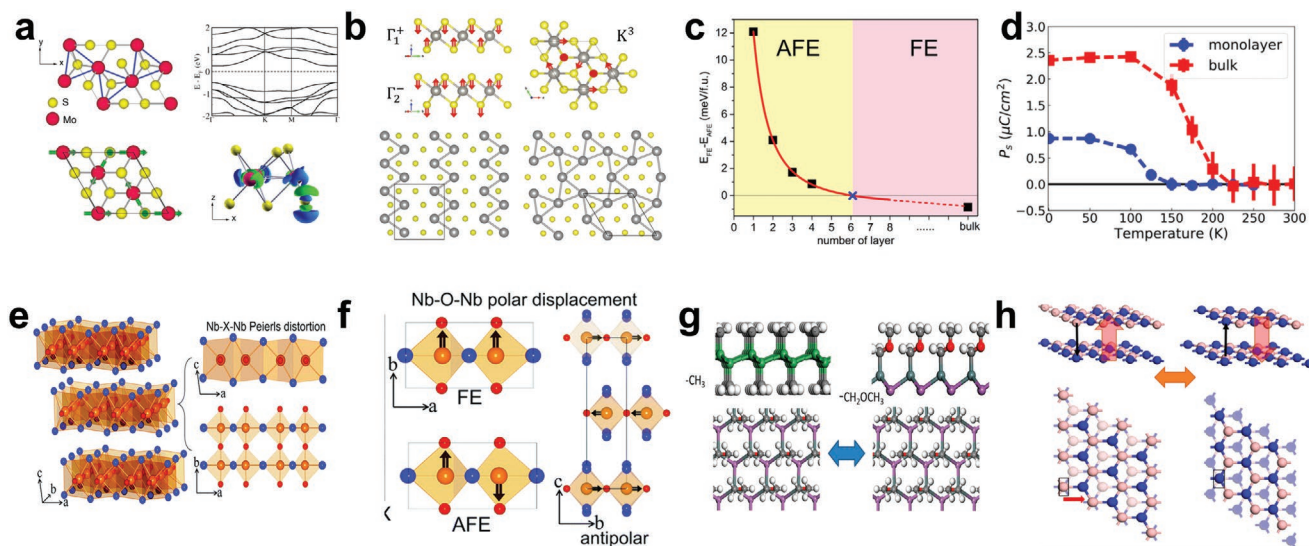


**Figure 12.** a) Structure, band structure and comparison of dIT with cIT MoS<sub>2</sub>. Reproduced with permission.<sup>[199]</sup> Copyright 2014, American Physical Society. b) Crystal structure of MX<sub>2</sub> phase. Reproduced with permission.<sup>[205]</sup> Copyright 2016, American Physical Society. c) Layer-dependent of the energy different of CIPS. d) Zero-*E*-field spontaneous polarization dependence on temperature in monolayer and bulk CulnP<sub>2</sub>Se<sub>6</sub>. c,d) Reproduced with permission.<sup>[201]</sup> Copyright 2017, American Physical Society. e) Crystal structure for PE of bulk NbOX<sub>2</sub>. f) Calculated phonon spectrum for bulk PE NbOI<sub>2</sub>. e,f) Reproduced with permission.<sup>[203]</sup> Copyright 2019, Royal Society of Chemistry. g) Crystal structure of methyl-terminated germanene/stanene and Sn(P, As, Sb)-CH<sub>2</sub>OCH<sub>3</sub>. Reproduced with permission.<sup>[204]</sup> Copyright 2016, American Chemical Society. h) Ferroelectric switching pathway of BN bilayer. Reproduced with permission.<sup>[207]</sup> Copyright 2017, Springer Nature.

antiferroelectricity induced by Nb cations polar displacement (Figure 12e,f).<sup>[203]</sup>

Besides, many functionalized 2D systems also theoretically exhibit ferroelectricity. Wu et al. predicted that 2D monolayer materials, including silicene, germanene, stanene, and MoS<sub>2</sub>,<sup>[204]</sup> could be covalently modified by ligands to realize ferroelectricity with high mobility and modest bandgap concurrently. The functionalized material systems modified by ligands with a dipole result in the electric switchable polarization (Figure 12g). The interface free carriers can be tuned between holes and electrons when switching the polarization. The simulation indicates that the covalent functionalized material system is a promising candidate for many future ferroelectric devices (FE-FET, topological transistor and FTJ). Picozzi et al. theoretically predicted the ferroelectricity in several 2D buckled honeycomb group IV and group III-V binary monolayers,<sup>[205,206]</sup> in which the ferroelectric dipoles are induced by the lattice buckled structure. Besides, the binary system also shows novel valley-related properties and Rashba spin physics, and the Rashba spin is fully controlled by ferroelectric polarization switching, while valley-dependent properties originates from binary nature. Moreover, Wu et al. inferred that graphitic bilayer of 2D materials (such as BN, AlN, ZnO, MoS<sub>2</sub>, and GaSe) show vertical ferroelectricity resulted from the strong charge transfer from the upper layer to the down layer due to the close interlayer distance (Figure 12h).<sup>[88,207]</sup>

On the basis of the various calculations (such as DFT, first-principles), many researchers demonstrated theoretically a series of 2D ferroelectrics. Some of these have been synthesized experimentally, which possess tunable bandgap and high mobility for nanoelectronic and optoelectronic devices. With the rising number of discoveries of 2D ferroelectrics, emerging

and integrated electronics and optoelectronics are expected, which will open a new area.

## 7. Summary and Perspective

In conclusion, we have summarized the state-of-the-art research situations of polarized materials and heterostructures. We have discussed the ferromagnetic, ferrovalley, and ferroelectric materials in detail. Represented by CrX<sub>3</sub>, TMDs, and SnX, the polarized family is now rather complicated on their elements system. Focusing on the basic physical mechanisms and synthesis process, some of these materials have been studied for years and revealed some satisfying performances. However, as depicted in **Table 2**, aiming at their practical application, some key issues should be addressed.

The first challenge is the robustness of polarization at the 2D limit. Especially for ferromagnets, compared with the bulk state, the polarization transition temperature is generally reduced in 2D situation. It is of great importance on revealing air stable, room temperature magnetic semiconductors and related spintronic devices robust against thermal fluctuation. It has been suggested that the doped and alloyed TMDs would be fascinating systems for studying the 2D magnetism, more systematic studies are necessary in this respect. The researchers should be specially informed that beyond the three polarized materials discussed, 2D antiferromagnetic and multiferroic materials could also possess fascinating polarization behaviors. The antiferromagnetic orders have been revealed in MnPS<sub>3</sub> and NiPS<sub>3</sub> systems, while the 2D multiferroics have been predicted in SnS and SnSe with coupled spontaneous ferroelectric and ferroelastic polarization behaviors.<sup>[208–210]</sup> The antiferromagnetic

**Table 2.** Schematic visualization of the technology urgently demanded for 2D polarized electronics.

Synthesis materials	<ul style="list-style-type: none"> <li>• Direct growth</li> <li>• Ferromagnetism</li> <li>• CrI<sub>3</sub> Fe<sub>3</sub>GeTe<sub>2</sub></li> <li>• Low air stability</li> </ul>	Ferrovalley <ul style="list-style-type: none"> <li>• VSe<sub>2</sub></li> <li>• No experimental demonstration</li> </ul>	Ferroelectricity <ul style="list-style-type: none"> <li>• CuInP<sub>2</sub>S<sub>6</sub></li> <li>• Low air stability</li> <li>• CuInP<sub>2</sub>S<sub>6</sub> In<sub>2</sub>Se<sub>3</sub></li> <li>• High leak current</li> </ul>
Construct heterostructures	<ul style="list-style-type: none"> <li>• Modification of TMDs</li> <li>• Doping, alloying, and decoration</li> <li>• Lack of phase diagram and experimental regularities</li> </ul>		<ul style="list-style-type: none"> <li>• Develop fully automatic transfer techniques</li> </ul>
Design devices	<ul style="list-style-type: none"> <li>• Transfer</li> <li>• Wet transfer</li> <li>• Organic solvents free techniques</li> <li>• Dry transfer</li> <li>• Interface</li> <li>• Encapsulation</li> <li>• Large-area hBN</li> <li>• Charged impurities induced degradation</li> </ul>		<ul style="list-style-type: none"> <li>• Contact issue</li> <li>• High efficiency charge-spin, charge-valley conversion</li> </ul>
	<ul style="list-style-type: none"> <li>• Device simulation</li> <li>• Equation describing the density of DOFs</li> <li>• Effective SPICE models</li> </ul>		

At its current stage, the 2D polarized electronics is more confined to the laboratory demonstration. A full integration process to the monolithic silicon circuits is absent, which are favored for the optimized manufacture chains. The reliability and yield of 2D polarized electronics is limited during the laboratory demonstration and hinders the integration. Thus, we listed the key topics and challenges for future works.

orders are utilized due to the spin-orbital torque behavior, which is of great value for spintronic memory devices. For 2D multiferroics, the coupled DOFs could provide researchers with more routines modulating the DOFs.

The second important area is the lack of efficient synthesis routine for 2D polarized system. On synthesizing the chromium halides, it is of great difficulty due to the lack of solid-state sources and air stability. Further, different from the traditional TMDs, the element components of polarized materials could be more complicated, such as Fe<sub>2</sub>GeTe<sub>3</sub> and CuInP<sub>2</sub>S<sub>6</sub>, thus the CVD method may not be compatible. It is suggested to modify the traditional methods and introduce more techniques such as solution method and pulse laser deposition on fabricating polarized materials in a large scale.<sup>[211–214]</sup>

Nonlayered materials could be a virgin land on studying 2D polarization. These materials could be fascinating with robust polarization, high transition temperatures, and coupled DOFs. Although hard to be exfoliated, the vdW epitaxy technique promotes the development of 2D nonlayered materials and have been demonstrated in 2D GaN, Ga, and CdTe.<sup>[215–218]</sup> With simplified element component, 2D Cr<sub>2</sub>S<sub>3</sub>, CrSe, and MnSe have been developed.<sup>[127,133,219]</sup> By trading-off the thickness and satisfying performance, it is challenging on balance the dangling-bonds and polarization behavior. However, the introduction of non-layered materials would provide researchers with more options.

Further, the ultrathin nature endows 2D materials with unique properties, such as linear electron dispersion in graphene, direct band-gap in TMDs, and SOCs originates from the atoms. These unique behaviors are also sensitive to the external fields at the 2D limit.<sup>[220]</sup> By introducing external modifications, such as 0D magnetic quantum dots, 1D nanotubes and

nanoribbons, more fascinating optical and electronic characters are expected. Although these techniques have demonstrated efficiency in traditional semiconductor devices, we should still consider the difference introduced by the reduced dimensionality, that is, the microphysical process such as the electronic structures, the scattering and drift process, these issues are required to be solved urgently. The intralayer coupling is frustrating. For instance, the antiferromagnetic behavior is observed in bilayer CrI<sub>3</sub>, while it has long been believed to be ferromagnetic coupled in bulk CrI<sub>3</sub> crystals. The valley behavior greatly depends on the rotation angle between layers. And the charge screening effect at the interface is significant for ferroelectric heterostructures. The DOFs behaviors is confusing at the interface and a clear picture is still absent.<sup>[221]</sup> During the fabrication of devices, the interface should be carefully treated to avoid localized defect states, which result in the unanticipated carrier redistribution and band structure reconstruction. To address these questions, the fabrication techniques such as exfoliation/transfer process in vacuum of inert gas atmosphere have been developed to obtain clean interfaces. For the contact quality, vdW contact and edge contact have demonstrated their efficiency on reducing the contact defects and charge-spin conversion.<sup>[222]</sup> The detection techniques with high sensitivity to the symmetry factors such as SHGs and MOKEs have also been elevated to in situ trace the DOFs interaction.

Meanwhile, there still exists great technical obstacles on the commercial applications of polarized electronics. For spintronics, the all-electrical spin-generation and manipulation are still urgently demanded. For valleytronics, the combination of 2D materials into silicon-based optoelectronic integration is an attractive territory. And for polarized electronics, better devices with compatibility to manufacturing process, lower power

assumption, and higher linearity have long been pursued. By designing heterostructures based on the pristine or interface effects, and utilizing the coupled DOFs lie behind, multifunctional devices invented would provide promising prospects. There have been 2D materials combined with traditional semiconductors and meta-structures demonstrating functional electronic and optical devices, which would be a potential routine to these obstacles.<sup>[223]</sup>

Finally, on designing 2D polarized materials and devices, it would be of great help if the calculation process could be introduced. Compared with the design of semiconductor devices based on Poisson's equation, continuity equation, and carrier transport equations, the design of multifunctional polarized devices is still immature. Further theoretical works on the density of polarized DOFs, boundary conditions, and equilibrium potential in the channels would be instructive. Considering the great potential of 2D polarization for next generation electronics, it is much more complicated in the designing process due to the mixed DOFs coupling, and thus emergent to utilize more computer process.

## Acknowledgements

J.C., Y.W., and X.W. contributed equally to this work. The authors gratefully acknowledge the support from the National Natural Science Foundation of China (21603157, 51722204, 51972041, and 51972042), the National Key Basic Research Program of China (2014CB931702), the National Basic Research Program of China (2015CB358600), the Sichuan Science and Technology Project (2016RZ0033, 2018RZ0082), the Fundamental Research Fund for the Central Universities (ZYGX2016Z004 and ZYGX2018J036), and the Natural Science Foundation of Guangdong Province (2018A030310225).

## Conflict of Interest

The authors declare no conflict of interest.

## Keywords

2D polarized materials, ferroelectric materials, ferromagnetic materials

Received: July 1, 2020

Revised: July 21, 2020

Published online:

- [1] R. Jansen, *Nat. Mater.* **2012**, *11*, 400.
- [2] A. I. Khan, K. Chatterjee, B. Wang, S. Drapcho, L. You, C. Serrao, S. R. Bakaul, R. Ramesh, S. Salahuddin, *Nat. Mater.* **2015**, *14*, 182.
- [3] J. Torrejon, M. Riou, F. A. Araujo, S. Tsunegi, G. Khalsa, D. Querlioz, P. Bortolotti, V. Cros, K. Yakushiji, A. Fukushima, H. Kubota, S. Yuasa, M. D. Stiles, J. Grollier, *Nature* **2017**, *547*, 428.
- [4] A. Chen, Y. Wen, B. Fang, Y. Zhao, Q. Zhang, Y. Chang, P. Li, H. Wu, H. Huang, Y. Lu, Z. Zeng, J. Cai, X. Han, T. Wu, X. X. Zhang, Y. Zhao, *Nat. Commun.* **2019**, *10*, 243.
- [5] A. K. Yadav, K. X. Nguyen, Z. Hong, P. García-Fernández, P. Aguado-Puente, C. T. Nelson, S. Das, B. Prasad, D. Kwon, S. Cheema, A. I. Khan, C. Hu, J. Iñiguez, J. Junquera, L. Q. Chen, D. A. Muller, R. Ramesh, S. Salahuddin, *Nature* **2019**, *565*, 468.
- [6] W. Zhang, P. K. J. Wong, R. Zhu, A. T. S. Wee, *InfoMat* **2019**, *1*, 479.
- [7] X. Li, T. Cao, Q. Niu, J. Shi, J. Feng, *Proc. Natl. Acad. Sci. USA* **2013**, *110*, 3738.
- [8] Q. Zhang, S. A. Yang, W. Mi, Y. Cheng, U. Schwingenschlögl, *Adv. Mater.* **2016**, *28*, 959.
- [9] S. Lin, A. Carvalho, S. Yan, R. Li, S. Kim, A. Rodin, L. Carvalho, E. M. Chan, X. Wang, A. H. Castro Neto, J. Yao, *Nat. Commun.* **2018**, *9*, 1455.
- [10] B. Zhu, H. Zeng, J. Dai, X. Cui, *Adv. Mater.* **2014**, *26*, 5504.
- [11] N. Singh, U. Schwingenschlögl, *Adv. Mater.* **2017**, *29*, 1600970.
- [12] C. Gong, L. Li, Z. Li, H. Ji, A. Stern, Y. Xia, T. Cao, W. Bao, C. Wang, Y. Wang, Z. Q. Qiu, R. J. Cava, S. G. Louie, J. Xia, X. Zhang, *Nature* **2017**, *546*, 265.
- [13] B. Huang, G. Clark, E. Navarro-Moratalla, D. R. Klein, R. Cheng, K. L. Seyler, D. Zhong, E. Schmidgall, M. A. McGuire, D. H. Cobden, W. Yao, D. Xiao, P. Jarillo Herrero, X. Xu, *Nature* **2017**, *546*, 270.
- [14] K. Chang, J. Liu, H. Lin, N. Wang, K. Zhao, A. Zhang, F. Jin, Y. Zhong, X. Hu, W. Duan, Q. Zhang, L. Fu, Q. K. Xue, X. Chen, S. H. Ji, *Science* **2016**, *353*, 274.
- [15] J. Stajic, *Science* **2018**, *362*, 1124.16.
- [16] H. Li, S. Ruan, Y. Zeng, *Adv. Mater.* **2019**, *31*, 1900065.
- [17] W. Wan, Y. Yao, L. Sun, C. C. Liu, F. Zhang, *Adv. Mater.* **2017**, *29*, 1604788.
- [18] Y. Wan, J. Xiao, J. Li, X. Fang, K. Zhang, L. Fu, P. Li, Z. Song, H. Zhang, Y. Wang, M. Zhao, J. Lu, N. Tang, G. Ran, X. Zhang, Y. Ye, L. Dai, *Adv. Mater.* **2018**, *30*, 1703888.
- [19] T. Song, X. Cai, M. W. Y. Tu, X. Zhang, B. Huang, N. P. Wilson, K. L. Seyler, L. Zhu, T. Taniguchi, K. Watanabe, M. A. McGuire, D. H. Cobden, D. Xiao, W. Yao, X. Xu, *Science* **2018**, *360*, 1214.
- [20] M. Si, A. K. Saha, S. Gao, G. Qiu, J. Qin, Y. Duan, J. Jian, C. Niu, H. Wang, W. Wu, S. K. Gupta, P. D. Ye, *Nat. Electron.* **2019**, *2*, 580.
- [21] X. Liu, M. C. Hersam, *Adv. Mater.* **2018**, *30*, 1801586.
- [22] S. Banerjee, O. Erten, M. Randeria, *Nat. Phys.* **2013**, *9*, 626.
- [23] B. Z. Xu, S. P. Beckman, *2D Mater.* **2016**, *3*, 031003.
- [24] B. Yang, M. F. Tu, J. Kim, Y. Wu, H. Wang, J. Alicea, R. Wu, M. Bockrath, J. Shi, *2D Mater.* **2016**, *3*, 031012.
- [25] J. Quereda, R. Biele, G. Rubio-Bollinger, N. Agraït, R. D'Agosta, A. Castellanos Gomez, *Adv. Opt. Mater.* **2016**, *4*, 1939.
- [26] K. F. Mak, C. Lee, J. Hone, J. Shan, T. F. Heinz, *Phys. Rev. Lett.* **2010**, *105*, 136805.
- [27] K. Xiao, T. Yan, X. Cui, *ACS Nano* **2020**, *14*, 1027.
- [28] Y. Jing, Y. Ma, Y. Li, T. Heine, *Nano Lett.* **2017**, *17*, 1833.
- [29] Q. Cheng, J. Pang, D. Sun, J. Wang, S. Zhang, F. Liu, Y. Chen, R. Yang, N. Liang, X. Lu, Y. Ji, J. Wang, C. Zhang, Y. Sang, H. Liu, W. Zhou, *InfoMat* **2020**, *2*, 656.
- [30] K. L. Seyler, D. Zhong, B. Huang, X. Linpeng, N. P. Wilson, T. Taniguchi, K. Watanabe, W. Yao, D. Xiao, M. A. McGuire, K. M. C. Fu, X. Xu, *Nano Lett.* **2018**, *18*, 3823.
- [31] H. L. Zhuang, P. R. Kent, R. G. Hennig, *Phys. Rev. B* **2016**, *93*, 134407.
- [32] B. Huang, G. Clark, D. R. Klein, D. MacNeill, E. Navarro-Moratalla, K. L. Seyler, N. Wilson, M. A. McGuire, D. H. Cobden, D. Xiao, W. Yao, P. Jarillo-Herrero, X. Xu, *Nat. Nanotechnol.* **2018**, *13*, 544.
- [33] D. H. Kim, K. Kim, K. T. Ko, J. Seo, J. S. Kim, T. H. Jang, Y. Kim, J. Y. Kim, S. W. Cheong, J. H. Park, *Phys. Rev. Lett.* **2019**, *122*, 207201.
- [34] I. Lee, F. G. Utermohlen, D. Weber, K. Hwang, C. Zhang, J. Van Tol, J. E. Goldberger, N. Trivedi, P. C. Hammel, *Phys. Rev. Lett.* **2020**, *124*, 017201.
- [35] L. Li, W. Han, L. Pi, P. Niu, J. Han, C. Wang, B. Su, H. Li, J. Xiong, Y. Bando, T. Zhai, *InfoMat* **2019**, *1*, 54.
- [36] R. Suzuki, M. Sakano, Y. J. Zhang, R. Akashi, D. Morikawa, A. Harasawa, K. Yaji, K. Kuroda, K. Miyamoto, T. Okuda, K. Ishizaka, R. Arita, Y. Iwasa, *Nat. Nanotechnol.* **2014**, *9*, 611.

- [37] H. Zeng, J. Dai, W. Yao, D. Xiao, X. Cui, *Nat. Nanotechnol.* **2012**, *7*, 490.
- [38] H. Yuan, X. Wang, B. Lian, H. Zhang, X. Fang, B. Shen, G. Xu, Y. Xu, S. C. Zhang, H. Y. Hwang, Y. Cui, *Nat. Nanotechnol.* **2014**, *9*, 851.
- [39] B. Ding, Z. Zhang, Y. H. Chen, Y. Zhang, R. J. Blaikie, M. Qiu, *ACS Nano* **2019**, *13*, 1333.
- [40] Y. Ye, J. Xiao, H. Wang, Z. Ye, H. Zhu, M. Zhao, Y. Wang, J. Zhao, X. Yin, X. Zhang, *Nat. Nanotechnol.* **2016**, *11*, 598.
- [41] K. F. Mak, K. He, J. Shan, T. F. Heinz, *Nat. Nanotechnol.* **2012**, *7*, 494.
- [42] W. Y. Tong, S. J. Gong, X. Wan, C. G. Duan, *Nat. Commun.* **2016**, *7*, 13612.
- [43] D. Zhong, K. L. Seyler, X. Linpeng, R. Cheng, N. Sivasdas, B. Huang, E. Schmidgall, T. Taniguchi, K. Watanabe, M. A. McGuire, W. Yao, D. Xiao, K. M. C. Fu, X. Xu, *Sci. Adv.* **2017**, *3*, e1603113.
- [44] J. Qi, H. Wang, X. Chen, X. Qian, *Appl. Phys. Lett.* **2018**, *113*, 043102.
- [45] Z. Tu, M. Wu, X. C. Zeng, *J. Phys. Chem. Lett.* **2017**, *8*, 1973.
- [46] M. Wu, J. D. Burton, E. Y. Tsymbal, X. C. Zeng, P. Jena, *Phys. Rev. B* **2013**, *87*, 081406.
- [47] M. Wu, X. C. Zeng, *Nano Lett.* **2017**, *17*, 6309.
- [48] C. Huang, Y. Du, H. Wu, H. Xiang, K. Deng, E. Kan, *Phys. Rev. Lett.* **2018**, *120*, 147601.
- [49] J. A. Mundy, C. M. Brooks, M. E. Holtz, J. A. Moyer, H. Das, A. F. Rébola, J. T. Heron, J. D. Clarkson, S. M. Disseler, Z. Liu, A. Farhan, R. Held, R. Hovden, E. Padgett, Q. Mao, H. Paik, R. Misra, L. F. Kourkoutis, E. Arenholz, A. Scholl, J. A. Borchers, W. D. Ratcliff, R. Ramesh, C. J. Fennie, P. Schiffer, D. A. Muller, D. G. Schlom, *Nature* **2016**, *537*, 523.
- [50] K. Yamauchi, S. Picozzi, *Phys. Rev. Lett.* **2010**, *105*, 107202.
- [51] J. E. Rault, W. Ren, S. Prosandeev, S. Lisenkov, D. Sando, S. Fusil, M. Bibes, A. Barthélémy, L. Bellaiche, N. Barrett, *Phys. Rev. Lett.* **2012**, *109*, 267601.
- [52] C. Li, L. Huang, T. Li, W. Lü, X. Qiu, Z. Huang, Z. Liu, S. Zeng, R. Guo, Y. Zhao, K. Zeng, M. Coey, J. Chen, Ariando, T. Venkatesan, *Nano Lett.* **2015**, *15*, 2568.
- [53] K. Liu, J. Lu, S. Picozzi, L. Bellaiche, H. Xiang, *Phys. Rev. Lett.* **2018**, *121*, 027601.
- [54] Z. Fei, W. Zhao, T. A. Palomaki, B. Sun, M. K. Miller, Z. Zhao, J. Yan, X. Xu, D. H. Cobden, *Nature* **2018**, *560*, 336.
- [55] X. Liu, Y. Yang, T. Hu, G. Zhao, C. Chen, W. Ren, *Nanoscale* **2019**, *11*, 18575.
- [56] A. Allain, J. Kang, K. Banerjee, A. Kis, *Nat. Mater.* **2015**, *14*, 1195.
- [57] Y. Liu, J. Guo, E. Zhu, L. Liao, S.-J. Lee, M. Ding, I. Shakir, V. Gambin, Y. Huang, X. Duan, *Nature* **2018**, *557*, 696.
- [58] L. Fu, C. L. Kane, *Phys. Rev. Lett.* **2008**, *100*, 096407.
- [59] Q. Li, C. He, Y. Wang, E. Liu, M. Wang, Y. Wang, J. Zeng, Z. Ma, T. Cao, C. Yi, N. Wang, K. Watanabe, T. Taniguchi, L. Shao, Y. Shi, X. Chen, S. J. Liang, Q. H. Wang, F. Miao, *Nano Lett.* **2018**, *18*, 7962.
- [60] C. K. Safeer, J. Ingla-Aynés, F. Herling, J. H. Garcia, M. Vila, N. Ontoso, M. R. Calvo, S. Roche, L. E. Hueso, F. Casanova, *Nano Lett.* **2019**, *19*, 5133.
- [61] C. Huang, A. Narayan, E. Zhang, Y. Liu, X. Yan, J. Wang, C. Zhang, W. Wang, T. Zhou, C. Yi, S. Liu, J. Ling, H. Zhang, R. Liu, R. Sankar, F. Chou, Y. Wang, Y. Shi, K. T. Law, S. Sanvito, P. Zhou, Z. Han, F. Xiu, *ACS Nano* **2018**, *12*, 7185.
- [62] T. Taniguchi, S. Li, L. Nurdijayanto, Y. Kobayashi, T. Saito, Y. Miyata, S. Obata, K. Saiki, H. Yokoi, K. Watanabe, T. Taniguchi, K. Tsukagoshi, Y. Ebina, T. Sasaki, M. Osada, *ACS Nano* **2019**, *13*, 11214.
- [63] E. C. O'Farrell, A. Avsar, J. Y. Tan, G. Eda, B. Özyilmaz, *Nano Lett.* **2015**, *15*, 5682.
- [64] T. Norden, C. Zhao, P. Zhang, R. Sabirianov, A. Petrou, H. Zeng, *Nat. Commun.* **2019**, *10*, 4163.
- [65] X. Qian, J. Liu, L. Fu, J. Li, *Science* **2014**, *346*, 1344.
- [66] A. Manchon, H. C. Koo, J. Nitta, S. M. Frolov, R. A. Duine, *Nat. Mater.* **2015**, *14*, 871.
- [67] T. S. Ghiasi, A. A. Kaverzin, P. J. Blah, B. J. Van Wees, *Nano Lett.* **2019**, *19*, 5959.
- [68] H. Ai, X. Ma, X. Shao, W. Li, M. Zhao, *Phys. Rev. Mater.* **2019**, *3*, 054407.
- [69] S. Jiang, L. Li, Z. Wang, K. F. Mak, J. Shan, *Nat. Nanotechnol.* **2018**, *13*, 549.
- [70] S. Jiang, J. Shan, K. F. Mak, *Nat. Mater.* **2018**, *17*, 406.
- [71] Z. Wang, T. Zhang, M. Ding, B. Dong, Y. Li, M. Chen, X. Li, J. Huang, H. Wang, X. Zhao, Y. Li, D. Li, C. Jia, L. Sun, H. Guo, Y. Ye, D. Sun, Y. Chen, T. Yang, J. Zhang, S. Ono, Z. Han, Z. Zhang, *Nat. Nanotechnol.* **2018**, *13*, 554.
- [72] Z. Wang, D. Sapkota, T. Taniguchi, K. Watanabe, D. Mandrus, A. F. Morpurgo, *Nano Lett.* **2018**, *18*, 4303.
- [73] Z. Fei, B. Huang, P. Malinowski, W. Wang, T. Song, J. Sanchez, W. Yao, D. Xiao, X. Zhu, A. F. May, W. Wu, D. H. Cobden, J. H. Chu, X. Xu, *Nat. Mater.* **2018**, *17*, 778.
- [74] F. Liu, L. You, K. L. Seyler, X. Li, P. Yu, J. Lin, X. Wang, J. Zhou, H. Wang, H. He, S. T. Pantelides, W. Zhou, P. Sharma, X. Xu, P. M. Ajayan, J. Wang, Z. Liu, *Nat. Commun.* **2016**, *7*, 12357.
- [75] M. Si, P. Y. Liao, G. Qiu, Y. Duan, P. D. Ye, *ACS Nano* **2018**, *12*, 6700.
- [76] W. Chen, Z. Sun, Z. Wang, L. Gu, X. Xu, S. Wu, C. Gao, *Science* **2019**, *366*, 983.
- [77] M. Bonilla, S. Kolekar, Y. Ma, H. C. Diaz, V. Kalappattil, R. Das, T. Eggers, H. R. Gutierrez, M. H. Phan, M. Batzill, *Nat. Nanotechnol.* **2018**, *13*, 289.
- [78] Y. Bao, P. Song, Y. Liu, Z. Chen, M. Zhu, I. Abdelwahab, J. Su, W. Fu, X. Chi, W. Yu, W. Liu, X. Zhao, Q. H. Xu, M. Yang, K. P. Loh, *Nano Lett.* **2019**, *19*, 5109.
- [79] H. Liu, L. Bao, Z. Zhou, B. Che, R. Zhang, C. Bian, R. Ma, L. Wu, H. Yang, J. Li, C. Gu, C. M. Shen, S. Du, H. J. Gao, *Nano Lett.* **2019**, *19*, 4551.
- [80] Z. Zhang, J. Niu, P. Yang, Y. Gong, Q. Ji, J. Shi, Q. Fang, S. Jiang, H. Li, X. Zhou, L. Gu, X. Wu, Y. Zhang, *Adv. Mater.* **2017**, *29*, 1702359.
- [81] Z. Zhang, Y. Gong, X. Zou, P. Liu, P. Yang, J. Shi, L. Zhao, Q. Zhang, L. Gu, Y. Zhang, *ACS Nano* **2019**, *13*, 885.
- [82] Y. Zhou, D. Wu, Y. Zhu, Y. Cho, Q. He, X. Yang, K. Herrera, Z. Chu, Y. Han, M. C. Downer, H. Peng, K. Lai, *Nano Lett.* **2017**, *17*, 5508.
- [83] C. Cui, W. J. Hu, X. Yan, C. Addiego, W. Gao, Y. Wang, Z. Wang, L. Li, Y. Cheng, P. Li, X. Zhang, H. N. Alshareef, T. Wu, W. Zhu, X. Pan, L. J. Li, *Nano Lett.* **2018**, *18*, 1253.
- [84] X. Zhu, Y. Guo, H. Cheng, J. Dai, X. An, J. Zhao, K. Tian, S. Wei, X. C. Zeng, C. Wu, Y. Xie, *Nat. Commun.* **2016**, *7*, 11210.
- [85] K. Zhang, S. Feng, J. Wang, A. Azcatl, N. Lu, R. Addou, N. Wang, C. Zhou, J. Lerach, V. Bojan, M. J. Kim, L. Q. Chen, R. M. Wallace, M. Terrones, J. Zhu, J. A. Robinson, *Nano Lett.* **2015**, *15*, 6586.
- [86] H. Duan, P. Guo, C. Wang, H. Tan, W. Hu, W. Yan, C. Ma, L. Cai, L. Song, W. Zhang, Z. Sun, L. Wang, W. Zhao, Y. Yin, X. Li, S. Wei, *Nat. Commun.* **2019**, *10*, 1584.
- [87] S. Fu, K. Kang, K. Shayan, A. Yoshimura, S. Dadrás, X. Wang, L. Zhang, S. Chen, N. Liu, A. Jindal, X. Li, A. N. Pasupathy, A. N. Vamivakas, V. Meunier, S. Strauf, E. H. Yang, *Nat. Commun.* **2020**, *11*, 2034.
- [88] B. Li, T. Xing, M. Zhong, L. Huang, N. Lei, J. Zhang, J. Li, Z. Wei, *Nat. Commun.* **2017**, *8*, 1958.
- [89] V. Kochat, A. Apte, J. A. Hachtel, H. Kumazoe, A. Krishnamoorthy, S. Susarla, C. Idrobo, F. Shimojo, P. Vashishta, R. Kalia, A. Nakano, C. S. Tiwary, P. M. Ajayan, *Adv. Mater.* **2017**, *29*, 1703754.
- [90] Z. Guguchia, A. Kerelsky, D. Edelberg, S. Banerjee, F. Von Rohr, H. Sкулlion, M. Augustin, M. Scully, D. A. Rhodes, Z. Shermadini, D. Luetkens, A. Shengelaya, C. Baines, E. Morenzoni, A. Amato, J. C. Hone, R. Khasanov, S. J. Billinge, E. Santos, A. N. Pasupathy, Y. J. Uemura, *Sci. Adv.* **2018**, *4*, eaat3672.
- [91] A. Avsar, A. Ciarrocchi, M. Pizzochero, D. Unuchek, O. V. Yazyev, A. Kis, *Nat. Nanotechnol.* **2019**, *14*, 674.

- [92] C. Y. Hwang, *J. Korean Magn. Soc.* **2011**, 21, 141.
- [93] J. Zak, E. R. Moog, C. Liu, S. D. Bader, *J. Magn. Magn. Mater.* **1990**, 89, 107.
- [94] J. Zak, E. Moog, C. Liu, S. Bader, *Phys. Rev. B* **1991**, 43, 6423.
- [95] Z. Q. Qiu, S. D. Bader, *J. Magn. Magn. Mater.* **1999**, 200, 664.
- [96] S. A. Denev, T. T. Lummen, E. Barnes, A. Kumar, V. Gopalan, *J. Am. Ceram. Soc.* **2011**, 94, 2699.
- [97] Z. Sun, Y. Yi, T. Song, G. Clark, B. Huang, Y. Shan, S. Wu, D. Huang, C. Gao, Z. Chen, M. McGuire, T. Cao, D. Xiao, W. T. Liu, W. Yao, X. Xu, S. Wu, *Nature* **2019**, 572, 497.
- [98] H. Chu, C. J. Roh, J. O. Island, C. Li, S. Lee, J. Chen, J. G. Park, A. F. Young, J. S. Lee, D. Hsieh, *Phys. Rev. Lett.* **2020**, 124, 027601.
- [99] J. Deng, Y. Liu, M. Li, S. Xu, Y. Lun, P. Lv, T. Xia, P. Gao, X. Wang, J. Hong, *Small* **2020**, 16, 1904529.
- [100] S. Yuan, X. Luo, H. L. Chan, C. Xiao, Y. Dai, M. Xie, J. Hao, *Nat. Commun.* **2019**, 10, 1775.
- [101] L. Thiel, Z. Wang, M. A. Tschudin, D. Rohner, I. Gutiérrez-Lezama, N. Ubrig, M. Gibertini, E. Giannini, A. F. Morpurgo, P. Maletinsky, *Science* **2019**, 364, 973.
- [102] N. Tombros, S. Tanabe, A. Veligura, C. Jozsa, M. Popinciuc, H. T. Jonkman, B. J. Van Wees, *Phys. Rev. Lett.* **2008**, 101, 046601.
- [103] W. Han, R. K. Kawakami, M. Gmitra, J. Fabian, *Nat. Nanotechnol.* **2014**, 9, 794.
- [104] M. H. Guimarães, P. J. Zomer, J. Ingla-Aynés, J. C. Brant, N. Tombros, B. J. Van Wees, *Phys. Rev. Lett.* **2014**, 113, 086602.
- [105] D. Huertas-Hernando, F. Guinea, A. Brataas, *Phys. Rev. B* **2006**, 74, 155426.
- [106] N. Tombros, C. Jozsa, M. Popinciuc, H. T. Jonkman, B. J. Van Wees, *Nature* **2007**, 448, 571.
- [107] J. Ingla-Aynés, M. H. Guimarães, R. J. Meijerink, P. J. Zomer, B. J. Van Wees, *Phys. Rev. B* **2015**, 92, 201410.
- [108] M. Drögel, C. Franzen, F. Volmer, T. Pohlmann, L. Banszerus, M. Wolter, K. Watanabe, T. Taniguchi, C. Stampfer, B. Beschoten, *Nano Lett.* **2016**, 16, 3533.
- [109] M. Gurram, S. Omar, S. Zihlmann, P. Makk, C. Schönenberger, B. J. Van Wees, *Phys. Rev. B* **2016**, 93, 115441.
- [110] J. Ingla-Aynés, R. J. Meijerink, B. J. Van Wees, *Nano Lett.* **2016**, 16, 4825.
- [111] J. C. Leutenantsmeyer, J. Ingla-Aynés, M. Gurram, B. J. Van Wees, *J. Appl. Phys.* **2018**, 124, 194301.
- [112] S. Singh, J. Katoch, T. Zhu, R. J. Wu, A. S. Ahmed, W. Amamou, D. Wang, K. A. Mkhoyan, R. K. Kawakami, *Nano Lett.* **2017**, 17, 7578.
- [113] W. Han, K. Pi, K. M. McCreary, Y. Li, J. J. I. Wong, A. G. Swartz, R. K. Kawakami, *Phys. Rev. Lett.* **2010**, 105, 167202.
- [114] Y. K. Luo, J. Xu, T. Zhu, G. Wu, E. J. McCormick, W. Zhan, M. R. Neupane, R. K. Kawakami, *Nano Lett.* **2017**, 17, 3877.
- [115] K. Behnia, *Nat. Nanotechnol.* **2012**, 7, 488.
- [116] J. H. Garcia, A. W. Cummings, S. Roche, *Nano Lett.* **2017**, 17, 5078.
- [117] W. Saverio Torres, J. F. Sierra, L. A. Benítez, F. Bonell, M. V. Costache, S. O. Valenzuela, *2D Mater.* **2017**, 4, 041008.
- [118] W. Yan, E. Sagasta, M. Ribeiro, Y. Niimi, L. E. Hueso, F. Casanova, *Nat. Commun.* **2017**, 8, 661.
- [119] L. A. Benítez, W. Saverio Torres, J. F. Sierra, M. Timmermans, J. H. Garcia, S. Roche, M. V. Costache, S. O. Valenzuela, *Nat. Mater.* **2020**, 19, 170.
- [120] A. Avsar, J. Y. Tan, M. Kurpas, M. Gmitra, K. Watanabe, T. Taniguchi, J. Fabian, B. Özyilmaz, *Nat. Phys.* **2017**, 13, 888.
- [121] T. S. Ghiasi, J. Ingla-Aynés, A. A. Kaverzin, B. J. Van Wees, *Nano Lett.* **2017**, 17, 7528.
- [122] J. Xu, S. Singh, J. Katoch, G. Wu, T. Zhu, I. Žutić, R. K. Kawakami, *Nat. Commun.* **2018**, 9, 2869.
- [123] A. Dankert, S. P. Dash, *Nat. Commun.* **2017**, 8, 16093.
- [124] D. Khokhriakov, A. W. Cummings, K. Song, M. Vila, B. Karpiak, A. Dankert, S. Roche, S. P. Dash, *Sci. Adv.* **2018**, 4, eaat9349.
- [125] C. Gong, L. Li, Z. Li, H. Ji, A. Stern, Y. Xia, T. Cao, W. Bao, C. Wang, Y. Wang, Z. Q. Qiu, R. J. Cava, S. G. Louie, J. Xia, X. Zhang, *Nature* **2017**, 546, 265.
- [126] D. Ghazaryan, M. T. Greenaway, Z. Wang, V. H. Guarochico-Moreira, I. J. VeraMarun, J. Yin, Y. Liao, S. V. Morozov, O. Kristanovski, A. I. Lichtenstein, M. I. Katsnelson, F. Withers, A. Mishchenko, L. Eaves, A. K. Geim, K. S. Novoselov, A. Misra, *Nat. Electron.* **2018**, 1, 344.
- [127] Y. Zhang, J. Chu, L. Yin, T. A. Shifa, Z. Cheng, R. Cheng, F. Wang, Y. Wen, X. Zhan, Z. Wang, J. He, *Adv. Mater.* **2019**, 31, 1900056.
- [128] Y. Deng, Y. Yu, Y. Song, J. Zhang, N. Z. Wang, Z. Sun, Y. Yi, Y. Z. Wu, S. Wu, J. Zhu, J. Wang, X. H. Chen, Y. Zhang, *Nature* **2018**, 563, 94.
- [129] S. Jiang, L. Li, Z. Wang, J. Shan, K. F. Mak, *Nat. Electron.* **2019**, 2, 159.
- [130] M. Alghamdi, M. Lohmann, J. Li, P. R. Jothi, Q. Shao, M. Aldosary, T. Su, B. P. Fokwa, J. Shi, *Nano Lett.* **2019**, 19, 4400.
- [131] T. Li, S. Jiang, N. Sivasdas, Z. Wang, Y. Xu, D. Weber, J. E. Goldberger, K. Watanabe, T. Taniguchi, C. J. Fennie, K. Fai Mak, J. Shan, *Nat. Mater.* **2019**, 18, 1303.
- [132] W. Yu, J. Li, T. S. Herg, Z. Wang, X. Zhao, X. Chi, W. Fu, I. Abdelwahab, J. Zhou, J. Dan, Z. Chen, Z. Chen, Z. Li, J. Lu, S. J. Pennycook, Y. P. Feng, J. Ding, K. P. Loh, *Adv. Mater.* **2019**, 31, 1903779.
- [133] D. J. O'Hara, T. Zhu, A. H. Trout, A. S. Ahmed, Y. K. Luo, C. H. Lee, M. R. Brenner, S. Rajan, J. A. Gupta, D. W. McComb, R. K. Kawakami, *Nano Lett.* **2018**, 18, 3125.
- [134] A. F. May, D. Ovchinnikov, Q. Zheng, R. Hermann, S. Calder, B. Huang, Z. Fei, Y. Liu, X. Xu, M. A. McGuire, *ACS Nano* **2019**, 13, 4436.
- [135] C. Huang, J. Feng, J. Zhou, H. Xiang, K. Deng, E. Kan, *J. Am. Chem. Soc.* **2019**, 141, 12413.
- [136] Y. Tian, W. Gao, E. A. Henriksen, J. R. Chelikowsky, L. Yang, *Nano Lett.* **2019**, 19, 7673.
- [137] C. Cardoso, D. Soriano, N. A. García-Martínez, J. Fernández-Rossier, *Phys. Rev. Lett.* **2018**, 121, 067701.
- [138] N. Nagaosa, J. Sinova, S. Onoda, A. H. MacDonald, N. P. Ong, *Rev. Mod. Phys.* **2010**, 82, 1539.
- [139] D. Xiao, M. C. Chang, Q. Niu, *Rev. Mod. Phys.* **2010**, 82, 1959.
- [140] D. Xiao, W. Yao, Q. Niu, *Phys. Rev. Lett.* **2007**, 99, 236809.
- [141] W. Yao, D. Xiao, Q. Niu, *Phys. Rev. B* **2008**, 77, 235406.
- [142] D. Xiao, G. B. Liu, W. Feng, X. Xu, W. Yao, *Phys. Rev. Lett.* **2012**, 108, 196802.
- [143] W. Kohn, J. M. Luttinger, *Phys. Rev. Lett.* **1965**, 15, 524.
- [144] P. Gong, H. Yu, Y. Wang, W. Yao, *Phys. Rev. B* **2017**, 95, 125420.
- [145] T. Cao, M. Wu, S. G. Louie, *Phys. Rev. Lett.* **2018**, 120, 087402.
- [146] X. Zhang, W.-Y. Shan, D. Xiao, *Phys. Rev. Lett.* **2018**, 120, 077401.
- [147] A. R. Akhmerov, C. W. J. Beenakker, *Phys. Rev. Lett.* **2007**, 98, 157003.
- [148] C. R. Zhu, K. Zhang, M. Glazov, B. Urbaszek, T. Amand, Z. W. Ji, B. L. Liu, X. Marie, *Phys. Rev. B* **2014**, 90, 161302.
- [149] W. T. Hsu, Y. L. Chen, C. H. Chen, P. S. Liu, T. H. Hou, L. J. Li, W. H. Chang, *Nat. Commun.* **2015**, 6, 8963.
- [150] G. Moody, K. Tran, X. Lu, T. Autry, J. M. Fraser, R. P. Mirin, L. Yang, X. Li, K. L. Silverman, *Phys. Rev. Lett.* **2018**, 121, 057403.
- [151] A. Singh, K. Tran, J. Seifert, Y. Wang, K. Hao, X. Li, D. Pleskot, N. M. Gabor, S. Helmrich, M. Kolarczik, N. Owschmikow, U. Woggon, *Phys. Rev. Lett.* **2016**, 117, 257402.
- [152] J. Kim, C. Jin, B. Chen, H. Cai, T. Zhao, P. Lee, S. Kahn, K. Watanabe, T. Taniguchi, S. Tongay, M. F. Crommie, F. Wang, *Sci. Adv.* **2017**, 3, e1700518.
- [153] K. Tran, G. Moody, F. Wu, X. Lu, J. Choi, K. Kim, A. Rai, D. A. Sanchez, J. Quan, A. Singh, J. Embley, A. Zepeda, M. Campbell, T. Autry, T. Taniguchi, J. Watanabe, N. Lu, S. K. Banerjee, K. L. Silverman, S. Kim, E. Tutuc, L. Yang, A. H. MacDonald, X. Li, *Nature* **2019**, 567, 71.

- [154] K. Hao, G. Moody, F. Wu, C. K. Dass, L. Xu, C. H. Chen, L. Sun, M. Y. Li, L. J. Li, A. H. MacDonald, X. Li, *Nat. Phys.* **2016**, *12*, 677.
- [155] A. M. Jones, H. Yu, N. J. Ghimire, S. Wu, G. Aivazian, J. S. Ross, B. Zhao, J. Yan, D. G. Mandrus, D. Xiao, W. Yao, X. Xu, *Nat. Nanotechnol.* **2013**, *8*, 634.
- [156] S. Dufferwiel, T. P. Lyons, D. D. Solnyshkov, A. A. Trichet, A. Catanzaro, F. Withers, G. Malpuech, J. M. Smith, K. S. Novoselov, M. S. Skolnick, D. N. Krizhanovskii, A. I. Tartakovskii, *Nat. Commun.* **2018**, *9*, 4797.
- [157] X. W. Shen, W. Y. Tong, S. J. Gong, C. G. Duan, *2D Mater.* **2017**, *5*, 011001.
- [158] G. Aivazian, Z. Gong, A. M. Jones, R. L. Chu, J. Yan, D. G. Mandrus, C. Zhang, D. Cobden, W. Yao, X. Xu, *Nat. Phys.* **2015**, *11*, 148.
- [159] A. Srivastava, M. Sidler, A. V. Allain, D. S. Lembke, A. Kis, A. Imamolu, *Nat. Phys.* **2015**, *11*, 141.
- [160] J. Zhang, L. Du, S. Feng, R.-W. Zhang, B. Cao, C. Zou, Y. Chen, M. Liao, B. Zhang, S. A. Yang, G. Zhang, T. Yu, *Nat. Commun.* **2019**, *10*, 4226.
- [161] T. P. Lyons, S. Dufferwiel, M. Brooks, F. Withers, T. Taniguchi, K. Watanabe, K. S. Novoselov, G. Burkard, A. I. Tartakovskii, *Nat. Commun.* **2019**, *10*, 2330.
- [162] A. Belianinov, Q. He, A. Dziaugys, P. Maksymovych, E. Eliseev, A. Borisevich, A. Morozovska, J. Banys, Y. Vysochanskii, S. V. Kalinin, *Nano Lett.* **2015**, *15*, 3808.
- [163] F. Xue, W. Hu, K. Lee, L. Lu, J. Zhang, H. Tang, A. Han, W. Hsu, S. Tu, W. Chang, C. Lien, J. He, Z. Zhang, L. Li, X. Zhang, *Adv. Funct. Mater.* **2018**, *28*, 1803738.
- [164] C. Zheng, L. Yu, L. Zhu, J. L. Collins, D. Kim, Y. Lou, C. Xu, M. Li, Z. Wei, Y. Zhang, M. T. Edmonds, S. Li, J. Seidel, Y. Zhu, J. Z. Liu, W. X. Tang, M. S. Fuhrer, *Sci. Adv.* **2018**, *4*, eaar7720.
- [165] T. Ghosh, M. Samanta, A. Vasdev, K. Dolui, J. Ghatak, T. Das, G. Sheet, K. Biswas, *Nano Lett.* **2019**, *19*, 5703.
- [166] J. W. Chen, S. T. Lo, S. C. Ho, S. S. Wong, T.-H. Y. Vu, X. Q. Zhang, Y. D. Liu, Y. Y. Chiou, Y. X. Chen, J. C. Yang, Y. C. Chen, Y. H. Chu, Y. H. Lee, C. J. Chung, T. M. Chen, C. H. Chen, C. L. Wu, *Nat. Commun.* **2018**, *9*, 3143.
- [167] J. A. Brehm, S. M. Neumayer, L. Tao, A. O'Hara, M. Chyasnovich, M. A. Susner, M. A. McGuire, S. V. Kalinin, S. Jesse, P. Ganesh, S. T. Pantelides, P. Maksymovych, N. Balke, *Nat. Mater.* **2020**, *19*, 43.
- [168] J. Xiao, Y. Wang, H. Wang, C. D. Pemmaraju, S. Wang, P. Muscher, E. J. Sie, C. M. Nyby, T. P. Devereaux, X. Qian, X. Zhang, A. M. Lindenberg, *Nat. Phys.* **2020**, <https://doi.org/10.1038/s41567-020-0947-0>.
- [169] Z. Ni, E. Minamitani, K. Kawahara, R. Arafune, C. Lin, N. Takagi, S. Watanabe, *J. Phys. Chem. C* **2020**, *124*, 2008.
- [170] Q. Yang, M. Wu, J. Li, *J. Phys. Chem. Lett.* **2018**, *9*, 7160.
- [171] J. Xiao, H. Zhu, Y. Wang, W. Feng, Y. Hu, A. Dasgupta, Y. Han, Y. Wang, D. A. Muller, L. W. Martin, P. Hu, X. Zhang, *Phys. Rev. Lett.* **2018**, *120*, 227601.
- [172] F. Xue, X. He, J. R. D. Retamal, A. Han, J. Zhang, Z. Liu, J. Huang, W. Hu, V. Tung, J. He, L. Li, X. Zhang, *Adv. Mater.* **2019**, *31*, 1901300.
- [173] G. Wu, B. Tian, L. Liu, W. Lv, S. Wu, X. Wang, Y. Chen, J. Li, Z. Wang, S. Wu, H. Shen, T. Lin, P. Zhou, Q. Liu, C. Duan, S. Zhang, X. Meng, S. Wu, W. Hu, X. Wang, J. Chu, J. Wang, *Nat. Electron.* **2020**, *3*, 43.
- [174] A. Lipatov, T. Li, N. S. Vorobeva, A. Sinitskii, A. Gruverman, *Nano Lett.* **2019**, *19*, 3194.
- [175] M. Si, C. J. Su, C. J. Jiang, N. J. Conrad, H. Zhou, K. D. Maize, G. Qiu, C. T. Wu, A. Shakouri, M. A. Alam, P. D. Ye, *Nat. Nanotechnol.* **2018**, *13*, 24.
- [176] M. Si, C. J. Jiang, W. Chung, Y. Du, M. A. Alam, P. D. Ye, *Nano Lett.* **2018**, *18*, 3682.
- [177] X. Wang, P. Yu, Z. Lei, C. Zhu, X. Cao, F. Liu, L. You, Q. Zeng, Y. Deng, C. Zhu, J. Zhou, Q. Fu, J. Wang, Y. Huang, Z. Liu, *Nat. Commun.* **2019**, *10*, 3037.
- [178] N. Park, H. Kang, J. Park, Y. Lee, Y. Yun, J.-H. Lee, S.-G. Lee, Y. H. Lee, D. Suh, *ACS Nano* **2015**, *9*, 10729.
- [179] A. Lipatov, P. Sharma, A. Gruverman, A. Sinitskii, *ACS Nano* **2015**, *9*, 8089.
- [180] Y. T. Lee, H. Kwon, J. S. Kim, H. H. Kim, Y. J. Lee, J. A. Lim, Y. W. Song, Y. Yi, W. K. Choi, D. K. Hwang, S. Im, *ACS Nano* **2015**, *9*, 10394.
- [181] Y. Jeong, H. Jin, J. H. Park, Y. Cho, M. Kim, S. Hong, W. Jo, Y. Yi, S. Im, *Adv. Funct. Mater.* **2020**, *30*, 1908210.
- [182] Z. D. Luo, X. Xia, M. M. Yang, N. R. Wilson, A. Gruverman, M. Alexe, *ACS Nano* **2020**, *14*, 746.
- [183] W. Hou, A. Azizimanesh, A. Sewaket, T. Peña, C. Watson, M. Liu, H. Askari, S. M. Wu, *Nat. Nanotechnol.* **2019**, *14*, 668.
- [184] C. Ko, Y. Lee, Y. Chen, J. Suh, D. Fu, A. Suslu, S. Lee, J. D. Clarkson, H. S. Choe, S. Tongay, R. Ramesh, J. Wu, *Adv. Mater.* **2016**, *28*, 2923.
- [185] Y. Hou, J. Kim, R. Wu, *Sci. Adv.* **2019**, *5*, eaaw1874.
- [186] S. M. Poh, S. J. R. Tan, H. Wang, P. Song, I. H. Abidi, X. Zhao, J. Dan, J. Chen, Z. Luo, S. J. Pennycook, A. H. Castro Neto, K. P. Loh, *Nano Lett.* **2018**, *18*, 6340.
- [187] S. Wan, Y. Li, W. Li, X. Mao, C. Wang, C. Chen, J. Dong, A. Nie, J. Xiang, Z. Liu, W. Zhu, H. Zeng, *Adv. Funct. Mater.* **2019**, *29*, 1808606.
- [188] J. Wu, H. Chen, N. Yang, J. Cao, X. Yan, F. Liu, Q. Sun, X. Ling, J. Guo, H. Wang, *Nat. Electron.* **2020**, <https://doi.org/10.1038/s41928-020-0441-9>.
- [189] Z. Zhang, Z. Wang, T. Shi, C. Bi, F. Rao, Y. Cai, Q. Liu, H. Wu, P. Zhou, *InfoMat* **2020**, *2*, 261.
- [190] X. Wang, P. Wang, J. Wang, W. Hu, X. Zhou, N. Guo, H. Huang, S. Sun, H. Shen, T. Lin, M. Tang, L. Liao, A. Jiang, J. Sun, X. Meng, X. Chen, W. Lu, J. Chu, *Adv. Mater.* **2015**, *27*, 6575.
- [191] L. Tu, R. Cao, X. Wang, Y. Chen, S. Wu, F. Wang, Z. Wang, H. Shen, T. Lin, P. Zhou, X. Meng, W. Hu, Q. Liu, J. Wang, M. Liu, J. Chu, *Nat. Commun.* **2020**, *11*, 101.
- [192] L. Lv, F. Zhuge, F. Xie, X. Xiong, Q. Zhang, N. Zhang, Y. Huang, T. Zhai, *Nat. Commun.* **2019**, *10*, 3331.
- [193] G. Wu, X. Wang, Y. Chen, S. Wu, B. Wu, Y. Jiang, H. Shen, T. Lin, Q. Liu, X. Wang, P. Zhou, S. Zhang, W. Hu, X. Meng, J. Chu, *J. Wang, Adv. Mater.* **2020**, *32*, 1907937.
- [194] B. Wen, Y. Zhu, D. Yudistira, A. Boes, L. Zhang, T. Yidirim, B. Liu, H. Yan, X. Sun, Y. Zhou, Y. Xue, Y. Zhang, L. Fu, A. Mitchell, H. Zhang, Y. Lu, *ACS Nano* **2019**, *13*, 5335.
- [195] T. Li, A. Lipatov, H. Lu, H. Lee, J. W. Lee, E. Torun, L. Wirtz, C. B. Eom, J. Íñiguez, A. Sinitskii, A. Gruverman, *Nat. Commun.* **2018**, *9*, 3344.
- [196] J. Wang, J. Han, X. Chen, X. Wang, *InfoMat* **2019**, *1*, 33.
- [197] Y. Wang, C. Xiao, M. Chen, C. Hua, J. Zou, C. Wu, J. Jiang, S. A. Yang, Y. Lu, W. Ji, *Mater. Horiz.* **2018**, *5*, 521.
- [198] C. Xiao, F. Wang, S. A. Yang, Y. Lu, Y. Feng, S. Zhang, *Adv. Funct. Mater.* **2018**, *28*, 1707383.
- [199] S. N. Shirodkar, U. V. Waghmare, *Phys. Rev. Lett.* **2014**, *112*, 157601.
- [200] D. Di Sante, A. Stroppa, P. Barone, M. H. Whangbo, S. Picozzi, *Phys. Rev. B* **2015**, *91*, 161401.
- [201] W. Song, R. Fei, L. Yang, *Phys. Rev. B* **2017**, *96*, 235420.
- [202] B. Xu, H. Xiang, Y. Xia, K. Jiang, X. Wan, J. He, J. Yin, Z. Liu, *Nanoscale* **2017**, *9*, 8427.
- [203] Y. Jia, M. Zhao, G. Gou, X. C. Zeng, J. Li, *Nanoscale Horiz.* **2019**, *4*, 1113.
- [204] M. Wu, S. Dong, K. Yao, J. Liu, X. C. Zeng, *Nano Lett.* **2016**, *16*, 7309.
- [205] E. Bruyer, D. Di Sante, P. Barone, A. Stroppa, M.-H. Whangbo, S. Picozzi, *Phys. Rev. B* **2016**, *94*, 195402.

- [206] J. Fang, Z. Zhou, M. Xiao, Z. Lou, Z. Wei, G. Shen, *InfoMat* **2020**, 2, 291.
- [207] L. Li, M. Wu, *ACS Nano* **2017**, 11, 6382.
- [208] G. Long, H. Henck, M. Gibertini, D. Dumcenco, Z. Wang, T. Taniguchi, K. Watanabe, E. Giannini, A. F. Morpurgo, *Nano Lett.* **2020**, 20, 2452.
- [209] K. Kim, S. Y. Lim, J. Lee, S. Lee, T. Y. Kim, K. Park, G. S. Jeon, C. Park, J. Park, H. Cheong, *Nat. Commun.* **2019**, 10, 345.
- [210] H. Wang, X. Qian, *2D Mater.* **2017**, 4, 015042.
- [211] Z. B. Yang, Z. H. Wu, Y. X. Lyu, J. H. Hao, J. Hao, *InfoMat* **2019**, 1, 98.
- [212] X. Tong, K. Liu, M. Zeng, L. Fu, *InfoMat* **2019**, 1, 460.
- [213] L. Xing, X. Yan, J. Zheng, G. Xu, Z. Lu, L. Liu, J. Wang, P. Wang, X. Pan, L. Jiao, *InfoMat* **2019**, 1, 552.
- [214] L. X. Kang, X. C. Yu, X. X. Zhao, Q. L. Ouyang, J. Di, M. Z. Xu, D. Tian, W. L. Gan, C. C. I. Ang, S. C. Ning, Q. D. Fu, J. D. Zhou, R. G. Kutty, Y. Deng, P. Song, Q. S. Zeng, S. J. Pennycook, J. Shen, K. T. Yong, Z. Liu, *InfoMat* **2020**, 2, 593.
- [215] Z. Y. Al Balushi, K. Wang, R. K. Ghosh, R. A. Vilá, S. M. Eichfeld, J. D. Caldwell, X. Qin, Y. C. Lin, P. A. DeSario, G. Stone, S. Subramanian, D. F. Paul, R. M. Wallace, S. Datta, J. M. Redwing, J. A. Robinson, *Nat. Mater.* **2016**, 15, 1166.
- [216] N. Briggs, B. Bersch, Y. Wang, J. Jiang, R. J. Koch, N. Nayir, K. Wang, M. Kolmer, W. Ko, A. De La Fuente Duran, S. Subramanian, C. Dong, J. Shallenberger, M. Fu, Q. Zou, Y. W. Chuang, Z. Gai, A.-P. Li, A. Bostwick, C. Jozwiak, C. Z. Chang, E. Rotenberg, J. Zhu, A. C. T. van Duin, V. Crespi, J. A. Robinson, *Nat. Mater.* **2020**, 19, 637.
- [217] R. Cheng, Y. Wen, L. Yin, F. Wang, F. Wang, K. Liu, T. A. Shifa, J. Li, C. Jiang, Z. Wang, J. He, *Adv. Mater.* **2017**, 29, 1703122.
- [218] J. H. Yu, R. Chen, *InfoMat* **2020**, 2, 905.
- [219] J. Chu, Y. Zhang, Y. Wen, R. Qiao, C. Wu, P. He, L. Yin, R. Cheng, F. Wang, Z. Wang, J. Xiong, Y. Li, J. He, *Nano Lett.* **2019**, 19, 2154.
- [220] J. Xiao, M. Zhao, Y. Wang, X. Zhang, *Nanophotonics* **2017**, 6, 1309.
- [221] Y. L. Guo, B. Wang, X. W. Zhang, S. J. Yuan, L. Ma, J. L. Wang, *InfoMat* **2020**, 2, 639.
- [222] Z. Y. Lin, J. L. Wang, X. Y. Guo, J. W. Chen, C. Xu, M. Q. Liu, B. L. Liu, Y. Zhu, Y. Chai, *InfoMat* **2019**, 1, 242.
- [223] W. H. Wang, K. Y. Liu, J. Jiang, R. X. Du, L. T. Sun, W. Chen, J. P. Lu, Z. H. Ni, *InfoMat* **2020**, 2, 761.



**Junwei Chu** received his B.E. degree in electronic science and technology from University of Electronic Science and Technology of China (UESTC) in 2015. Now, he is a Ph.D. candidate in Prof. Jie Xiong's group at the School of Electronic Science and Engineering, UESTC. His scientific research concentrates on the growth of 2D magnetic materials and related spintronic dynamics.



**Xianfu Wang** received his Ph.D. degree in Physical Electronics from Huazhong University of Science and Technology in 2015. He is now a distinguished professor at University of Electronic Science and Technology of China. His current research interests focus on low-dimensional functional materials and fundamental principles in nanoelectronics and optoelectronics.



**Jie Xiong** received his Ph.D. degree in Materials Physics and Chemistry from UESTC under the supervision of Prof. Yanrong Li in 2007. He worked in Los Alamos National Laboratory, USA, as a postdoc from 2009 to 2011. Currently, he is working at School of Electronic Science and Engineering, UESTC. His research interests have focused on the growth of low-dimensional materials, the study of processing–structure–property–mechanism relationship of ferromagnetic, multiferroic materials, 2D materials, and nanostructured storage materials and devices.